FACULDADE DE ENGENHARIA DA UNIVERSIDADE DO PORTO

U.PORTO

FEUP FACULDADE DE ENGENHARIA
UNIVERSIDADE DO PORTO

Noninvasive Techniques for Vine Perception

Rodrigo Gomes Borges

WORKING VERSION

Mestrado Integrado em Engenharia Eletrotécnica e de Computadores

Supervisor: Prof. Manuel Cândido Duarte dos Santos (FEUP)

Co-Supervisor: Dr. Filipe Baptista Neves dos Santos (INESC TEC)

July 26, 2018

Resumo

Tecnologias de taxa de aplicação variável e pulverizadores agrícolas precisam ser inovados, otimizados e adaptados ao contexto da integração com robótica agrícola e agricultura de precisão. Um sistema de aplicação tradicional usa apenas informação fornecida por sistemas de dados agrícolas para pulverizar uma determinada quantidade de produto sobre as plantas. No entanto, estes sistemas não obtêm *feedback* em tempo real sobre a quantidade exata de produto aplicado e os requisitos reais de cada planta. Isto pode implicar perdas de produto e um baixo volume de aplicação do produto na planta (o que pode causar tratamento inadequado de doenças nas plantas). Novos sistemas, sensores e algoritmos devem ser estudados e desenvolvidos para avaliar a qualidade da pulverização e fornecer *feedback* em tempo real ao processo de pulverização.

O objetivo desta dissertação é validar uma técnica não invasiva para a perceção do conteúdo de água em vegetação e analisar várias opções para uma implementação viável do sistema. O conceito é que, nas frequências em torno de 20 GHz, a atenuação do sinal é afetada principalmente pelo conteúdo de água da planta que está a ser irradiada pelo sinal transmitido. A abordagem implementada consistiu em analisar a atenuação causada por folhas, plantas e elementos com água ao longo de uma transmissão entre um par de antenas de alto ganho.

Um conjunto de testes e experiências foi realizado para verificar e validar o conceito do método proposto, juntamente com uma análise dos dados recolhidos durante os testes. Os resultados destes revelaram uma clara influência da água na intensidade do sinal, validando a técnica proposta. Uma avaliação das capacidades de quantificação do sistema face à quantidade de água também foi realizada.

Uma comparação de diferentes abordagens possíveis para a implementação do sistema foi feita. Uma técnica de *beamforming* utilizando uma matriz de antenas foi simulada e desenvolvida. O foco foi dado ao desenvolvimento do lado do emissor do sistema, com a fabricação dos elementos simulados no decorrer desta dissertação.

Abstract

Variable Rate Technologies (VRT) and sprayers need to be innovated, optimized and adapted in the context of agricultural robotics and precision agriculture. A traditional VRT system only uses information provided by agro data cloud systems to determine the amount of product required to be sprayed. However, these systems do not get real-time feedback about the real amount of product applied and the real requirements of the plant. This may imply product losses and a low volume of product application on the plant that may cause inadequate plant disease treatment. New systems, sensors, and algorithms should be researched and developed to evaluate the spraying quality in real-time, and give real-time feedback to the spraying process.

The purpose of this dissertation is to validate a noninvasive technique for vegetation water content perception and analyze several options for a viable and cost-effective system implementation. The concept is that, at frequencies around 20 GHz, the attenuation of the signal is mostly affected by the water content of the plant being irradiated by the transmitted signal. The implemented approach consisted of analyzing the attenuation caused by leaves, plants, and elements containing water over a transmission between a pair of high gain antennas.

A set of experiments were conducted to verify the concept of the proposed method, along with an analysis of the collected data during the tests. The results of these tests revealed a clear influence of water on the intensity of the signal, validating the proposed technique. An assessment of the quantification abilities of the system was also made.

A comparison of the different potential approaches for the system implementation was made. A beamforming technique using a phased array of antennas was developed and simulated. The focus was given on the emitter side of the system, with the fabrication of the simulated elements during the course of this dissertation.

Key words: Agriculture; Antennas; Microwave; Normalized Difference Water Index; Pulverization; Robot; Water Sensing; Water Stress.

Acknowledgements

Gostaria de começar por agradecer aos meus supervisores, professor Cândido Duarte, pela dedicação, conhecimentos transmitidos e sobretudo por todo o apoio ao longo deste percurso, e doutor Filipe Santos, pela sua disponibilidade.

Não poderia deixar de agradecer à minha família, por todo o apoio incondicional.

Aos meus amigos, um agradecimento por todas as histórias partilhadas durante estes anos e por toda a ajuda, direta ou indireta, no desenvolvimento desta dissertação.

Rodrigo Gomes Borges

"We cannot solve our problems with the same thinking we used when we created them."

Albert Einstein

Contents

List of Figures

List of Tables

Abbreviations and Symbols

ADS	Advanced Design System
CSV	Comma Separated Value
DEEC	Departamento de Engenharia Electrotécnica e Computadores
EM	Electromagnetic
EVI	Enhanced Vegetation Index
FEUP	Faculdade de Engenharia da Universidade do Porto
HFSS	ANSYS HFFS: High Frequency Structure Simulator
INESC TEC	Instituto de Engenharia de Sistemas e Computadores - Tecnologia e Ciência
NDVI	Normalized Difference Vegetation Index
NDWI	Normalized Difference Water Index
RF	Radio Frequency
RoMoVi	Robot Modular e Cooperativo para Vinhas de encosta
VRT	Variable Rate Technologies
VNA	Vector Network Analyser
VWC	Vegetation Water Content
SAR	Synthetic-aperture Radar
SMA	SubMiniature version A

Chapter 1

Introduction

Agriculture is the set of activities concerned with the cultivation of land and breeding of livestock. Englobing a large number of activities, each specific culture has its own science to respond to its various and singular problems. In the context of this dissertation, the focus will be made in viticulture.

Viticulture is the science, production, and study of grapes and the cultivation of grapevines. This science deals with all the aspects related to vineyards and grape production.

A vineyard is a plantation of grape-bearing vines, grown mainly for winemaking, but also for table grapes, raisins or juice production. The cultivation and maintenance of these vineyards are costly and laborious processes, needing a vast amount of resources, whether human or physical resources such as water, fertilizers, and land. The dependence on water usually leads to vineyards located near rivers and water reservoirs, regularly cultivated in the margins of these water bodies in steep-slopes topography with difficult access, therefore increasing the cost of production of grapes.

To face the progressive growth of the wine market and wine consumption on a worldwide basis, it is relevant the creation of techniques capable of aiding the vinification industry in the analysis of the grape production. Viticulturists are asking for sensors and techniques that can analyse in real time the vineyard treatments in order to be able to perform precision spraying, reducing the water and phytochemicals losses.

1.1 Context

In this context, it is important to develop techniques capable of measuring the amount of water in the vineyards, resulting in a decrease of water waste and an evaluation method of the spraying process. Current techniques are based on radar analysis, such as synthetic aperture radars (SAR), primarily directed to extract information about soil moisture and to monitor vegetation phenology. This dissertation aims to develop a ground-based noninvasive system, enabling a more precise analysis of the water stress in vineyards canopies.

1.2 Motivation

Sensing of agriculture canopies has been traditionally addressed through satellite radars, e.g. SAR, used to retrieve information on vegetation and provide soil moisture monitoring. For the purpose of precision agriculture, methods relying on ground-based scattering sensing are preferred instead, achieving much higher resolution through local measurements. Active methods based on wireless transmitter-receiver systems are known to provide the best degree of accuracy and the largest amount of information when comparing to passive approaches. By placing a wireless transmitter and receiver antenna in both ends of the vegetation, the water content can be sensed.

Several studies indicate the frequency dependency of the water absorption ratio with high frequencies (i.e. $> 8\,\text{GHz}$) provide the best sensitivity on detecting the amount of water content present in the vegetation (e.g. around $20\,\text{GHz}$). Also because of shorter wavelengths, the radar cross-section of the vineyard vegetation is increased, easing its detection and delimitation by using a simple transmissive system. Therefore, such application enables not only the measurement of water level in the vegetation but also a possible radar-like system to detect and map the vegetation. Here we will study, design, and pre-validate a novel noninvasive system to perceive the water content in vineyards.

1.3 Definition of the problem

The use of automated irrigation systems and spraying techniques need some type of feedback to know its effectiveness on the field. A traditional variable rate technology (VRT) uses only information supplied by agro data cloud systems to apply a certain amount of product. However, these sprayers do not get real-time feedback about the real amount of product applied. Moreover, there is not a way to determine and analyse the requirements of the plant, and adequate the quantities that are necessary. This may lead to product losses or to a deficient application of the product over the required plants.

The available technologies for remote sensing of vegetation water content rely on SAR systems or scatterometers. A technology capable of sensing the water content in a plant, and therefore, the quantity of product applied over the said plant, can be extremely beneficial for future improvements in the spraying techniques and decrease the amount of wasted product.

1.4 Goals

The main goals of this dissertation is to perform a set of tests to validate the proposed concept, along with an initial analysis of the collected data, and to propose and develop a noninvasive system to perceive the water content in vineyards. The system proposal relies on the absorption of electromagnetic radiation through the vineyard canopy to derive a precise water content mapping. The system will be mounted on the AgRob V16 robot, that is being tested in RoMoVi P2020 Project [10], capable of operating on steep-slopes scenarios as it is common with vineyards.

As the robot moves along the vineyard, the absorption ratio of high frequencies in the range of 19.5 GHz to 20 GHz is measured and stored, enabling a thorough analysis of the water content in the vegetation.

1.5 Document organization

Since the work developed during this dissertation is based on a concept, its structure is slightly different from the normal. The first part consisted of validating the proposed concept and analysing the results of these tests, and the second part consisted of analyzing and proposing an implementation for a system to apply the technique that uses this concept.

After this introduction, a bibliographic review covering the topics of backscatter and its interaction with vegetation, SAR and radar systems — for different applications related with vegetation — and water remote sensing — using infrared spectrum — will be made in chapter 2.

In chapter 3, the tests performed to validate the concept will be explained along with the analysis of the test results.

Chapter 4 proposes a system design to implement the technique. The various stages of development of said design will be explained, as well as the presentation of real results compared to the various perfomed simulations.

Finally, chapter 5 presents the conclusion of the work developed, along with a balance of fulfillment of the objectives and sugestions for future work.

Chapter 2

Bibliographic Review

This chapter presents technologies and applications in remote sensing. A small introduction about backscatter will be given, as well as an overview of experiments and applications of this technique in agricultural environments. Techniques of remote water sensing will also be talked. The chapter is divided in 3 main parts.

Section 2.1 presents a brief explanation about backscatter, referring to the relationship with soil roughness and the interactions with vegetation.

Section 2.2 presents a overview about synthetic-aperture radar and its applications. A comparison between the different types of mountings for SAR systems and scatterometers will also be given. From subsection 2.2.1.1 to subsection 2.2.1.3, some applications of SAR related to agriculture and remote water sensing will be presented.

In section 2.3, a technique using the infrared spectrum to sense the water content of leafs will be discussed. In this section it will also be presented some vegetation indices based on the infrared spectrum.

2.1 Backscatter

In physics, backscatter or backscattering is the reflection of waves back to the same direction of the transmitted wave. It differs from reflection as the waves suffer diffuse reflection, as can be seen in figure 2.1. It has many applications such as in astronomy, photography, surface and landscape analysis, and meteorology.

The backscattering coefficient (sigma naught or σ_0) of a ground surface observed by a radar system is affected by two sets of parameters, as stated in [11]. The first set is related to the radar parameters as the angle of incidence, frequency, and polarisation of the transmitted signal. The second set is related to intrinsic parameters of the ground: 1) dielectric constant (ε') and 2) surface roughness. The dielectric constant of the ground is very dependable on its moisture content and the effects of the different types and textures of ground are negligible to the value of this constant, compared to the effects of water content, as stated in [12].

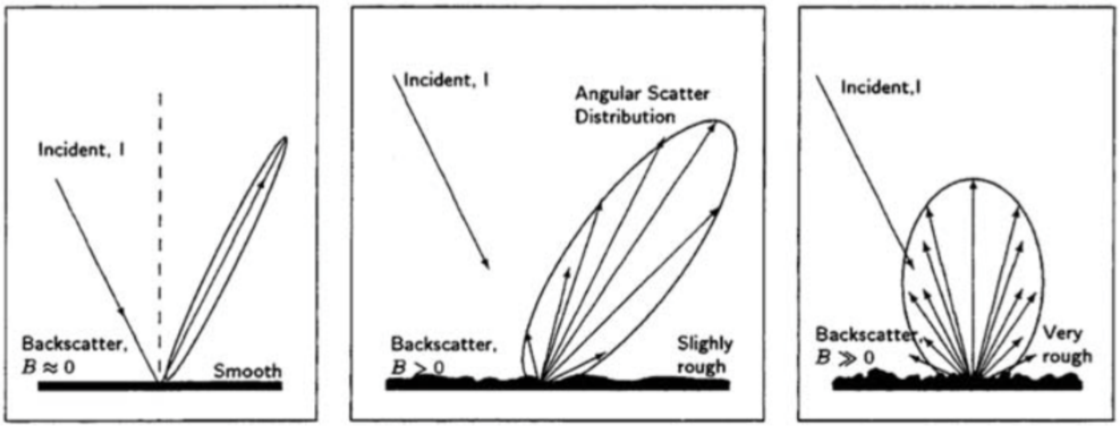

Figure 2.1: Effect of surface roughness on backsctatter [1].

2.1.1 Interaction with vegetation

Susan et al [13] states that higher frequencies contain more information on vegetation dynamics and that lower frequencies minimize the influence of vegetation on backscatter from the soil. This is due to the relationship between the wavelength of the incident wave and the object. An object reflects a particular wavelength if its dimensions are of the order of that wavelength. Therefore, the different components of a vegetation canopy interact differently with different wavelengths, as shown in figure 2.2.

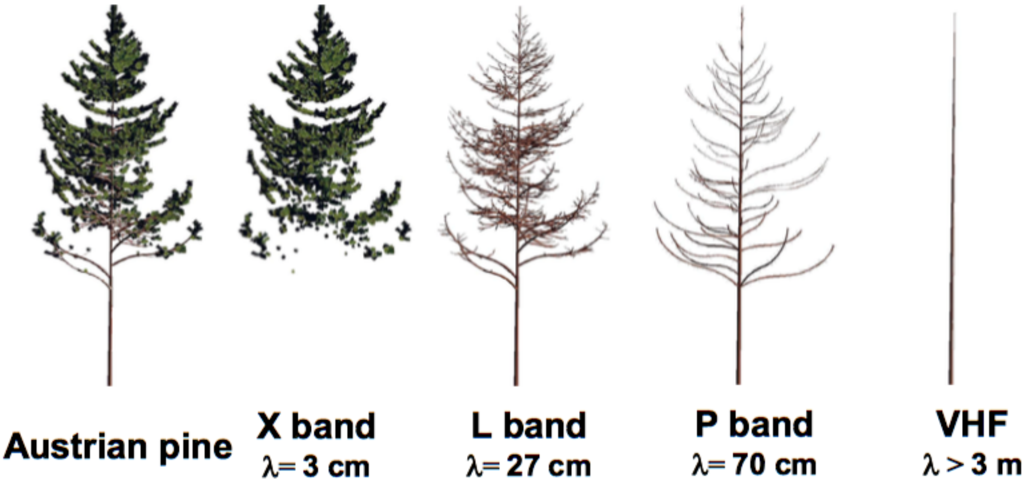

Figure 2.2: The relationship between the wavelength and the elements of a tree [2].

Higher frequency electromagnetic waves (C- and X- bands with a wavelength of 2.5 cm to 7.5 cm) are reflected mainly by leaves and small trunks. Lower frequencies (L-band and ultra high frequency (UHF) with a wavelength of 15 cm to 1 meter) are able to penetrate the vegetation canopy and are better suited to extract information about soil moisture. In figure 2.3, a representation of the interactions between the different wavelengths and the canopy can be seen, showing that the longer the microwave wavelength, the greater the penetration of the vegetation canopy.

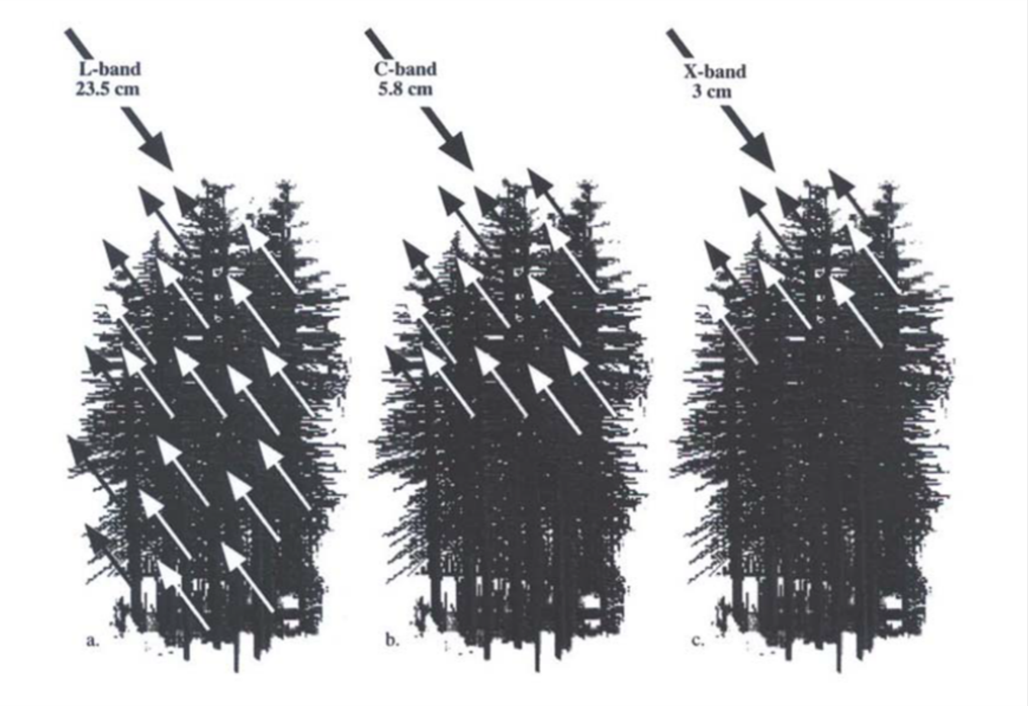

Figure 2.3: Penetration on vegetation canopy of different wavelengths [3].

2.2 Radar scatterometers and SAR

Scatterometry is a form of radar remote sensing that can measure multiple geophysical properties of Earth's surface based on the amplitude of microwave electromagnetic signals that are transmitted from and scattered back to an antenna. A radar system that measures the amplitude of the scattered signal is called a "scatterometer".

Synthetic aperture radar is a complex imaging system that transmits electromagnetic waves with a frequency between 300 Mhz to 300 Ghz (electromagnetic waves in this frequency range are called microwaves), and receives the reflections of the backscattered signals [14]. The transmitted wave interacts with multiple elements in the Earth surface, with each having a unique backscatter pattern. This pattern is a combination of the amplitude and phase of the backscattered signal and depends mainly on the physical characteristics (for example dimensions, shape and surface roughness) and the electrical characteristics, namely the dielectric constant, of the targeted element [4].

The purpose of SAR is to create an image of the area or object being analysed. This type of radar is normally installed in a moving platform, and uses the motion of the platform to scan the desired area of interest. Due to the continuous motion of the platform, the time of a transmission and the time of the reception of the respective echoed signal translates into different positions of the system. The combination of the received signals enables the creation of a virtual aperture, hence the name "synthetic aperture", that is much larger than the physical dimensions of the systems' antenna [4]. A representation of a SAR imaging system can be seen in figure 2.4.

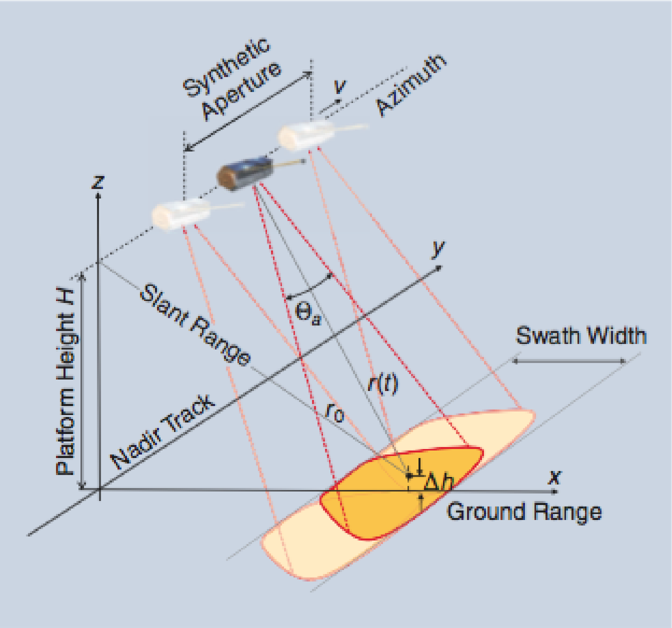

Figure 2.4: Representation of the SAR imaging geometry [4].

Since it has the ability to illuminate the area of interest with its own transmitting signal, its performance is independent of the available daylight and weather conditions. The image obtained by SAR differentiates the targets with high backscattering signals from low backscattering signals. High values of backscatter are represented as bright spots (usually associated to rough surfaces) and low values of backscatter are represented as darker spots [14].

The applications of SAR are really diverse, ranging from security and surveillance to geosciences as topography, oceanography, glaciology or geology. The advantages over an optical system are essentially due to the lack of dependability in daylight, allowing to operate effectively at day and night. Moreover, the system can work in hazy conditions, something impracticable to an optical system. Nevertheless, optical systems can produce true color images with higher resolution than SAR, which may be more suitable for some applications [14].

As complementary technology is expected that the fusion of SAR and optical systems results in high value monitoring data. Studies have suggested that the analysis of SAR signal response to vegetation can be improved by combining data from optical sensors [15]. The workflow of the combination between optical and SAR images can be seen in figure 2.5, along with ground data to enhance the results to a specific vegetated area.

SAR instruments are normally installed in aircrafts or in spaceborne systems as satellites and used in airborne experiments, whereas tower- and truck-based scatterometers (figure 2.6) are commonly used for ground campaigns. Operating a tower-based system is a lot less expensive than flying an airborne instrument, so the data gathering can be a lot denser in time than that from an airborne campaign. It is also much easier to modify the observation parameters such as incidence angle, allowing a greater diversity of data collection. However, being a ground-based system, it is difficult to move the system to analyse different areas, limiting the diversity of fields and

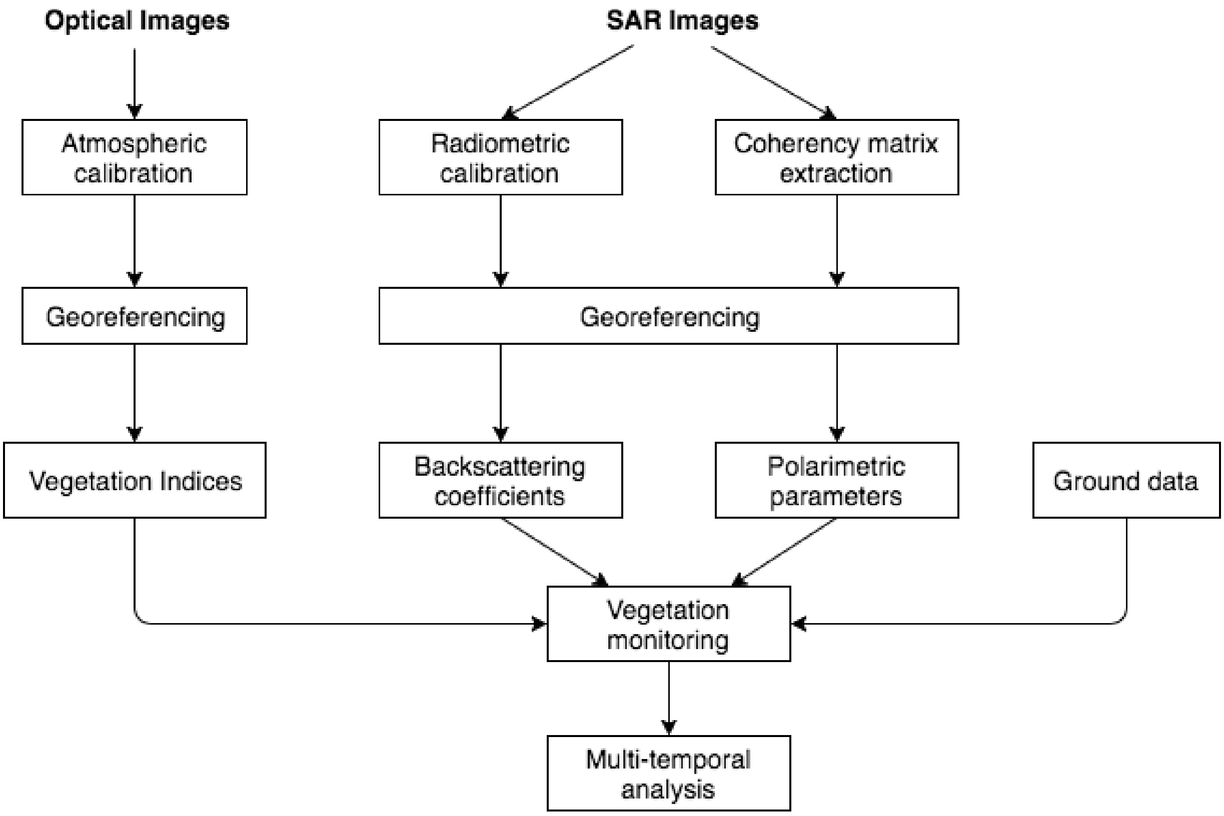

Figure 2.5: Workflow of the processing of SAR images, optical and ground data, adapted from [5].

conditions that can be examined in a single campaign [13].

2.2.1 SAR and radar applications

SAR images and radar scatterometer data have wide applications in remote sensing and mapping of the surfaces of the Earth. In the context of this dissertation, SAR and radar data can be used to analyse soil moisture, vegetation monitoring, as well as crop classification and crop growth monitoring. In the next sections, it will be presented some applications and the results obtained from experiments in that field.

2.2.1.1 Soil moisture monitoring

Remote sensing of soil moisture is of primary concern to water resource management of farming regions (as to assess water availability for plant growth) and to flood prevention and forecasting. It is also important for many hydrologic applications including mapping rainfall events and monitoring differential drying patterns [11, 16].

There is evidence that SAR systems can provide information about soil moisture since SAR backscatter has been shown to depend on natural surface parameters such as surface roughness and dielectric constant [16, 17]. Moran et al [16] add that the SAR backscatter is directly related

Figure 2.6: ComRAD microwave instrument system - an example of a truck-based scatterometer.

to the target dielectric constant (ε'), which is the dielectric capacity of the material being analysed compared to the dielectric capacity of vacuum. This dielectric constant is highly dependent on soil moisture [11]. The dependency is due to a large difference between dielectric constants between a dry soil and water. At low frequencies (below 10 GHz), water has a dielectric constant of $\varepsilon' \cong 80$ and dry soil has a value of ε' between 2 and 3 [12, 15, 17, 18]. Therefore, an increase in soil moisture content changes ε', which results in a strong sensitivity of the SAR signal to the soil moisture content. The SAR signal is also influenced by the topography of the landscape, vegetation density and to surface roughness [16].

In [16], it is shown that the results of monitoring the surface soil moisture (to 5 cm) using SAR signals are confounded by variations of the topography of the area being evaluated, the respective surface roughness and the vegetation density in that area. In this experiment, the soil moisture content of three sites (which with a different dominant type of vegetation) was measured using the European remote sensing (ERS-2) SAR sensor with a frequency of 5.35 GHz (C-band), VV polarisation and an incidence angle of 23^{o}. To only evaluate the soil moisture content, the experiment was applied in flat sites, reducing the influence of the topography, and to reduce the effects of vegetation, its volume was measured on a monthly basis to quantify its influence in SAR backscatter. To better estimate the surface soil moisture content, optical images from the Landsat thematic mapper (TM) sensor where used. The initial results "showed that measurements of C-band SAR backscatter (σ^0 , dB) were poorly correlated ($r^2 = 0.27$) with surface soil moisture content". This poor correlation was due to differences in the surface roughness of the three sites that were analysed, and after correcting the data for differences in the surface roughness using images and the SAR backscatter data from the dry season, the correlation increased to $r^2 = 0.93$. Despite a good correlation between the SAR backscatter and soil moisture content, the overall sensitivity of the SAR signal to soil moisture changes was poor, since a change of 25% in soil moisture content only resulted in a 3 dB change of the signal backscatter.

Ulaby [11] studied the effects of soil moisture on radar backscatter by measuring the spectral response from two bare-soil fields with very different surface textures, using the University of Kansas 4-8 GHz microwave active and passive spectrometer (MAPS) system. The measurements were made over the period of a month, at 2-3 day intervals. Each collection of data consisted of measuring the radar response at 10 frequency points in the range of 4-8 GHz, at incident angles of 0^o to 70^o in 10^o increments for all polarisations.

The results showed that for soils with a smooth surface and low moisture content (4.3%), the change in incident angle does not cause significant changes in the backscatter signal. However, for a soil moisture state of 30.2%, the increase in incident angle produced an exponential decrease in the backscatter signal. The increase in moisture content not only influences the dielectric properties of the soil, but it also causes the surface texture to appear smoother to the incident wave. As represented in section 2.1, figure 2.1, this leads to a low value of backscatter signal. As for soil moisture in a smooth surface, the results showed that an increase of the signal frequency allowed a better sensitivity of radar backscatter as the percentage of soil moisture increased. Again, this result is caused by the effect of soil moisture which caused the surface to appear "smooth" in terms of the signal frequency. The smoothing effect caused the backscatter return to decrease at lower frequencies ($\sim$4 GHz), but as the frequency was increased to $\sim$8 GHz, the surface roughness increased enough to make the surface look "rough" again.

2.2.1.2 Vegetation crop monitoring and classification

Agricultural targets are very dynamic throughout the growing season, and thus remote sensing is an attractive approach to mapping and monitoring applications. Remotely sensed data including images from SAR and scatterometer systems can be used to derive useful crop information.

In [19], a ground-based multifrequency polarimetric scatterometer was used to evaluate the radar vegetation index (RVI) as a tool to estimate vegetation water content (VWC). The RVI is given by

$$RVI = \frac{8\sigma_{HV}}{\sigma_{HH} + \sigma_{VV} + 2\sigma_{HV}} \tag{1}$$

where σ_{HV} is the cross-polarization backscattering cross section and σ_{HH} and σ_{VV} are the copolarization backscattering cross sections.

The system provides data at the L-, C- and X- bands. The experiment was made over a rice field and in a soybean field. For the two analysed fields, the results showed that there was an increase in the backscattering coefficient of the L-band over the course of the growing season and a decrease after harvesting. This trend is correlated with both the RVI and VWC for both cultures. When comparing the RVI of L- and C-band, it was observed that L-band RVI had a higher correlation with VWC in both cultures. From this, it is possible to conclude that the L-band presented the best attributes for the retrieval of rice and soybean growth parameters when compared to the C- and X-bands.

Moran et al [15] studied the potential for the combined use of SAR and optical data for crop management. The images were acquired in the visible, near-infrared and thermal spectrum. The SAR images were acquired with two different radar configurations:

- Ku-band at 14.85 GHz, VV polarization, and a 55^{o} incidence angle;
- C-band at 5.3 GHz, VV polarization, and a 23^{o} incidence angle.

The results showed that the signals at Ku-band are sensitive to soil roughness and insensitive to soil moisture when vegetation is present. With a uniform soil roughness, the results showed a correlation between NDVI and the Ku-band, which indicates that the Ku-band is sensitive to the vegetation cover. As for the C-band, the results showed that the C-band was the most suitable for soil moisture retrieval, but that the value was attenuated with the increase of vegetation cover.

2.2.1.3 Applications in vineyards

The SAR observation can also be applied to vineyards. These cites have different specifications than normal culture cites, since, for example, the vineyards can be installed in hilly terrains, with a fixed space between each row of vines and with a support system made of a variety of materials including wood or steel, which impacts the measurements of the SAR backscatter.

Although SAR backscattering is being used successfully in the monitoring of some culture growth as stated in section 2.2.1.2, in vineyards, the difference in growth of the grapes are the only noticeable aspect that changes the backscatter signal. Therefore, it is required to reduce the effects of all the external elements such as the plant phenology and the cultivation practices.

In [20], it is studied the impact of grape development and growth in the backscatter of SAR signals from an airborne SAR system. To only account for the grape biomass, SAR images of uncultivated soils close to the vineyards were used to decrease the effect of the soil in the experiments. Two time series of SAR images were acquired during the annual growth cycle of grapevines in 1999 and 2001. The integration of the SAR images into the Geographical Information System (GIS) of the "Bacchus" project [21] allowed the retrieval of relevant data about the vineyards. The results revealed an increase of backscattering caused by the cultivation techniques used during the winter period, which causes an increase in the surface roughness. A steady increase during the development and ripening period of the grapes and a drop after the harvesting of the fruit suggests that SAR might be used to monitor wine production. Therefore, these results denote the sensitivity of SAR to the cultivation techniques and to the growth of the grapes.

An experiment was made to extract SAR images from a wine-producing landscape [22]. The experiment took place in October 2005, and the SAR images were collected using a SAR system onboard of an aircraft. The system flew over the landscape on the 5^{th} October, when the grapes were still present, and on the 25^{th} October, after the vintage. The first assessment of the SAR potential in monitoring grape growth by examining the acquired images was difficult due to the different weather conditions affecting the two flights.

In [6], the images obtained in [22] were processed and analysed by two methods. The first method consisted of the use of HH, VV, and HV polarisations and a bare soil reference. However, the results were noisy and limited the analysis, preventing any conclusion. The second method was based on the polarimetric features of the SAR images and the study of the sensitivity of the co- and cross-polarisations. A decrease of the co- and cross-polarized backscatter was observed between the two dates, which indicates sensitivity to grape growth. Figure 2.7 represents the difference between the backscatter on the HV and the HH polarisation (in dB) between the two flight days. The decrease of the red and yellow areas from the first image to the second is noticeable.

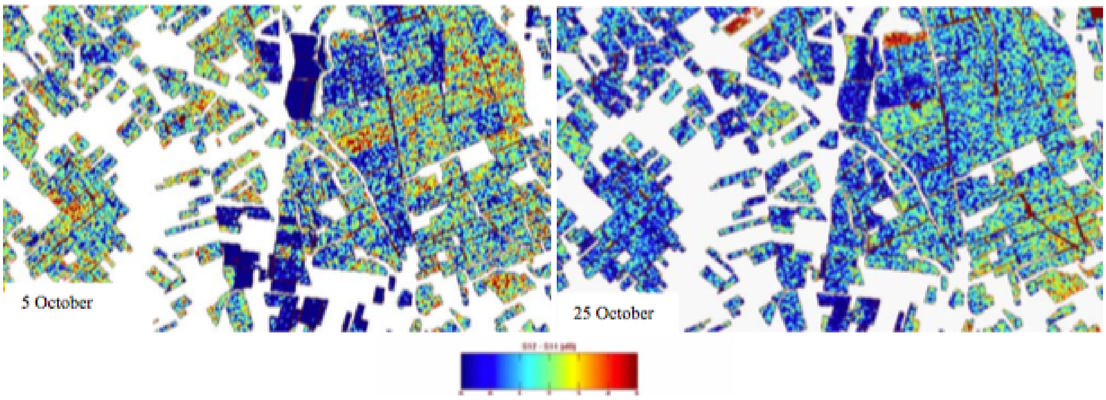

Figure 2.7: Backscatter difference between the fist flight (5^{th} October) and the second flight (25^{th} October) [6].

After analysing the results, it was concluded that backscattering is greatly influenced by vineyard cultivation practices such as ploughing and harrowing. A steady increase of the backscatter coefficient over the growing season of the grapes, and a decrease after the grape harvesting denotes that SAR imaging can be sensitive to the grapes development.

2.3 Water remote sensing using infrared spectrum

Another method of remote sensing is the analysis of the reflectance by vegetation canopies in the near-infrared region. This reflectance is largely affected by the biological properties of the plant, and in the regions of 0.7 to 1.4 μm (near-infrared wavelengths) and 1.3 to 2.5 μm (middle-infrared wavelengths) of the electromagnetic spectrum, the reflectance is affected by the quantity of water in the leafs [23].

In [24], an analysis of the spectral reflectance of leafs with different levels of water content was made based on simulations with leafs with a known water content. The reflectance of wavelengths in the regions of 0.4 to 2.5 μm is affected by the intensity of the incident wave. Therefore, the impact of atmospheric absorption must be taken into account, since it greatly affects the incident and reflectance of the leaf back to the sensor being used.

The results showed that the leaf spectral reflectance variations were different for the different wavelengths regions used during the simulations, and were affected by the water content in the leafs. The increase in water content led to a decrease in the reflectance of the leafs, being more noticeable in the 1.42 to 188 μm region, the 1.90 to 2.05 μm region and the 2.10 to 2.35 μm region.

Taking into consideration the atmospheric transmission characteristics, the results showed that the 1.55 to 1.75 μm region was the most-suited band in the infrared spectrum region to monitor the water content from space platforms.

2.3.1 Vegetation indices

Vegetation indices (VIs) are used to quantitatively and quantitatively evaluate and analyse the vegetation cover using spectral measurements [25]. These indices use two or more bands related to the spectral characteristics of the vegetation [26]. The spectral response of vegetated regions presents a complex mixture of vegetation, soil characteristics such as moisture and brightness, and are also influenced by atmospheric variations. The use of indices allows the qualification of this complex phenomenon without the need to separate the value into each particular characteristic since this separation is generally hard [25].

VIs have been widely used for remote sensing of vegetation, and its usefulness relies on having better sensitivity than individual spectral bands [25] and can be used for crop classification or monitoring, vegetative cover density and for remote sensing of vegetation water content. From 2.3.1.1 to 2.3.1.3 some vegetation indices will be presented.

2.3.1.1 Normalized Difference Vegetation Index

Normalized Difference Vegetation Index (NDVI) is a measurement of the density of green vegetation over the Earth's surface [7]. This index uses the reflectance of electromagnetic waves near the 0.66 μm and the 0.86 μm wavelength regions [27] to derive the density of green vegetation covering a specific area. Its value is calculated by

$$NDVI = \frac{\rho_{NIR} - \rho_{RED}}{\rho_{NIR} + \rho_{RED}} \tag{2}$$

where ρ_{RED} and ρ_{NIR} refers to the reflectance over the 0.66 μm and 0.86 μm wavelength, respectively. Values of NDVI between 0 and 0.1 correspond to arid areas with close to none green vegetation; values between 0.2 and 0.3 correspond to grass fields and shrubs and values greater than 0.6 correspond to large green vegetation areas as rainforests [7], as shown in figure 2.8.

2.3.1.2 Enhanced Vegetation Index

The lack of feedback in NDVI renders it susceptible to errors caused by variable atmospheric and canopy background conditions. For a constant vegetation canopy, a dark or wet background soil results in a higher NDVI value. The effects of atmospheric conditions also alter the value

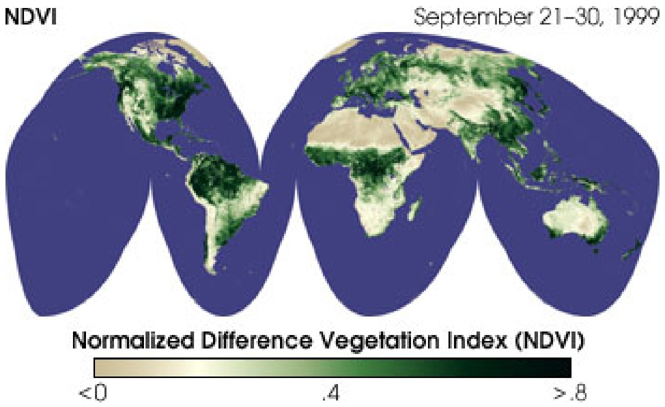

Figure 2.8: Normalized Difference Vegetation Index between September 21-30, 1999 [7].

of NDVI: high atmospheric aerosol contents (minute particles suspended in the atmosphere that interact with radiation) produce lower NDVI signals, whereas lower atmospheric aerosol contents produce higher NDVI signals [28]. Due to these potential errors, the Enhanced Vegetation Index (EVI) was proposed as a modified NDVI with the capability of adjusting to the canopy background and being more robust to the atmospheric conditions [8].

EVI is calculated by the following equation

$$EVI = G \times \frac{\rho_{nir} - \rho_{red}}{\rho_{nir} + (C_1 \times \rho_{red} - C_2 \times \rho_{blue}) + L} \tag{3}$$

where ρ_{nir} corresponds to the reflectance at the near-infrared wavelengths (0.7 to 1.1 μm), ρ_{red} corresponds to the reflectance at red wavelengths (0.6 to 0.7 μm) and finally ρ_{blue} corresponds to the reflectance at blue wavelengths (0.45 to 0.52 μm). The C_1 and C_2 coefficients are used to correct aerosol scattering in the red band by the use of the blue band, G is a gain factor and L is the canopy background adjustment factor. Generally, the coefficients used in equation 3 are, $L = 1$, $G = 2.5$, $C_1 = 6$ and $C_2 = 7.5$ [8].

Although the performance of EVI is better in numerous applications compared to NDVI, it is also more sensitive to the topography of the area being analysed. This greater sensitivity was concluded to be caused by the canopy background adjustment factor "L".

In figure 2.9 the effect of the topography in NDVI and EVI can be observed.

2.3.1.3 Normalized Difference Water Index

Gao in [27] proposes a different index, the Normalized Difference Water Index (NDWI), for remote sensing of vegetation water content. Similar to NDVI, NDWI uses the reflectance of two electromagnetic channels, this time one channel near the 0.86 μm and the second channel near the 1.24 μm wavelength regions. This new index is calculated by a similar equation to 2, as shown by

$$NDWI = \frac{\rho(0.86\ \mu m) - \rho(1.24\ \mu m)}{\rho(0.86\ \mu m) + \rho(1.24\ \mu m)} \tag{4}$$

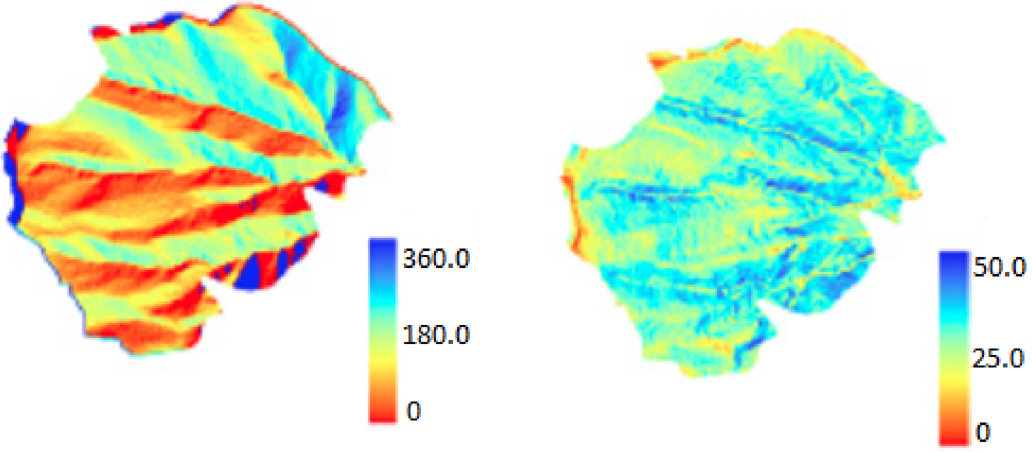

(a) Aspect (b) Slope

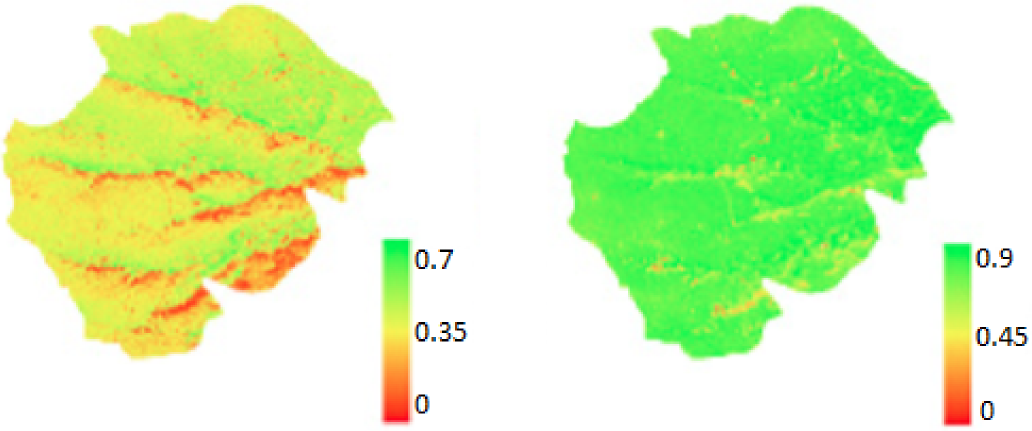

(c) EVI (d) NDVI

Figure 2.9: Effect of topography in EVI and NDVI, adapted from [8].

where each ρ represents the reflectance in the specific wavelength. These two wavelengths were chosen since they both have similar vegetation scattering properties but different sensitivities to liquid water changes. Since the 1.24 μm channel is sensitive to liquid water variations, it is expected that NDWI is also sensitive to these same variations.

The effects of soil background and atmospheric water vapour were taken into account in the development of this index. Gao in [27] states that the soil reflectance increases with increasing wavelengths in the region 0.8 to 1.3 μm. Therefore, reflectance at 1.24 μm are greater than at 0.86 μm, meaning that, based on equation 4, the value of NDWI is expected to be negative for bare soils. After examining the effects of soil on NDWI, it was concluded that NDWI increases with the increase of the covered area being analysed. As for atmospheric water vapour, [27] states that the channels being used are not affected, and therefore, the effects on NDWI are minimal.

Some tests were performed to demonstrate the usefulness of this index for remote water sensing. The tests were performed under controlled conditions and consisted of the stacking of leafs to simulate an increase in water content. It was verified that NDWI increased with the number of layers which indicates that it is sensitive to the vegetation water content.

Chapter 3

Proposed approach and concept validation

In this chapter, an overview of the tests carried out for the purpose of validating the concept will be given.

The first phase of this dissertation was to validate the concept. The concept is that, at frequencies around 20 GHz, the attenuation of the signal is mostly affected by the water content of the plant being irradiated by the beam. The proposed approach is based on this concept, consisting of an emitter and a receiver with the element being analysed in between, as demonstrated in figure 3.1.

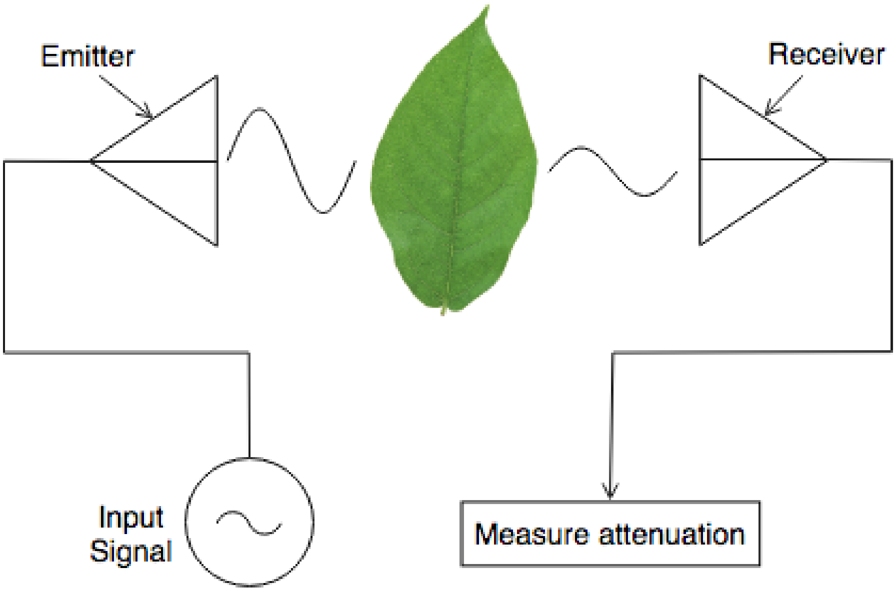

Figure 3.1: Overview of the proposed approach.

This range of frequencies around 20 GHz was chosen due to the effects of water in the intensity of the signals. As shown in figure 3.2, there is a peak of attenuation around 20 GHz for the line of the air containing water vapor, highlighted by the vertical red line.

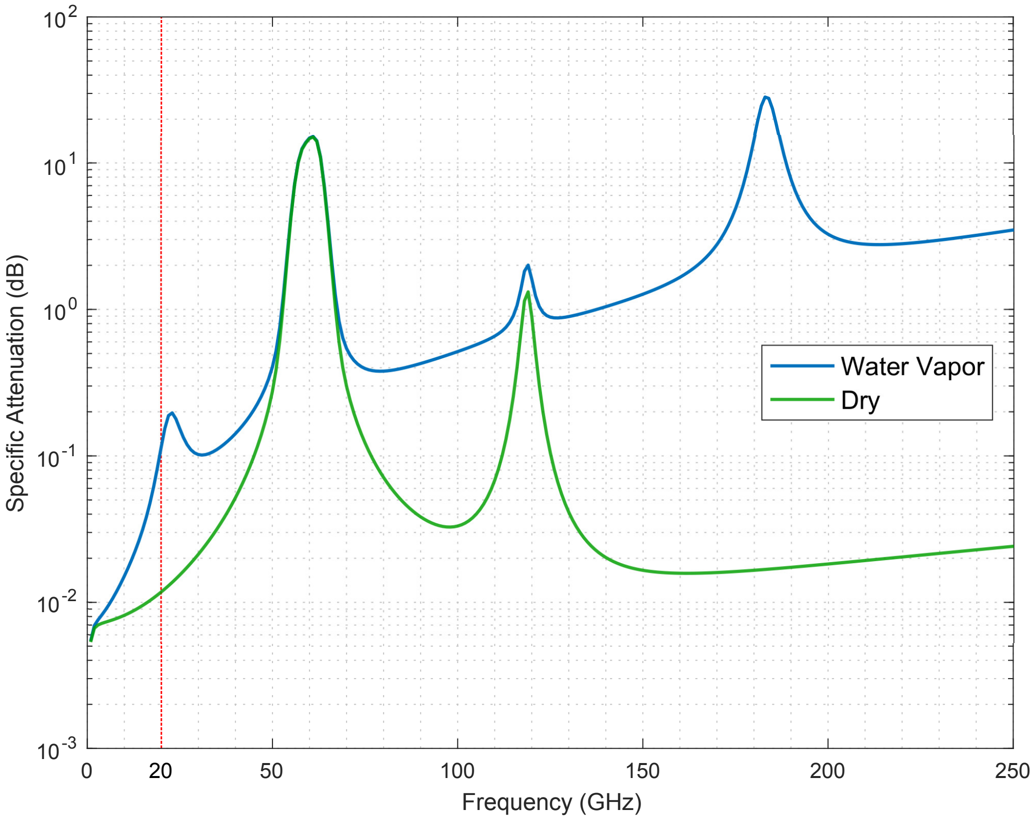

Figure 3.2: Atmospheric absorption for dry air and air containing water vapor [9].

The test equipment was also taken into account, since the maximum value of frequency for the test equipment in use was 40 GHz. However, at higher frequencies, the power loss is even greater than at 20 GHz, decreasing the distance between antennas and therefore, the distance to place objects and plants in between the antennas. This loss in power is due to the free space path loss (L_{fs}) calculated by

$$L_{fs} = 20\log_{10}\left(\frac{4\pi f D}{c}\right)\ \text{(dB)} \tag{3.1}$$

where f is the frequency, c is the speed of light in the vacuum and D is the distance between the emitter and the receiver. As observed in equation 3.1, the higher the value of the frequency, the higher the value of the free space path loss, and a consequent decrease in the maximum practical distance between the antennas.

3.1 Test equipment and set-up

To perform the tests for concept validation, some elements and instruments were used. The test equipment was composed of two high gain antennas mounted on a claw. This claw was placed on the end of a robotic arm, which allowed for the scanning of the object being measured. The pair of high gain antennas was connected to a vector network analyzer (VNA) by coaxial cables to measure the S-parameters of the transmitted signal, more precisely, the S_{12} parameter. The model of the VNA was the E8363B PNA Series Network Analyzer (10 MHz to 40 GHz) from Agilent Technologies and the model of the coaxial cables were the KMM24 from Thorlabs and the KBL-2FT-PHS+ from Minicircuits, both prepared for the high frequencies in use during the tests.

A Matlab script was developed to perform the tests, collect the data of each test and control the position of the robotic arm. The computer executing the script was connected to the VNA through a GPIB connection. The position control of the robotic arm was achieved by sending instructions through UDP between the computer and the robotic arm controller. The robotic arm controller had a UDP server running, and the Matlab script functioned as a UDP client. An overview of the test configuration is shown in figure 3.3.

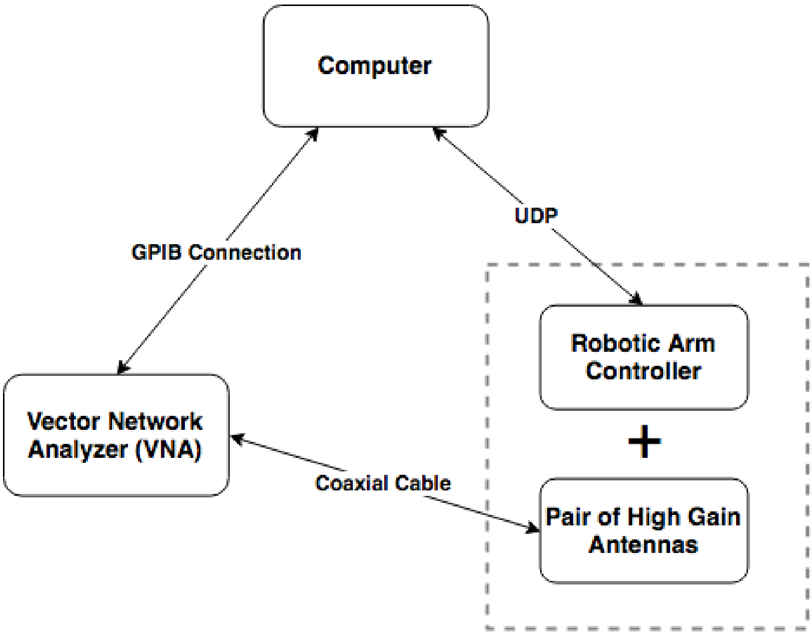

Figure 3.3: Overview of the test configuration.

The S-parameters describe the input-output relationship between ports or terminals in an electrical system. The S_{12} parameter represents the power transferred between two ports, in this case, the pair of antennas. The S_{11} parameter represents how much power is reflected from the antenna and it is known as the reflection coefficient. These parameters were measured using the VNA to characterize the frequency range of the antennas using the S_{11} parameter, and the signals attenuation over a transmission using the S_{12} parameter. Figure 3.4 shows the S_{11} parameter of the antennas used during the tests, where a value below -10 dB represents the region where the antennas radiate most of the input power. For these antennas, this range was between 19.5 GHz and 20.6 GHz. The frequency range measured for the S_{12} parameter, for all the tests analysing the different elements between the antennas, was from 19.5 GHz to 20 GHz.

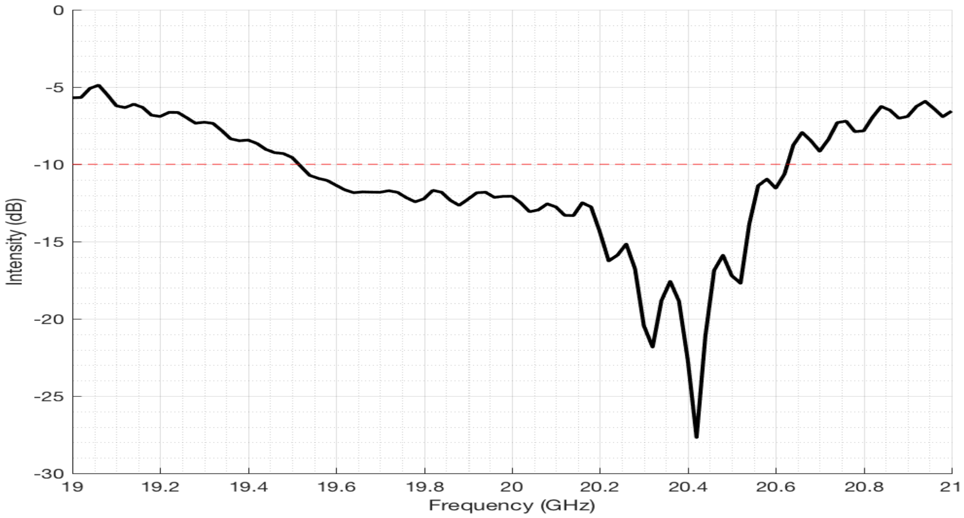

Figure 3.4: S_{11} parameter of the antennas used during the tests.

Figure 3.5 shows a photography of one of the antennas in use during the tests.

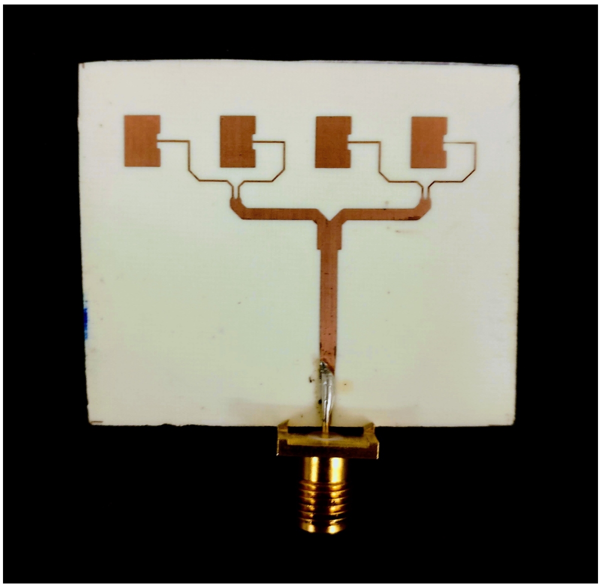

Figure 3.5: Photography of one of the antennas used during the tests.

3.2 Test methodology

For each test, a test element was placed between the antenna pair to be scanned. The area of this scanning process was defined in the Matlab script with the desired step size (the maximum value of this step size was 3 mm, dictated by the maximum precision of the robotic arm). The maximum size of the scanning area was a 20 cm by 20 cm square, due to physical limitations of the robotic arm. The test sequence consisted of acquiring the S_{12} parameter measured by the VNA on the initial point, send a request to move the robotic arm to the next position, acquire the S_{12} parameter of that position and so on until all the positions defined by the pre-determined area for the scanning process were achieved. The flow diagram describing the test sequence is shown in figure 3.6. With this sequence, a matrix was obtained where each point has the value of the signal intensity of the respective position of the scan. For all scans, the starting point was the lower left corner, with the scan being done by lines always from left to right. Figure 3.7 displays the recording of the multiple test positions of a test scan, where the lower left point represents the first position saved and the top right point represents the last position. The points do not form a perfect square and have a deviation to the right due to rounding errors of the position by the robotic platform. For each position, the VNA acquired a defined number of points of the intensity of the S_{12} parameter from 19.5 GHz to 20 GHz, saving the frequency value of each point, the value of the intensity of the S_{12} parameter and the phase of the signal at that frequency in a comma-separated values (CSV) file.

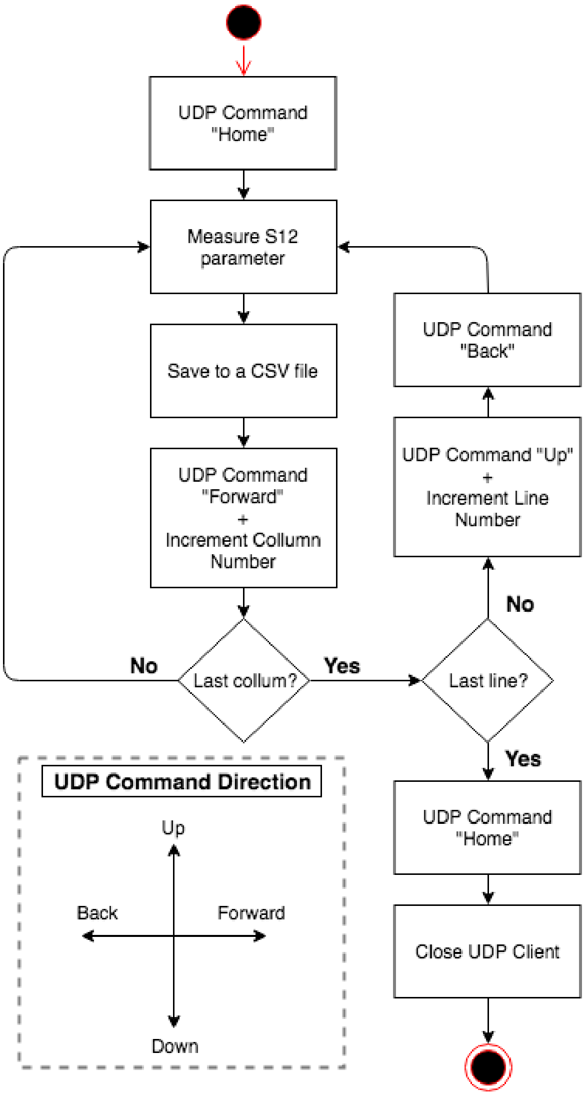

Figure 3.6: Diagram of the test scanning sequence.

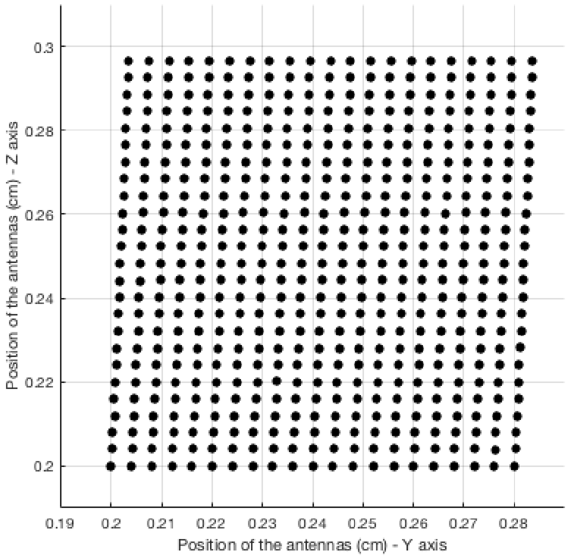

Figure 3.7: Plot of the recorded positions of a test.

The tests consisted of analysing different objects, plants, and leaves. The size of the objects and plants was limited by the distance between the pair of antennas. This distance was dictated by the size of the two claws used. With the first claw, the distance between antennas was 20 cm, whereas, with the second claw, this distance was 9 cm. Initially, the tests were performed using the first claw, although the distance between the antennas meant that sometimes the VNA measured really low values, in the range of -70 dB to -80 dB for the S_{12} parameter. This value was at the end of the VNA measuring range, and for that reason, the second claw was created to improve the tests performance and to increase the range of intensity values acquired by the VNA.

The first set of tests consisted of analysing containers such as plastic bags and plastic water bottles. These containers were chosen because plastic did not interfere with the signal being irradiated between the pair of antennas, therefore, ensuring that only the existence of water inside the container was what created changes in the intensity of the signal.

The following set of tests were performed using a cactus-like plant and some leaves. The leaves were tested with varied conditions such as a green leaf with water sprinkled over it to simulate a watering process and a leaf with a green and a brown dry part. For a better perception of the impact of the water content inside the leaf in the signals intensity, a sequence of tests was performed on a green leaf. Before each scan, the leafs mass was measured using a high precision scale. Between each scanning procedure, the leaf was left to dry naturally, and the perceived decrease of the leafs mass was mainly due to the evaporation of the water inside it.

The last set of tests consisted of analysing the systems precision and quantification abilities for different water levels. For these tests, the smallest claw was used with the pair of antennas facing each other in the vertical direction, with a petri dish sitting right above the bottom antenna. This test setup allowed for the extraction of data related to the sensitivity of the system to different water thicknesses, and consequently, different amounts of water. For each different water quantity inside the petri dish, the VNA would record the intensity of the S_{12} parameter of the signal. At the start of each test, a measurement of the container without water was made to serve as a reference value. The test sequence for this specific set of tests is shown in figure 3.8.

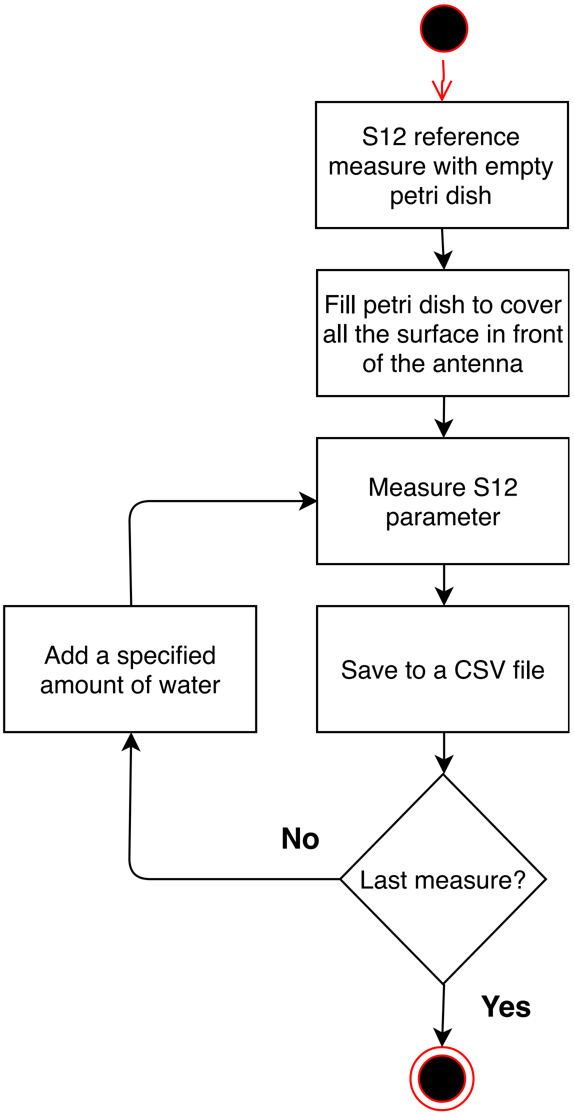

Figure 3.8: Diagram of the test scanning sequence for the last set of tests.

3.3 Analysis of collected data and tests results

The analysis of the collected data was performed using scripts developed in Matlab. The output files generated by the VNA measurements during the tests were saved as a CSV file, with the number of points and the frequency range being recorded defined by the script controlling the VNA. In these CSV files, the VNA saved three different values: the frequency of the point being measured (in GHz), the intensity (dB) of the signal at that frequency and its phase (in radians).

The function of these scripts was to import the data recorded on the individual CSV files to Matlab, extract the values of the intensity of each file, and create a matrix with the values for each position of the scanning area. Since all the intensity values are negative numbers, the next operation was to get the absolute values of the obtained matrix. Following this step, these values were normalized to the range of 0 to 1 using the maximum and minimum values of the matrix with the absolute values. The output of this script is a grayscale image of the object, plant or leaf, where the brightest part of the image represents the area with the greatest attenuation and, therefore, a greater water quantity, whereas, the darkest areas of the image represents a lower signal attenuation corresponding to areas with less water content. The basic sequence of actions of the developed scripts are shown in figure 3.9.

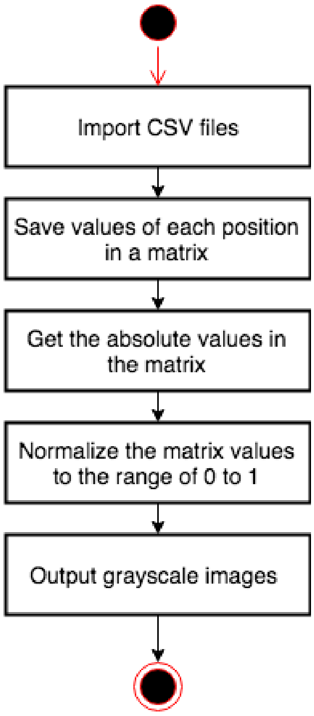

Figure 3.9: Diagram of the sequence for the analysis of the collected data.

Sometimes the visual differences between the different output images are not noticeable, and therefore, the analysis and comparison of the values of the different matrices is needed to denote slight variations and patterns otherwise invisible in the images.

For the tests of the systems precision and quantification abilities for different water levels, the results of the analysis of the collected data are graphical representations of the attenuation for the different water levels.

3.3.1 Plastic bag and water bottle

A test using a plastic bag was performed and the results of the tests are shown in figure 3.10. This bag was chosen because the material it was made of did not interfere with the signals intensity.

The bag was filled with water and suspended from a wooden structure. The scanning area was an 8 cm by 14 cm rectangle with a step size of 4 mm, corresponding to a total of 700 collected points. The scanning area was chosen in a way to include all the area of the plastic bag filled with water. This way, the expected test result is an image with black areas on the sides and on the top part of the image, with a brighter area corresponding to the area filled with water in the center. By analysing figures 3.10c and 3.10d one can clearly see the correlation between the real image and the resulting image, where the areas inside the red line represent the areas with water. The area right above the red line in figure 3.10d is not completely black, having pixels with a light shade of the grey color in the top of the image, which was caused by some droplets that where stuck to the inside walls of the plastic bag.

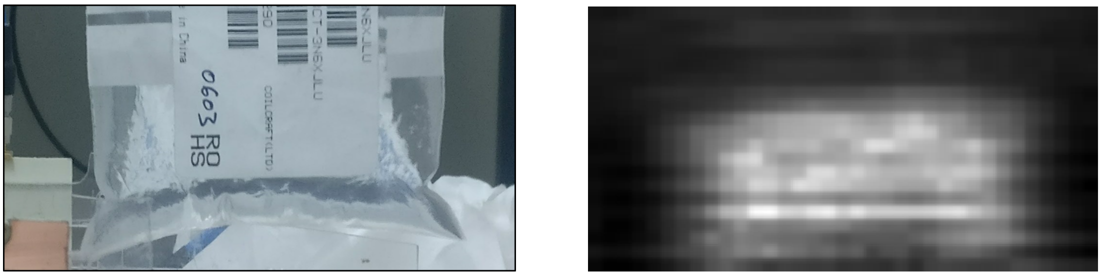

(a) Real image of the plastic bag.

(b) Resulting image of the test.

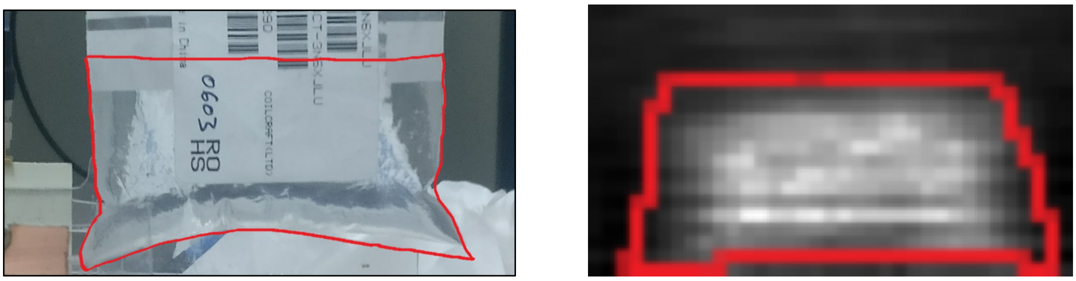

(c) Real image of the plastic bag with a red line denoting the area filled with water.

(d) Resulting image with a red line denoting the area with greater attenuation.

Figure 3.10: Images of the plastic bag and of the test results. The red lines used in (c) and (d) represent the area of the plastic bag filled with water.

The same test was performed using a water bottle. The scanning area was a 17 cm by 9 cm rectangle with a step size of 5 mm, corresponding to a total of 612 collected points. Figure 3.11 shows both the real image of the bottle and the result of the test. As in the previous test, the results show a clear indication of the effects of water on the signal's intensity, as shown by the bright area in the lower part of the resulting image, corresponding to the area filled with water. The top part of the resulting image shows a light grey area rather than a black area due to the influence of water droplets attached to the inner surface of the bottle. It is also noticeable a gradient from the side to the middle of the image, starting in a light grey and changing to a bright white. This is caused by the shape of the bottle, since the signal has to go through a larger amount of water in the middle than when the signal is going through the sides of the bottle.

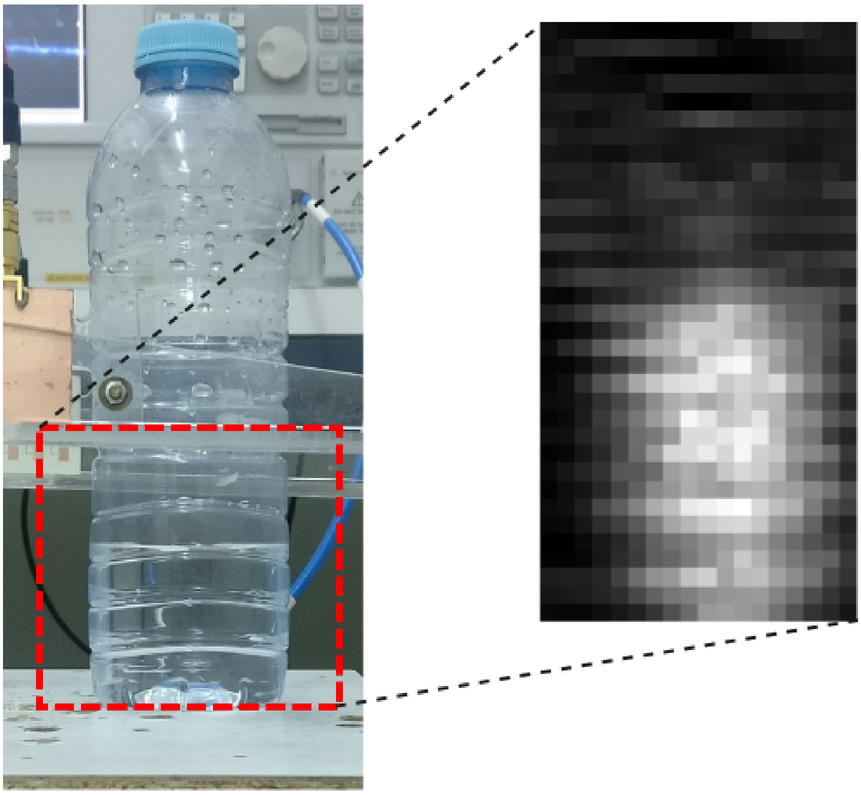

Figure 3.11: Comparison between the real image of the water bottle and the resulting image after the analysis of the collected data. The red square represents the estimated area scanned during the test.

3.3.2 Plants and leaves

The different tests performed with plants and leaves will be presented in the following subsections.

The leaves used during the tests were suspended from a wooden structure so that the only object in the middle of the claw with the pair of antennas was the leaves. The same type of leaf was used throughout the tests to decrease the number of variables. As for the plant, its size was small enough to be fitted between the antennas and to allow for the scanning procedure.

3.3.2.1 Cactus-like plant

A test using the largest claw and a cactus-like plant was made. This plant was chosen due to its high water content, causing a greater attenuation on the intensity of the signal. The analysis of the collected data for this test confirms that the signal is strongly attenuated when the signal is passing through the plant. This is perceptible by analysing the images obtained from the collected data, where the brightest parts of the images correspond to areas where a leaf of the plant is directly in the middle of the antenna pair, and the darkest areas correspond to the void spaces between each leaf, as observed in figure 3.12.

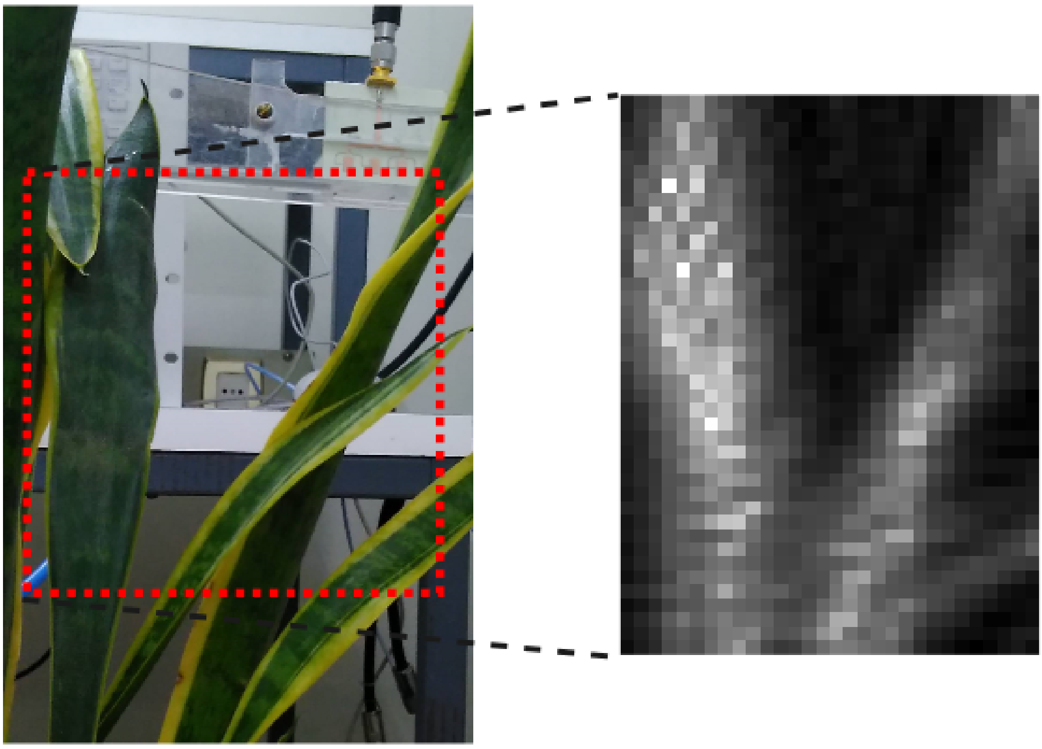

Figure 3.12: Comparison between the real image of the cactus-like plant and the resulting image after the analysis of the collected data. The red square represents the estimated area scanned during the test.

The scanning area of this test was a rectangle of 20 cm by 15 cm with a step size of 5 mm, corresponding to 1200 different points. The resulting images of the analysis of the collected data can be viewed in figure 3.13. In this figure, it is shown the results for three different frequencies (19.5 GHz, 19.75 GHz and 20 GHz) as well as the average of the magnitude in the range of 19.5 to 20 GHz. The analysis of the resulting images reveals better results using the average of the frequency range.

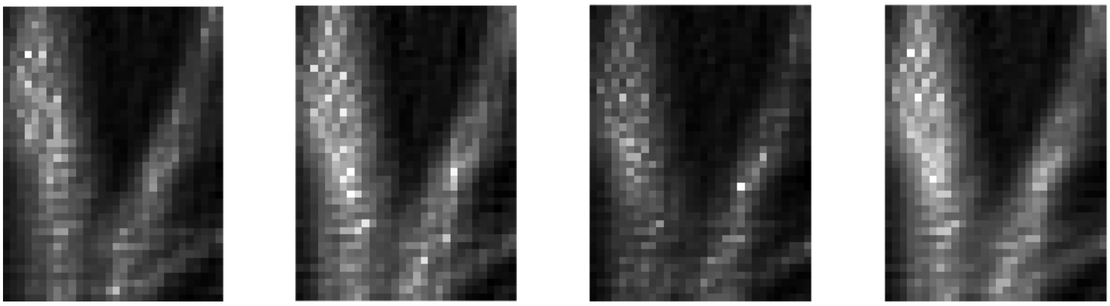

(a) Signals intensity at 20 GHz.

(b) Signals intensity at 19.75 GHz.

(c) Signals intensity at 19.50 GHz.

(d) Average of signals intensity from 19.5 to 20 GHz.

Figure 3.13: Images of the test result of the cactus-like plant for different individual frequencies and for the average of the frequency range from 19.5 GHz to 20 GHz.

3.3.2.2 Half-brown leaf

In this test, the leaf represented on the left side of figure 3.14 was scanned, with the red box representing the area covered by the scan. The leaf was directly extracted from the tree in this condition, with almost half of the leaf in a dry state. The scanning area of this test was a rectangle of 12 cm by 7 cm with a step size of 4 mm, corresponding to 540 different points.

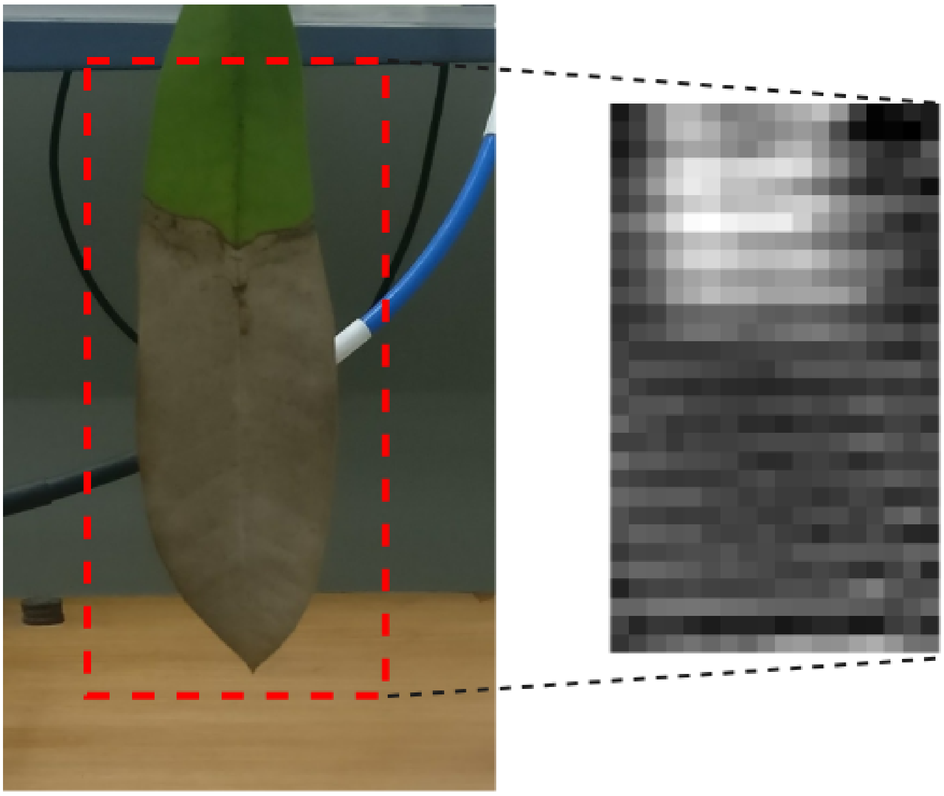

Figure 3.14: Leaf with a dry half and the respective result of the test scan.

As observed by the result of the test scan in figure 3.14, there is a brighter area in the top part of the resulting image, corresponding to the green portion of the leaf, presenting a higher water content in this area. The middle and bottom part of the resulting image shows a area corresponding to the dry part of the leaf. This correlates to the real image since the brown portion of the leaf has less water content in comparison to the green part.

3.3.2.3 Measurements of a leafs mass

This test consisted of starting with a green leaf freshly taken from a tree, measure its mass using a high precision scale and perform a scanning test. Next, the leaf was left to dry naturally for two days, before being again weighted and scanned. For this test, the size of the scanning area was a 12 cm by 8 cm rectangle with a step size of 4 mm, corresponding to a total of 600 different points. The images of the starting leaf and the resulting dry leaf are shown in figure 3.15.

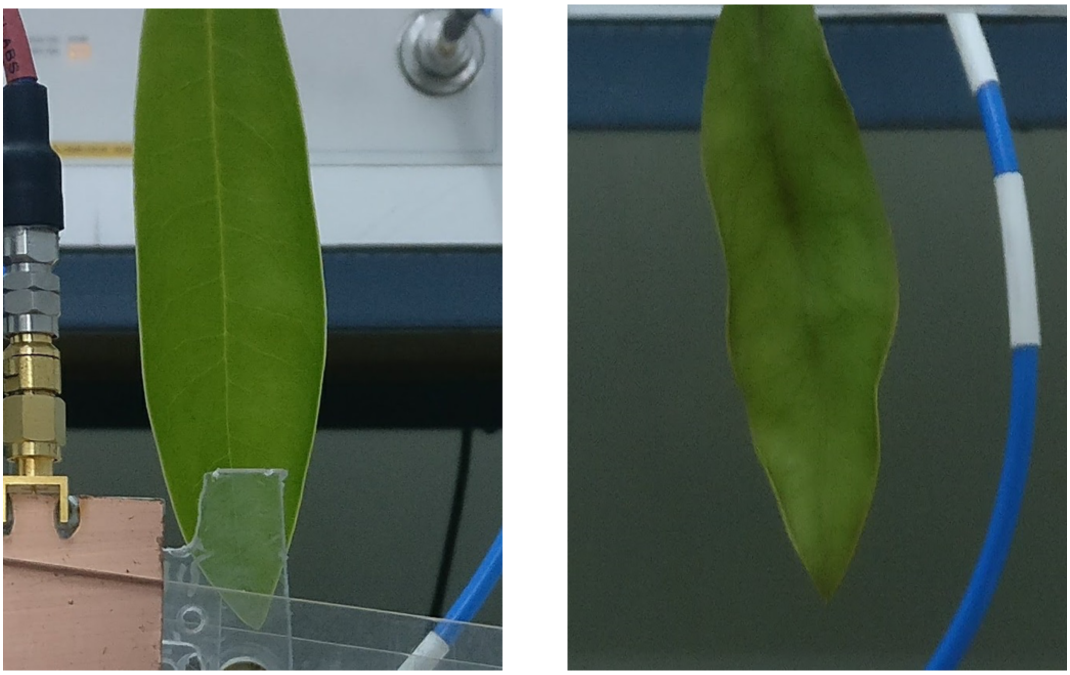

(a) Initial green leaf.

(b) Dry leaf.

Figure 3.15: Images of the green leaf used in this test during the first scan (a) and during the following scan two days later (b).

The weight of the leaf decreased between each scanning procedure, starting at 1.1094 grams and finishing at 0.3908 grams. This loss of weight by the leaf is mainly due to the evaporation of water during the natural drying process, since the physical structure of the leaf stayed intact during the drying process and the scanning procedures. This loss of weight corresponds to a loss of water by the leaf, thus affecting each test scan results. In figure 3.16, the results of this analysis are shown, where image 3.16a represents the result of the scan of the green leaf (with a mass of 1.1094 grams), image 3.16b represents the result of the dry leaf (with a mass of 0.3908 grams) and image 3.16c is the difference between the results of the green leaf and the dry leaf. The images were obtained by normalizing both matrices with the global maximum and minimum between the matrices acquired from both scanning procedures. The fact that the green leaf result has a brighter area in the zone of the leaf, whereas, on the dry leaf the result is a image almost black and uniform, indicates a clear sensibility of the system to the water content inside the leaf. The lack of a clear contrast between the dry leaf and the area of the image without the leaf in figure 3.16b indicates that there is not a significant attenuation of the signal due to the lack of water on the dry leaf.

The analysis of the sum of all the elements of the normalised matrices also gives a clear indication of the effects of the water content of the leaf on the signals attenuation. The sum of the values of the normalised matrix of the green leaf was 262.20, whereas, for the dry leaf this sum was 156.47. This difference is explained due to the fact that a greater attenuation of the signal is represented by a number closer to 1 on the matrix, thus giving a bigger sum of the elements of the matrix of the green leaf.

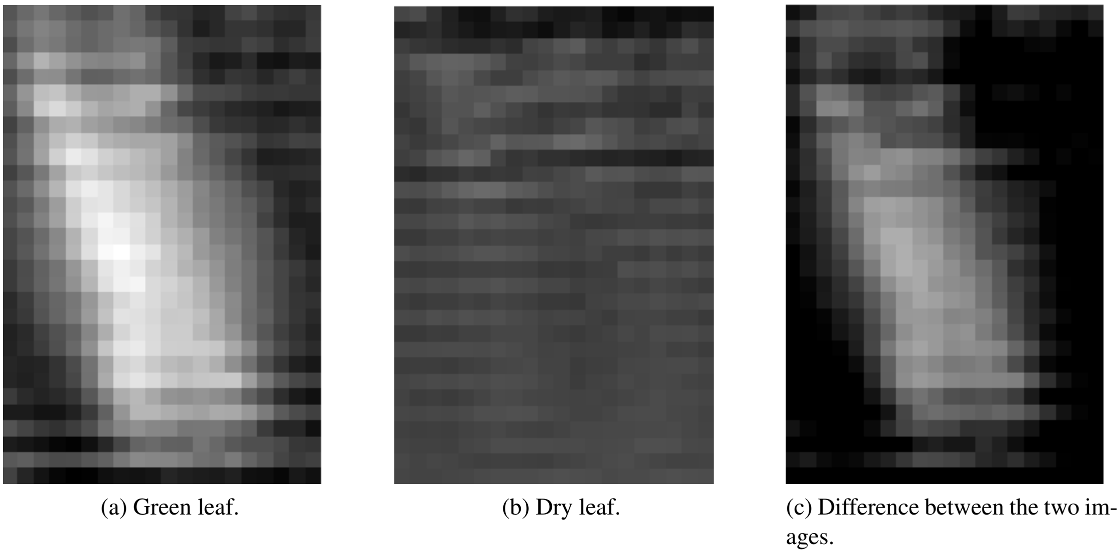

(a) Green leaf.

(b) Dry leaf.

(c) Difference between the two images.

Figure 3.16: Images of the analysis of a green leaf, a dry leaf and the difference between the two images.

The analysis of the difference between the maximum and minimum values recorded by the VNA also reveals some information about the leafs water content. For the data recorded for the green leaf, the difference between the maximum and the minimum values was 6.59 dB, whereas, on the dry leaf, this value was 2.57 dB. This difference of 4.02 dB between these two values reveals a clear indication of a greater effect on the signals attenuation with the green leaf.

The same test was repeated using the smaller claw, this time with the scanning procedure being repeated six times over the course of two days and the mass of the leaf being measured before each scan. The values of the leafs mass for each scanning procedure are shown in table 3.1, with the first three scans being performed on the first day and the following scans on the second day.

Table 3.1: Values of the leafs mass before each scan and corresponding difference between the maximum and minimum values of the matrices of each test result.

	Day 1			**Day 2**		
	Test 1	**Test 2**	**Test 3**	**Test 4**	**Test 5**	**Test 6**
Mass (g)	1.0472	0.9741	0.9336	0.6181	0.5652	0.5311
Difference Max - Min (dB)	3.87	3.74	3.73	1.92	1.86	1.58

The analysis of the difference between the maximum and minimum values of the data collected for each test reveals an indication of the effect of the leafs water content on the signals intensity. The higher the value of the leafs mass (corresponding to a higher water content), the higher the attenuation on the signals intensity, represented by a greater difference between the maximum and minimum values of the of the tests performed on the first day in relation to the tests on the second day, as shown in table 3.1.

3.3.2.4 Green leaf with water on the surface

The purpose of this test was to verify the effects on the test results for water on the surface of the leaves, simulating the possible conditions after a watering process of a plant. The scanning area of this test was a 10 cm by 7 cm rectangle with a step size of 4 mm, corresponding to 450 different points. Figure 3.17 shows the results of this test.

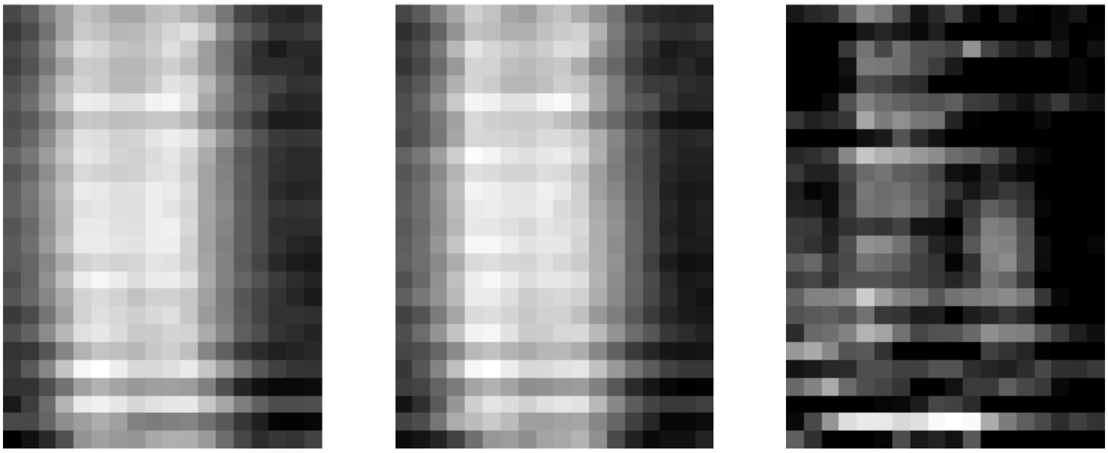

(a) Green leaf.

(b) Green leaf with water on the surface.

(c) Difference between the two images.

Figure 3.17: Images of the analysis of a green leaf (a), the analysis of the same leaf with water on its surface (b) and the difference between the two images (c).

Although the visual difference between figures 3.17a and 3.17b is almost none, the resulting difference of the two images, shown in figure 3.17c, shows some bright spots over the lower part of the image. These spots correspond to parts where the attenuation of the leaf with water on the surface is greater in relation to the same spot on the leaf without water on the surface. These bright spots are located in the lower part of figure 3.17c because the tests were performed from the bottom to the top part of the leaves, and therefore, due to gravity pulling down the drops of water over the leafs surface, the amount of water concentrated on the bottom part of the leaf was greater than at the top. The fact that the test took about two and a half hours to be completed was also a factor to this result as some of the water on the top part of the leaf evaporated before the scan passed over that part of the leaf. The analysis of the values of each matrix for the two tests also revealed that there is a bigger sum for the matrix of the leaf with water on its surface, which again confirms the effect of water on the signals intensity. The sum of the values of this matrix was 242.453, whereas, for the matrix of the values for the leaf without water, this sum corresponds to 230.723.

3.3.3 Sensibility to different water thicknesses

These tests consisted of analysing the sensibility of the signal to different amounts and thicknesses of water on a petri dish. The scanning ability of the robotic platform was not needed during these tests, so the claw holding the antennas was directly fixed to a table, with the pair of antennas facing each other in the vertical direction. Images of the setup for these tests are shown in figure 3.18.

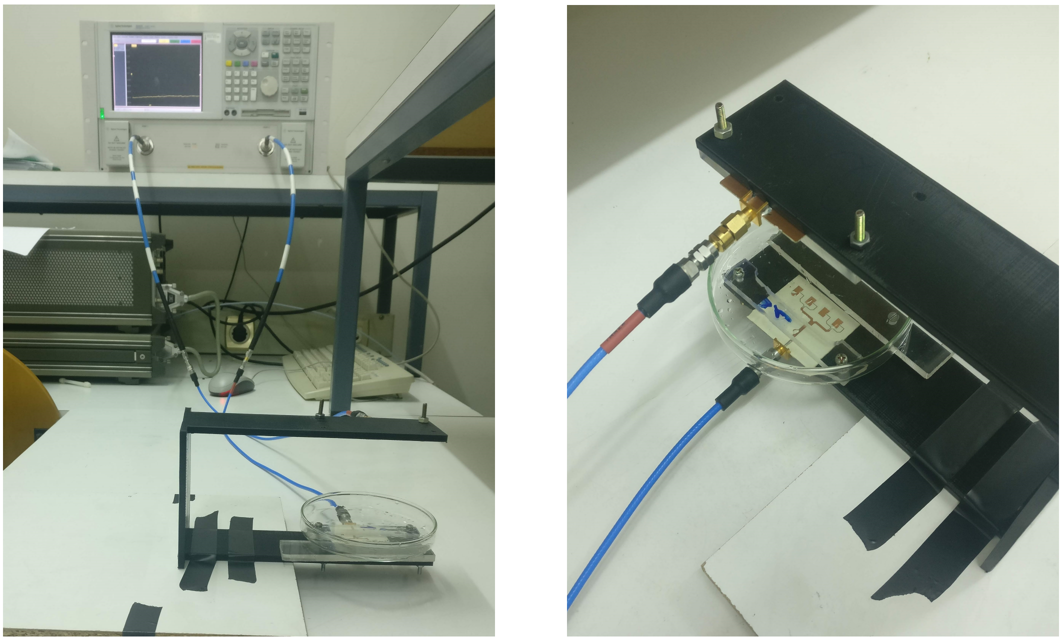

Figure 3.18: Setup for testing the sensibility of the signal to different quantities of water.

The tests results are shown in figures 3.19 to 3.22. These tests were performed using a petri dish since it does not influence the signals intensity. For each test, a measure was made with an empty petri dish to serve as a reference, represented by the line "REF" in figures 3.19 and 3.21, and by the red point in figures 3.20 and 3.22.

Seven measurements were made in the first test, where the first measurement was the reference measure, the second was a measure with 15 ml of water and each of following measures was made with an increase of 6 ml of water. Table 3.2 shows the quantity of water in the petri dish and the respective water thickness for each measurement. The amount of water for the first measure after the reference was 15 ml to completely cover the surface of the petri dish.

Table 3.2: Measurements for the first test with the petri dish.

Measurement	**Quantity of water (ml)**	**Water thickness (mm)**
REF	0	0
1	15	1.61
2	21	2.25
3	27	2.89
4	33	3.54
5	39	4.18
6	45	4.82

The analysis of figure 3.19 reveals a clear influence of water on the signals attenuation between the reference measure and measurement number "1", a difference of around 15 dB, which validates the perception part of the proposed concept. The analysis of lines "2" to "6" also reveals a sensibility of the signal to the different amounts of water, as the signals attenuation increases with the increase of the quantity of water in the petri dish. This fact is more noticeable in figure 3.20, where each point on the graph represents the average value of the attenuation for the different amounts of water. There is a steady increase in the average value of the attenuation with the increase of the amount of water until 27 ml, and a stabilization of the attenuation for values higher than 27 ml. This stabilization in the graphic is probably due to interference during the performed measurements, since a small movement in the petri dish can cause a slight variation in the signals intensity. Again, there is a clear difference in the signals attenuation between the measurement without water and the measurements with water, this is, between the value represented by the red dot and the values represented with the black dots.

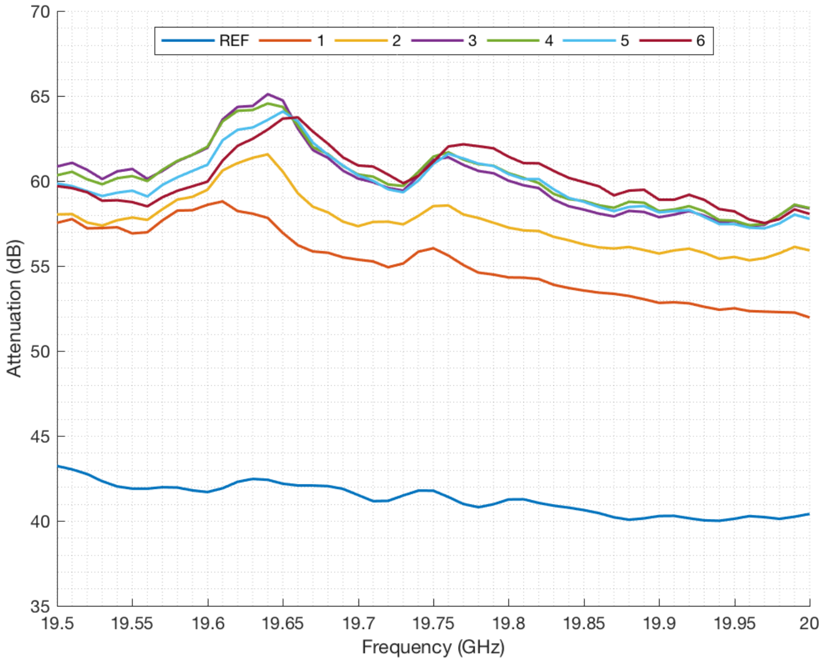

Figure 3.19: Results of the sensibility test using a petri dish.

The same test was repeated with a smaller water quantity increase (4 ml) between consecutive measurements and a higher final amount of water, corresponding to a higher number of measurements (22 in total). This allowed for a better understanding of the signals behavior to the different amounts of water. The first measurement was the reference, the second was with 20 ml of water, and the step size for the following measures was 4 ml. Table 3.3 shows the quantity of water, and the respective thickness, in the petri dish for each measurement.

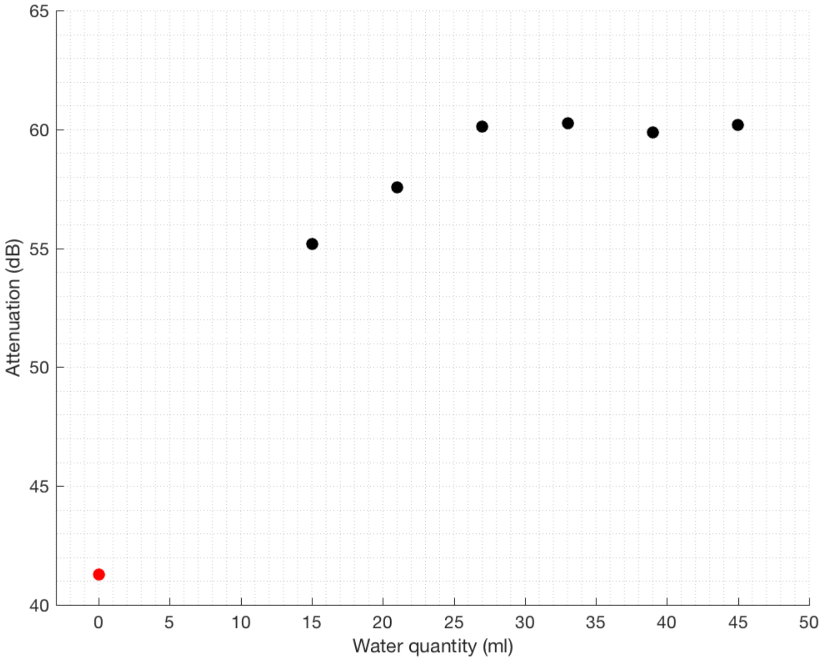

Figure 3.20: Results of the sensibility test using a petri dish, where each point represents the average of the attenuation for the frequency swipe from 19.5 to 20 GHz, for different amounts of water.

Table 3.3: Measurements for the first test with the petri dish. The values in bold are the measurements represented in figure 3.21.

Measurement	Quantity of water (ml)	Water thickness (mm)
REF	**0**	**0**
1	**20**	**2.14**
2	24	2.57
3	28	3.00
4	32	3.43
5	**36**	**3.86**
6	40	4.29
7	44	4.72
8	48	5.14
9	**52**	**5.57**
10	56	6.00
11	60	6.43
12	64	6.86
13	**68**	**7.29**
14	72	7.72
15	76	8.14
16	80	8.57
17	**84**	**9.00**
18	88	9.43
19	92	9.86
20	96	10.28
21	**100**	**10.72**

The results are shown in figures 3.21 and 3.22, with only 7 measurements being shown in figure 3.21 for better readability. As in the previous test, there is a clear indication of the perception ability of the system, noted by the difference of about 17 dB between line "REF" and "1". As for the quantification ability, the results in figure 3.22 show an increase in the signal's attenuation with the increase of the amount of water, as intended. The peak noted in figure 3.22 between 20 ml and 30 ml was caused by small interferences during the measurements such as a little movement of the petri dish, as was the case in the previous test.

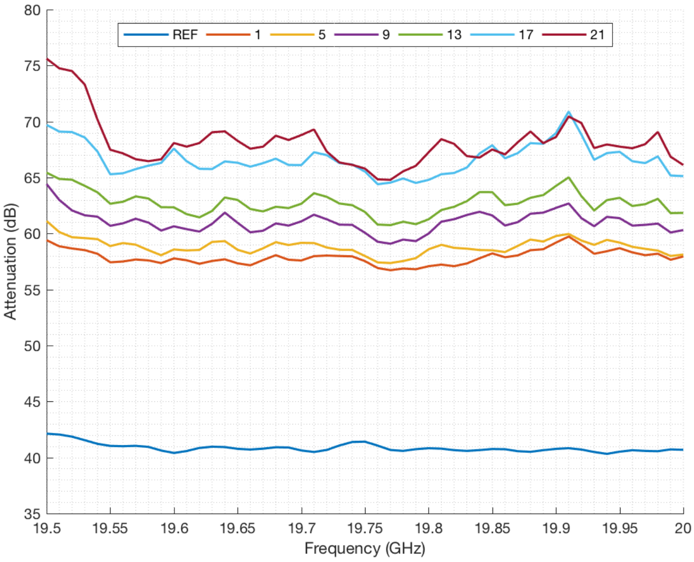

Figure 3.21: Results of the second sensibility test using a petri dish.

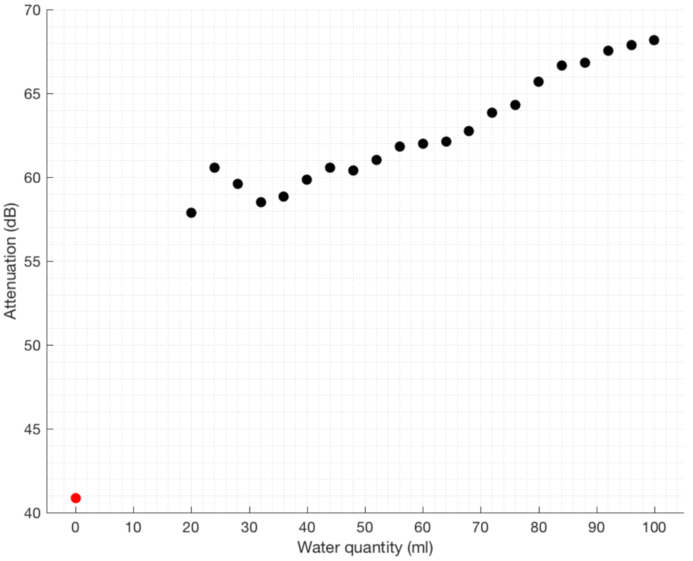

Figure 3.22: Results of the second sensibility test using a petri dish.

3.4 Review of the results

The overall results of the tests show a clear influence in the signals intensity with the presence of water on plants and leaves, and this influence validates the proposed concept. Furthermore, the results of the sensibility test with the petri dish revealed a clear indication that the technique is perfectly capable of detecting water and, with a more controlled experiment, the quantification ability of the technique for different water contents could be studied. As for the tests with the plastic bag and water bottle, the results showed the effects of the water on the signals intensity as well as the sensitivity to water droplets in the inner surfaces of the containers.

Due to the test equipment limitations such as the slow-moving speed of the robotic arm and the lack of input power from the VNA, the quantity and quality of the collected data did not meet the initial expectations. Nevertheless, the analysis of the collected data allowed for the validation the concept, as desired.

The use of coaxial cables to connect the pair of antennas to the VNA was an inhered necessity due to the existance of the moving parts of the robotic arm to perform the scan. However, at 20 GHz, the slight movements of the cables can induce interferences on the signals intensity due to its small wavelength, which can create small differences in the signals intensity in the same position of the scanning area in different tests. To decrease the effect of this problem, an idle state was introduced to the developed script after each movement and before the acquisition of data from the VNA, which increased the duration of the tests.

Chapter 4

Proposed System Design

During the tests, it was noticeable that a mechanic scan using the robotic arm was a time-consuming process. The velocity of the robotic arm was low to achieve better precision, and the need to wait for the stabilisation of the position of the arm after each move made the tests take a considerable amount of time. This amount of time is impracticable in a real-world situation and implementation, and therefore, it is necessary to analyze other implementations options to improve the velocity of the analysis and adequate the technique to a practical implementation. The easiest way to decrease the amount of time needed to analyze a plant is to use an electrical-based scan instead of a mechanical one. Instead of moving the pair of antennas using the robotic arm to scan a plant, the idea is to use the robotic arm to put the plant being analyzed between an emitter and a receptor. This emitter consists of an electronically steerable array of antennas known as a phased array, enabling the control of the direction of the beam and of the position being analyzed without the need to move the robotic arm.

All the equations and assumptions used in this chapter were taken from [29] and [30], unless stated otherwise.

4.1 System specification

There are diverse options for a possible implementation of the system using an electrical scanning over a mechanical one. For the implementation of the electrical scanning, two options emerged. The first consisted of two arrays of antennas serving as an emitter and receiver, where each element of the array would irradiate individually and only one at a time in opposite directions. This way, only one pair of opposing antennas would be activated at each given moment, with the intensity of the emitted signal being affected by the objects and plants directly in front of that pair of antennas. The electrical scan in this system would consist of controlling the switches connected to each antenna as shown in figure 4.1, turning on and off the different pairs of antennas in the arrays to scan the whole area.

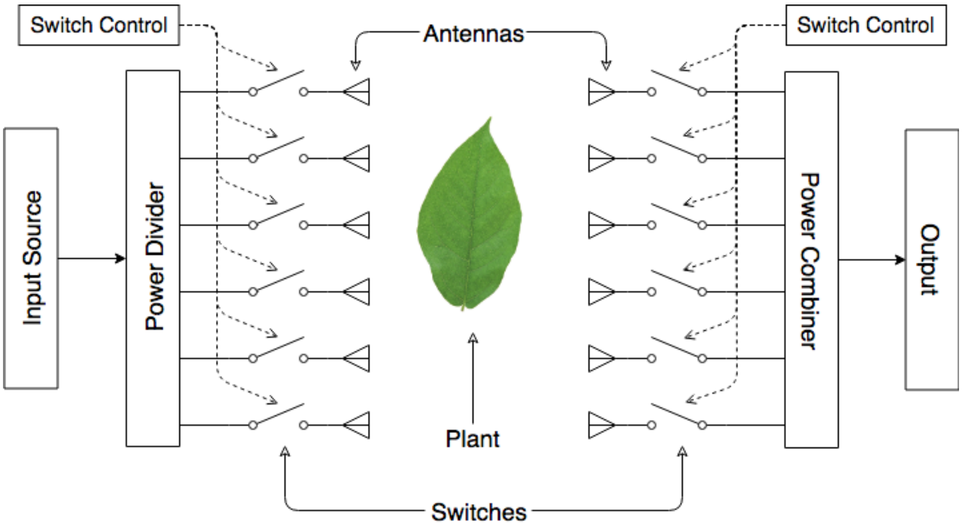

Figure 4.1: Diagram of the antenna array with switches.

Assuming that each letter of the following arrays represents an individual antenna, with the arrays facing each other with the plants between the two arrays as shown in figure 4.2, an example of a scanning procedure would work as shown in figure 4.3.

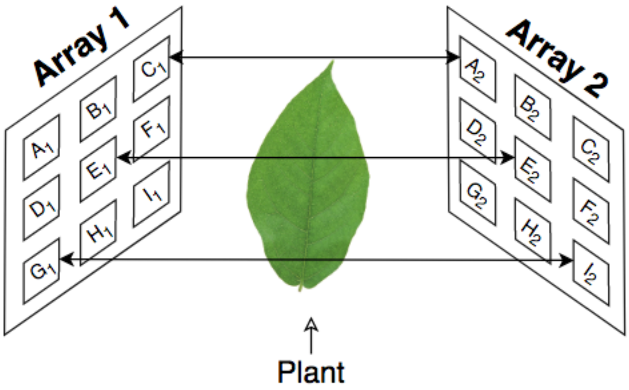

Figure 4.2: Arrays where each letter represents an antenna.

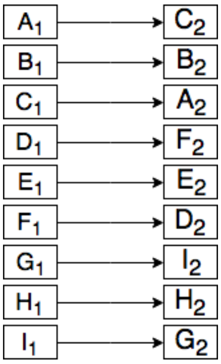

$A_1 \rightarrow C_2$
$B_1 \rightarrow B_2$
$C_1 \rightarrow A_2$
$D_1 \rightarrow F_2$
$E_1 \rightarrow E_2$
$F_1 \rightarrow D_2$
$G_1 \rightarrow I_2$
$H_1 \rightarrow H_2$
$I_1 \rightarrow G_2$

Figure 4.3: Sequence of a possible scanning with the two arrays of antennas facing each other, with the letters corresponding to the position represented in figure 4.2.

The second option consisted of developing a phased array of antennas as the emitter. In this configuration, all the antennas of the array would be emitting at the same time. The combination of the individual radiation patterns of each antenna of the array creates a beam, directing the radiation pattern of the array in a more specific direction, increasing the directivity. The change in the angle of the beam is achieved by shifting the phase of the signal emitted from each radiating element, to provide constructive or destructive interference so as to steer the beams in the desired direction. The direction of the beam is changed by controlling the phase shifters connected to each element of the array as shown in figure 4.4.

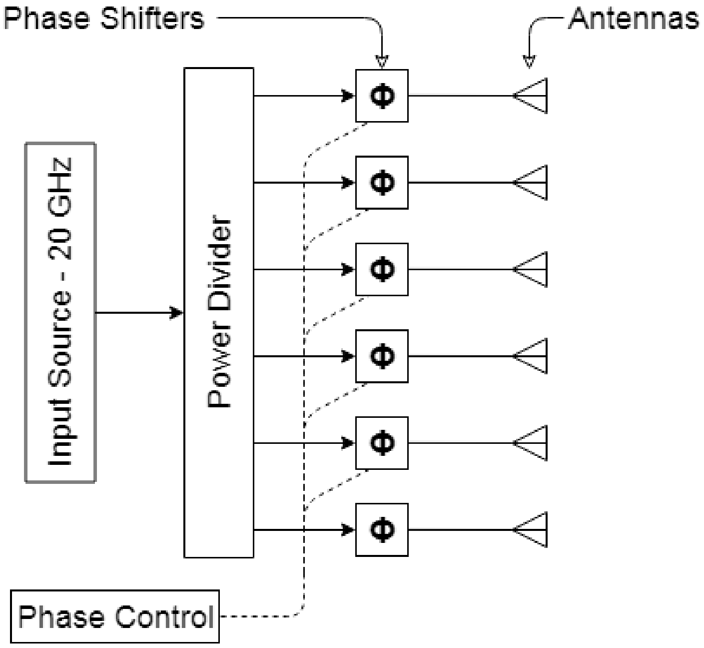

Figure 4.4: Diagram of the antenna array with the phase shifters.

For the development of this dissertation, the option chosen was the second one, with a phased array as the emitter. Due to time constraints, the focus was given only on the development of the antenna array for the emitter, being that for test purposes, the antenna used as a receptor was the same as an individual element developed for the array.

There are many factors to consider when designing an antenna for the development of a phased antenna array. Typical array designs include parameters such as the number of elements, array geometry, element spacing, and element tapering. Matlab was used to simulate and better understand the different effects of the parameters on the array performance and on the beamforming technique. For this implementation, the geometry of the array was defined as a rectangle. For a faster simulation in this phase of the analysis, an cosine antenna object of Matlab was used as the radiating element of the array. This object models an antenna element whose response follows a cosine function raised to a specified power in both the azimuth and elevation directions. The 3D radiation pattern of this element, with an equal specified power for both directions, is shown in figure 4.5.

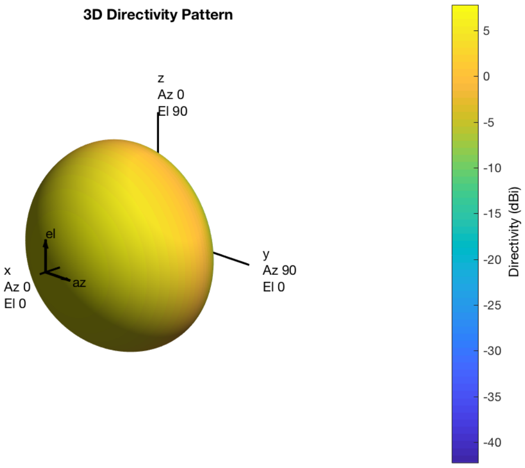

Figure 4.5: 3D radiation pattern of an ideal cosine antenna used during the simulations in Matlab.

Element tapering is a technique to reduce the effect of side lobes via amplitude control or weighting across the array aperture. This effect is simulated in Matlab by creating a matrix with a specific excitation amplitude for each element of the array. Figure 4.6 shows an image of the radiation pattern with element tapering versus an image without the tapering, where the presence of side lobes is obvious in the array without taper in figure 4.6b. The tapering technique comes with a trade-off between low side lobe levels and a loss in the main beam directivity, as shown by the lower directivity in figure 4.6a. In figure 4.6a, the maximum value of the directivity is around 25 dB, whereas, in figure 4.6b, the maximum value is around 30 dB.

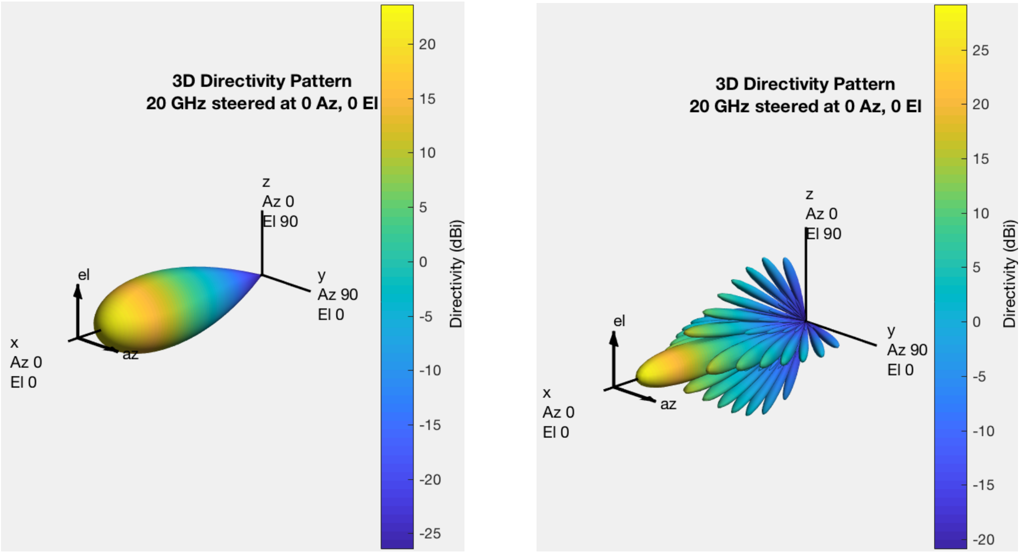

(a) 16 × 16 array with element tapering.

(b) 16 × 16 array without element tapering.

Figure 4.6: 16 × 16 array radiation pattern with element tapering (a) and without element tapering (b).

Figure 4.7 shows the different 3D radiation patterns for different numbers of elements in the array. As observed, the larger the number of elements in the array, the higher the directivity of the beam. There is an increase of around 15 dB from the maximum value in the 4x4 configuration (figure 4.7a) to the maximum value in the 32×32 configuration (figure 4.7d).

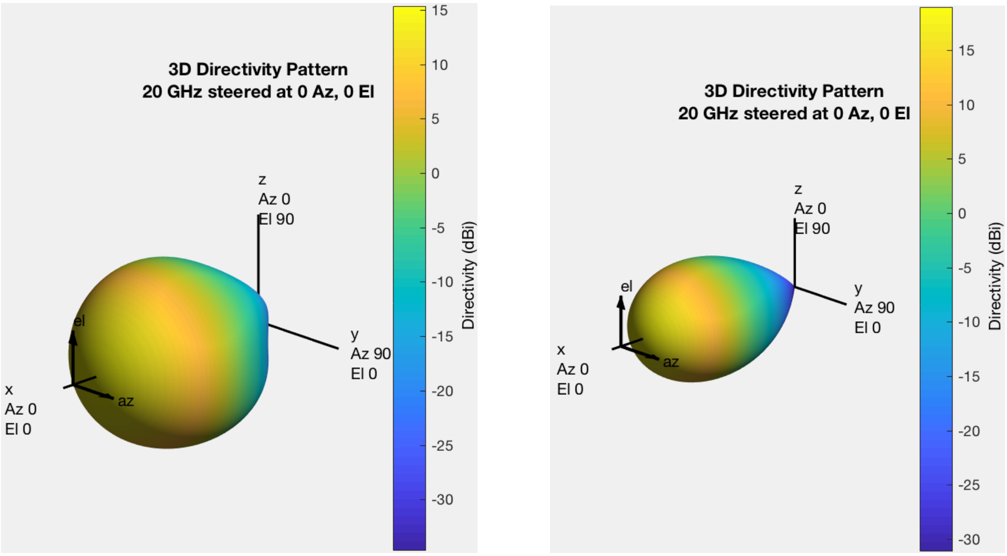

(a) 4×4 array radiation pattern.

(b) 8×8 array radiation pattern.

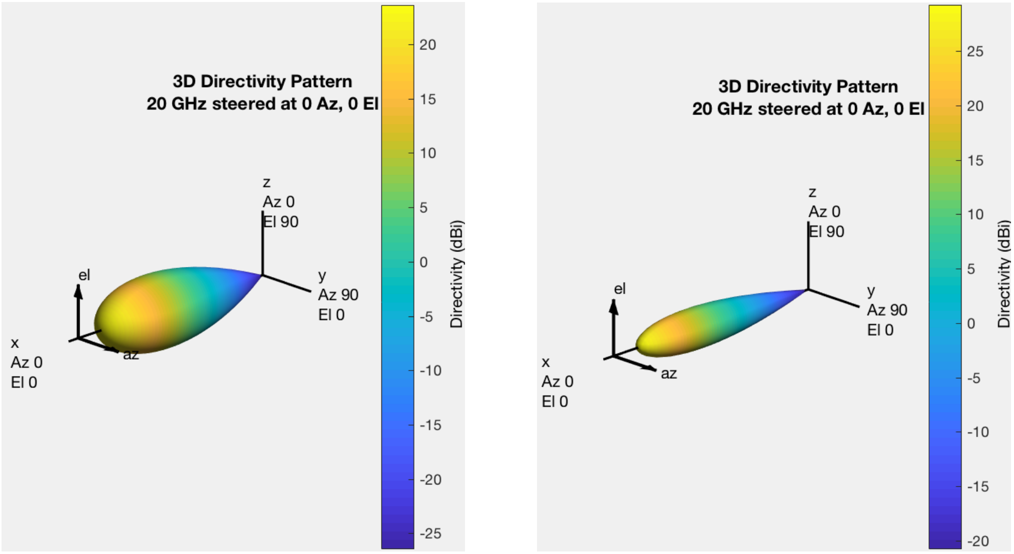

(c) 16×16 array radiation pattern.

(d) 32×32 array radiation pattern.

Figure 4.7: Radiation patterns for different number of elements.

As for the element spacing, this distance is normally defined as a fraction of the wavelength. Figure 4.8 shows the different 2D radiation pattern for four different element spacing. When the spacing between the elements is greater than half a wavelength, the effect of the side lobes is more pronounced, as is shown in the figures 4.8a and 4.8b.

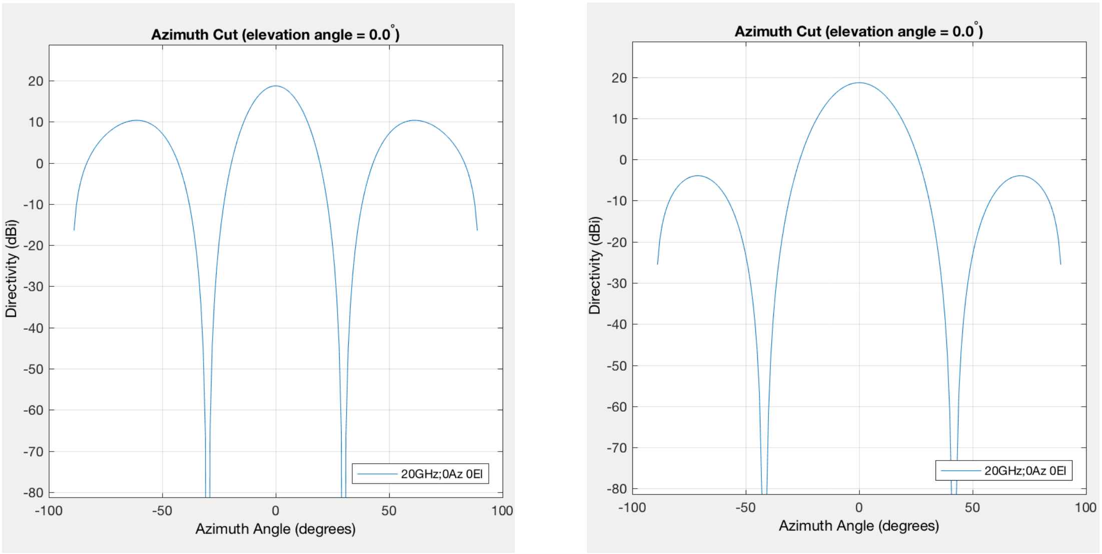

(a) 2D radiation pattern with an element spacing of a wavelength.

(b) 2D radiation pattern with an element spacing of 3 quarters of a wavelength.

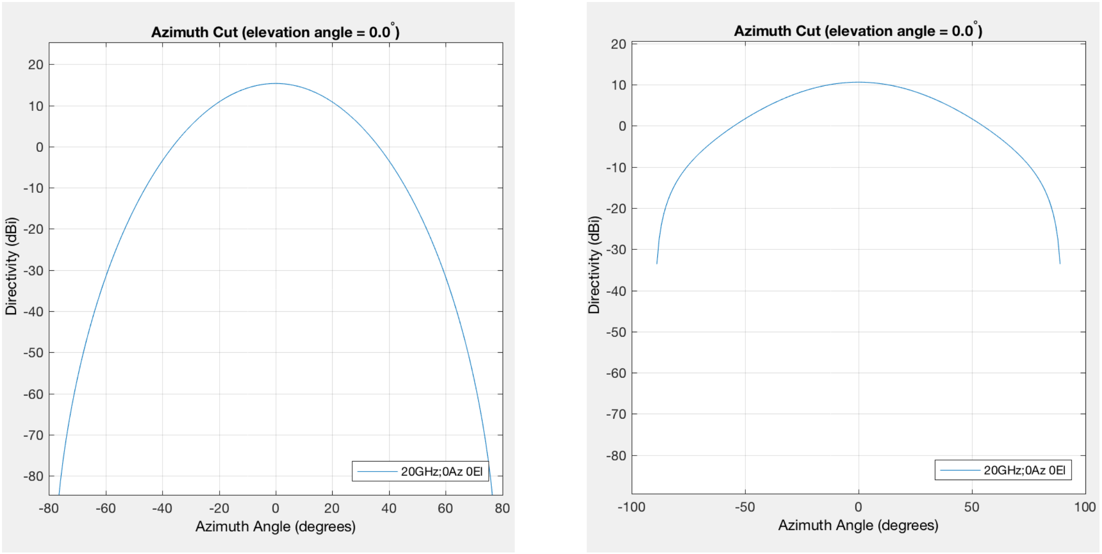

(c) 2D radiation pattern with an element spacing of half a wavelength.

(d) 2D radiation pattern with an element spacing of 1 quarter of a wavelength.

Figure 4.8: Radiation patterns for different element spacing.

Matlab also allows for the simulation of the steering the beam of the array. This steering is made possible by controlling the phase of the signal for each antenna, as stated above. To simulate this effect, Matlab creates a matrix with the phases of the signal for each different element of the array. The direction of the beam is defined by the phase difference between each consecutive element of the array. This phase difference $(\Delta\varphi)$ is obtained using equation 4.1, where d is the distance between the radiating elements, λ is the wavelength and θ_s is the desired angle of the beam.

$$\Delta\varphi = \frac{360^{o} \times d \times sin(\theta_s)}{\lambda} \tag{4.1}$$

Figure 4.9 shows the result of the simulation of a 16 × 16 array with tapering for an angle of 30° for the positive and negative directions of the azimuth and elevation axis. The element spacing is half of a wavelength and the phase difference between consecutive elements is 90°, calculated using equation 4.1.

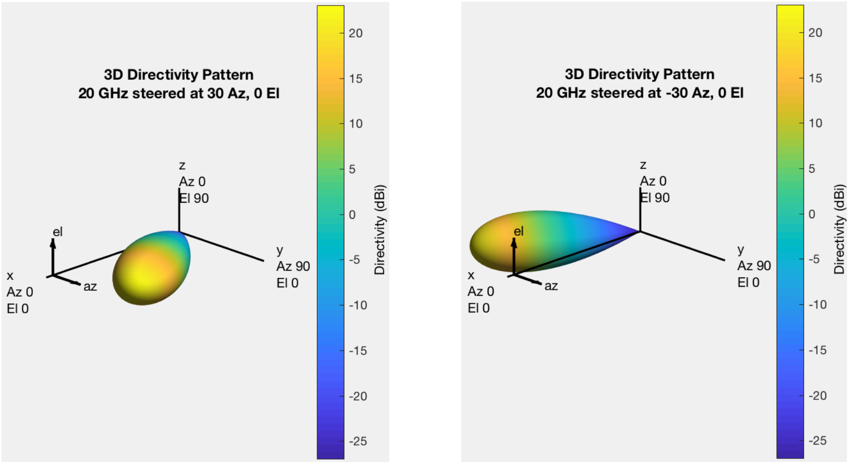

(a) Radiation pattern for a 30° angle in the azimuth direction.

(b) Radiation pattern for a -30° angle in the azimuth direction.

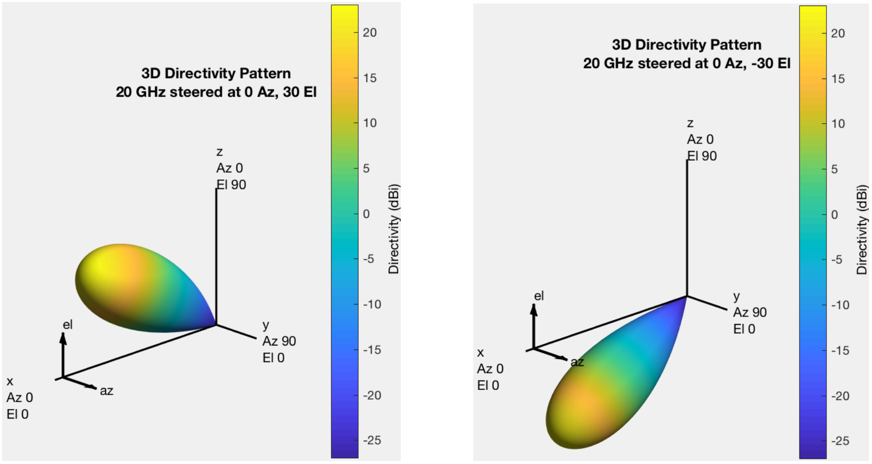

(c) Radiation pattern for a 30° angle in the elevation direction.

(d) Radiation pattern for a -30° angle in the elevation direction.

Figure 4.9: Simulation of the steering of the beam.

To create the array of antennas to be developed, the first thing to do is to decide the type of antenna. For this dissertation, the antenna chosen was a microstrip patch antenna, due to its characteristics and being prone to be used in an array configuration. It consists of a thin metallic strip placed a small distance above a ground plane, with a dielectric sheet, referred to as a substrate, in between. These antennas are low-profile, can be arranged in multiple configurations, are simple to manufacture using printed-circuit technology and are suitable for microwave frequencies. They also present some disadvantages such as low efficiency, low power, and narrow bandwidth, however, for the intended application, these disadvantages have no implications since no data will be sent (so a narrow bandwidth has no effects) and the conjugation of the various antennas in the array increases the gain.

The substrate defined for the development of these antennas was of the Rogers RO4000 Series. This series was selected due to its low dielectric constant and low tangent losses, along with the fact that is one of the families used by the PCB manufacturer. The 3D radiation pattern of the patch antenna using substrate Rogers 4003C, with a dielectric constant of 3.55, is shown in figure 4.10.

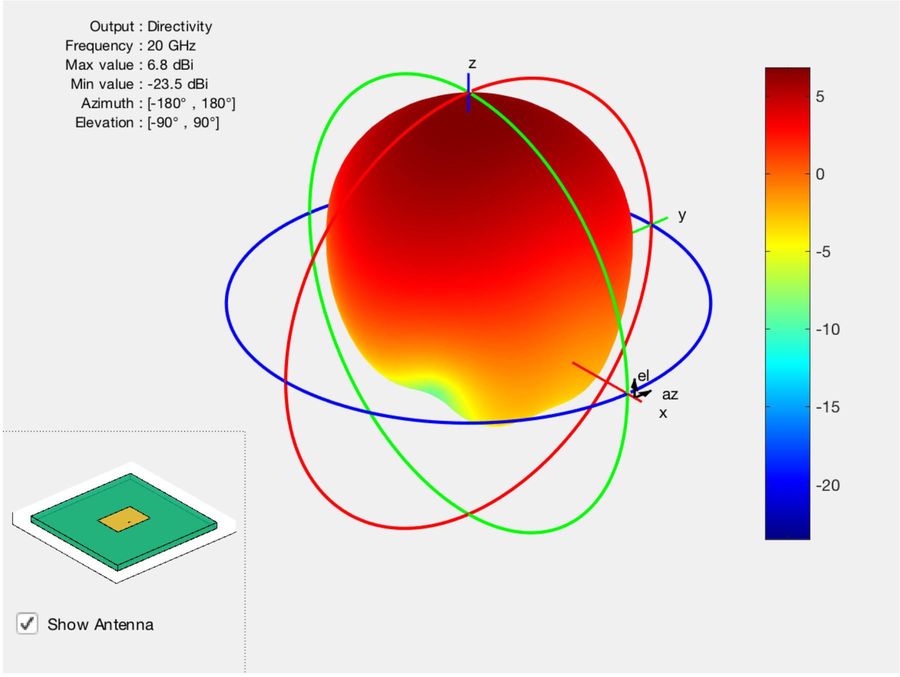

Output : Directivity
Frequency : 20 GHz
Max value : 6.8 dBi
Min value : -23.5 dBi
Azimuth : [-180° , 180°]
Elevation : [-90° , 90°]

Figure 4.10: Radiation pattern of the microstrip patch antenna, simulated in Matlab.

Due to computing power limitations, as well as limitations in the test equipment, the size of the array chosen for this implementation was a 4 × 2 array, with the capability of controlling the array only in the vertical direction, with phase shifters in the four lines of the array. This array consisted of four pairs of patch antennas, where the control of the phase of the input signal for each of the four pairs allows for the control of the angle of the beam in the vertical direction.

The available budget for this dissertation was limited and the cost of analog or digital phase shifters suitable for 20 GHz was relatively high, so, to enable the tests of the developed phased array, the phase shift for each antenna was achieved using microstrip lines of different lengths. The basic configuration of the system that was developed and tested is shown in figure 4.11. Each connection between the blocks was made with SMA connectors to allow changing the different microstrip line lengths between the different antennas.

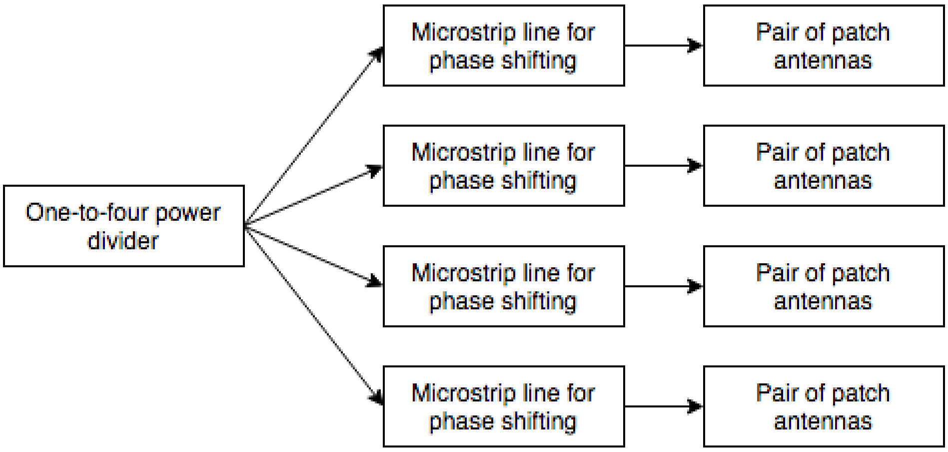

Figure 4.11: Basic system configuration were each connection between the blocks was made with SMA connectors.

4.2 Patch antenna design

The method of analysis of the microstrip patch to be used during this subsection is the transmission-line model, as it is the easiest of all the methods and gives a good physical insight.

For a microstrip patch antenna, the radiating patch can be a diverse number of shapes such as a square, rectangular, circular or triangular. For this implementation, the shape in use is a rectangle, due to the ease of analysis and dimensioning and for being the most widely used configuration. The microstrip line feed configuration was chosen as the feeding method for the patch. An inset feed was also used to facilitate the impedance matching of the antenna to the desired impedance of 100 Ω. Figure 4.12 shows the basic layout of the patch antenna with the microstrip feed line and the inset, where:

- W_p is the width of the patch;
- L_p is the length of the patch;
- W_f is the width of the feed line;
- L_f is the length of the feed line;
- y_0 is the length of the inset feed;
- g is the gap between the feed and the antenna.

The development of an individual microstrip patch antenna started by calculating the width and length of the said antenna. For this, equations 4.2 to 4.7 were used, where ε_r is the dielectric constant of the substrate, h is the height of the substrate, f_r is the resonant frequency and c is the speed of light in vacuum.

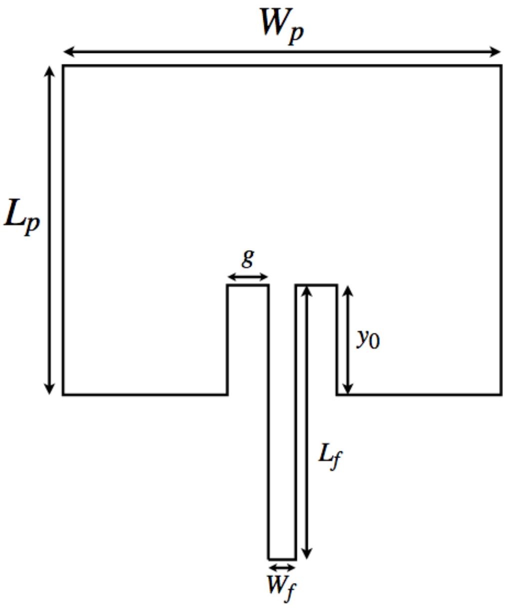

Figure 4.12: Parameters used during the parametric simulations to dimension the antenna to operate at the desired frequency.

Equation 4.2 calculates the width of the patch.

$$W_p = \frac{c}{2f_r}\sqrt{\frac{2}{\varepsilon_r+1}} \tag{4.2}$$

Equation 4.3 calculates the effective dielectric constant of the propagation medium.

$$\varepsilon_{reff} = \frac{\varepsilon_r+1}{2} + \frac{\varepsilon_r-1}{2}\left[1+12\frac{h}{W_p}\right]^{-1/2} \tag{4.3}$$

Because of fringing effects that occur in the substrate between the patch and the ground plane, electrically the patch of the microstrip antenna looks greater than its physical dimensions. Therefore, the physical length of the antenna is extended on each end by a distance ΔL, given by equation 4.4.

$$\Delta L = h \times 0.412\frac{(\varepsilon_{reff}+0.3)(\frac{W_p}{h}+0.264)}{(\varepsilon_{reff}-0.258)(\frac{W_p}{h}+0.8)} \tag{4.4}$$

Since the length of the patch has been extended by ΔL on each side, the effective length of the patch is determined by equation 4.5.

$$L_{eff} = L_p + 2\Delta L \tag{4.5}$$

The value of the effective length of the patch can be obtained using equation 4.6.

$$L_{eff} = \frac{c}{2f_r\sqrt{\varepsilon_{reff}}} \tag{4.6}$$

Lastly, the physical length of the patch is achieved by solving equation 4.5 in order of L_p, as shown below, in equation 4.7.

$$L_p = L_{eff} - 2\Delta L \tag{4.7}$$

The values used during this phase were base on the characteristics of the substrate Rogers RO4003C which has a dielectric constant of $\varepsilon_r = 3.55$. The substrate thickness was chosen based on the available options for this parameter on the datasheet. A resume of the characteristics for the development of the antenna in this initial phase is shown in table 4.1. Using these values, and the above equations, the theoretical values for the width and length of the patch were $W_p = 4.969\,\text{mm}$ and $L_p = 3.873\,\text{mm}$, respectively.

Table 4.1: Characteristics of the parameters for the first phase of the development of the antenna.

Parameters	**Characteristics**
Substrate type	Rogers RO4003C
Dielectric constant (ε_r)	3.55
Thickness (h)	0.305 mm
Resonant frequency (f_r)	20 GHz
Input Impedance	50 Ω

The antenna was developed for an input impedance of 100 Ω since the aim was to join two antennas to form a pair of antennas. This way, the junction of two 100 Ω antennas would create a 50 Ω line, without the need of using tapers to change the impedance of the line. This impedance matching of the antenna was made possible by the inset made along the width of the patch. The longer the inset feed inside the patch, the lower the impedance of the antenna. The initial value of the length of the inset feed (y_0) was calculated using the following set of equations.

Equation 4.8 calculates the wavenumber (k) of a wave.

$$k = \frac{2\pi}{\lambda} \tag{4.8}$$

The conductance (G_1) is expressed as

$$G_1 = \frac{I_1}{120\pi^2} \tag{4.9}$$

where

$$I_1 = -2 + \cos(X) + XS_i(X) + \frac{\sin(X)}{X} \tag{4.10}$$

$$X = kW_p \tag{4.11}$$

The conductance G_{12} is calculated using equation 4.12.

$$G_{12} = \frac{1}{120\pi^2} \int_0^{\pi} \left[\frac{\sin\left(\frac{kW_p}{2}\cos\theta\right)}{\cos\theta} \right]^2 J_0(kL_p \sin\theta)\sin^3\theta \, d\theta \tag{4.12}$$

where J_0 is the Bessel function of order zero.

The resonant input resistance is given by equation 4.13.

$$R_{in} = \frac{1}{2(G_1 + G_{12})} \tag{4.13}$$

Finally, the length of the inset feed is calculated by equation 4.14

$$y_0 = \frac{L_p}{\pi} \arccos\left(\frac{\sqrt{R}}{R_{in}}\right) \tag{4.14}$$

where R is the value of the desired impedance of the patch.

The result of this set of equations with $R = 100\,\Omega$ was $y_0 = 1.157\,\text{mm}$.

The gap (g) between the inset feed and the patch antenna was defined as a ratio of the width of the patch, with $g = W_p/20$. The width of the microstrip feed line was calculated solving equation 4.15, and the result was $W_f = 0.172\,\text{mm}$. The length of the feed line does not cause significant changes in antenna behavior so its initial value was set to 4 mm. A resume of the initial values for the different parameters of the patch antenna is shown in table 4.2.

$$Z_0 = \begin{cases} \frac{60}{\sqrt{\varepsilon_{reff}}} ln\left(\frac{8h}{W_f} + \frac{W_f}{4h}\right) & \text{for } W_f/h \leq 1 \\ \frac{120\pi}{\sqrt{\varepsilon_{reff}}\left[W_f/h + 1.393 + 0.667 ln\left(W_f/h + 1.444\right)\right]} & \text{for } W_f/h \geq 1 \end{cases} \tag{4.15}$$

Table 4.2: Initial values of the patch parameters.

Patch Parameter	**Dimension (mm)**
Patch width (W_p)	4.969
Patch length (L_p)	3.873
Feed width (W_f)	0.172
Feed length (L_f)	4
Inset feed length (y_0)	1.157
Feed gap (g)	0.248

After reaching the dimensions of the patch through the above equations, the next step was to simulate the individual patch using ANSYS HFSS: High Frequency Structure Simulator. ANSYS HFSS is a 3D electromagnetic (EM) simulation software for designing and simulating high-frequency electronic products such as antennas, antenna arrays, RF or microwave components [31].

The first step was to create and simulate an object in the HFSS environment. The design of this object consisted of the creation of a solid made of Rogers RO4003C, with a height of 0.305 mm, and two sheets of metal, one in the top and one in the bottom of this solid. Both sheets were made of copper, with the bottom sheet representing the ground plane and the top sheet representing the patch with the calculated dimensions. Figure 4.13 shows the design of the patch antenna in HFSS, where the lighter area represents the substrate. The area of the substrate was calculated such that there was at least a half-of-a-wavelength distance from the end of the patch design to the end of the substrate.

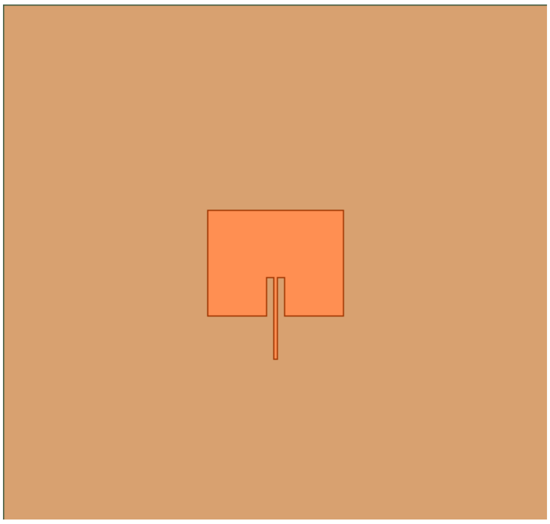

Figure 4.13: Design of the initial patch in HFSS.

The developed antenna, with the dimensions of the parameters presented in table 4.2, was simulated to extract the values of the S_{11} parameter of the antenna, and the results are shown in figure 4.14.

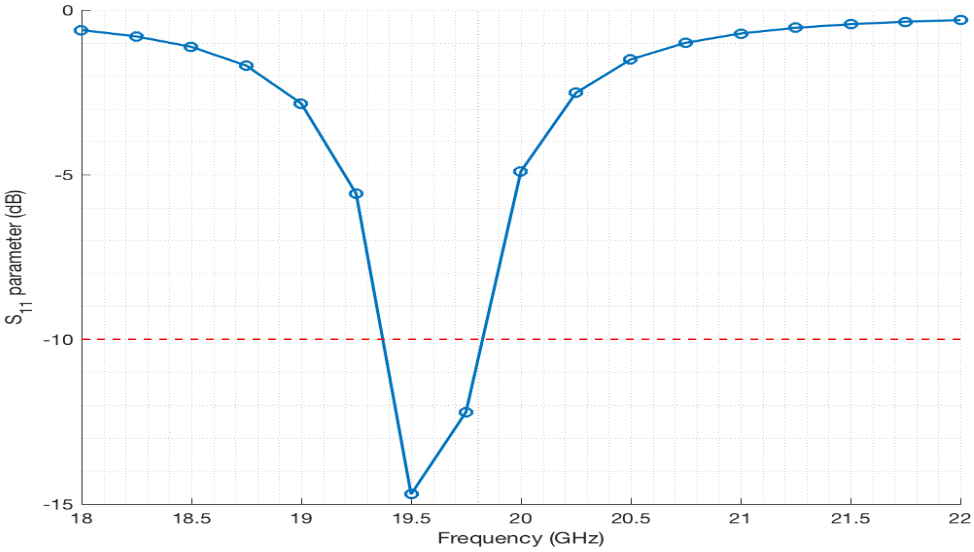

Figure 4.14: S_{11} parameter of the first simulation of the patch antenna with the parameters of table 4.2.

As observed in figure 4.14, the value of the S_{11} parameter has a value greater than $-10\,\mathrm{dB}$ at 20 GHz and the negative peak of the graph is at 19.5 GHz. The behavior of the patch was, therefore, different from what was desired. To solve this problem, the parametric simulation of HFSS was used to tune the different parameters of the patch in order to improve its performance at the desired frequency. This parametric simulation allows for the simulation of multiple values and combinations for each parameter and the analysis of the results of these simulations allows for the tuning of the different parameters to achieve the desired behavior of the antennas.

The first parametric simulation was performed to change the resonant frequency of the antenna to 20 GHz. The resonant frequency of the patch antenna is mainly determined by its length L_p, so this parameter was simulated from 3.75 mm to 3.85 mm with a step size of 0.05 mm. The result of this simulation is presented in figure 4.15.

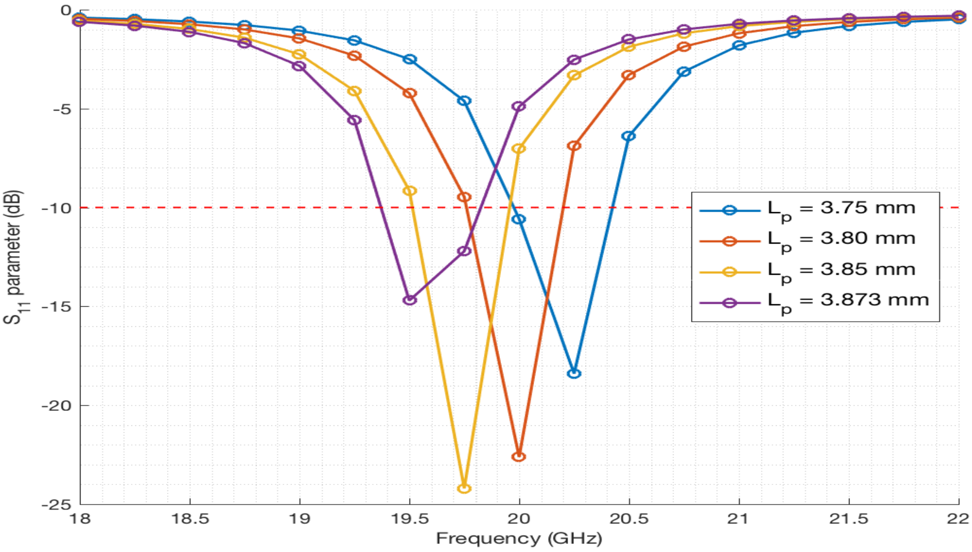

Figure 4.15: S_{11} parameter of the parametric simulation of the patch length L_p.

After analyzing the results, the value of the patch length was changed to 3.8 mm, since the lowest value at 20 GHz was achieved with that length. The next step was to improve the performance of the antenna. To achieve this, a new parametric simulation was performed, this time changing the values of the feed inset length (y_0), from 1.1 mm to 1.5 mm with a step size of 0.1 mm, and of the feed line width (W_f), from 0.1 mm to 0.25 mm with a step size of 0.05 mm. Figure 4.16 shows part of the resulting S_{11} parameters of the simulated combinations, showing only the combinations where the result was as desired for a better visualization.

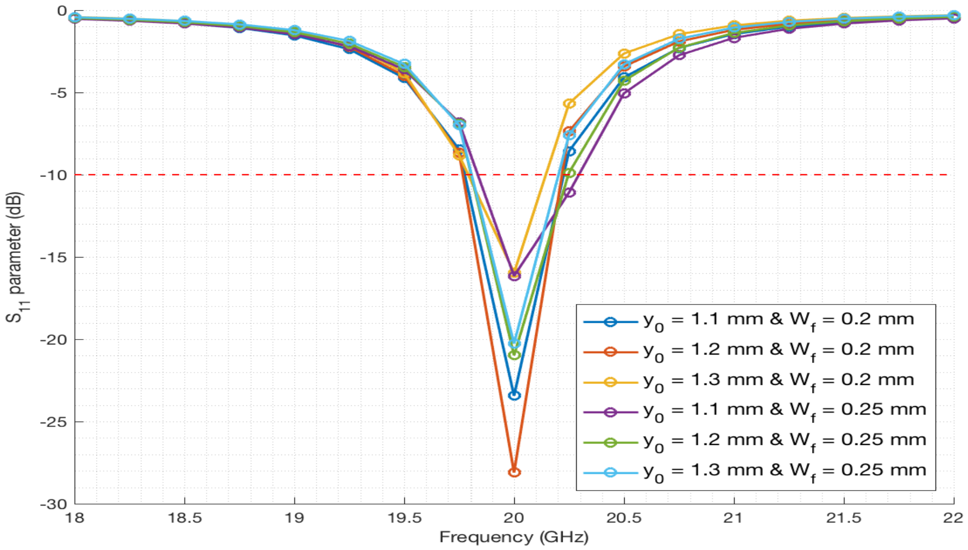

Figure 4.16: S_{11} parameter of the parametric simulation of the feed inset length (y_0) and of the feed line width (W_f).

By analyzing figure 4.16, the combination that produces the best result is $y_0 = 1.2\,\text{mm}$ and $W_f = 0.2\,\text{mm}$, with a value of -28.11 dB at 20 GHz.

The last parametric simulation for the patch antenna was performed to test the effects of the feed line length (L_f). In theory, the length of the feed line does not change the behavior of the antenna, only affecting the negative peak value of the patch at the resonant frequency. By analyzing figure 4.17, the change of the feed length only changed the value of the S_{11} parameter for the resonant frequency, as expected.

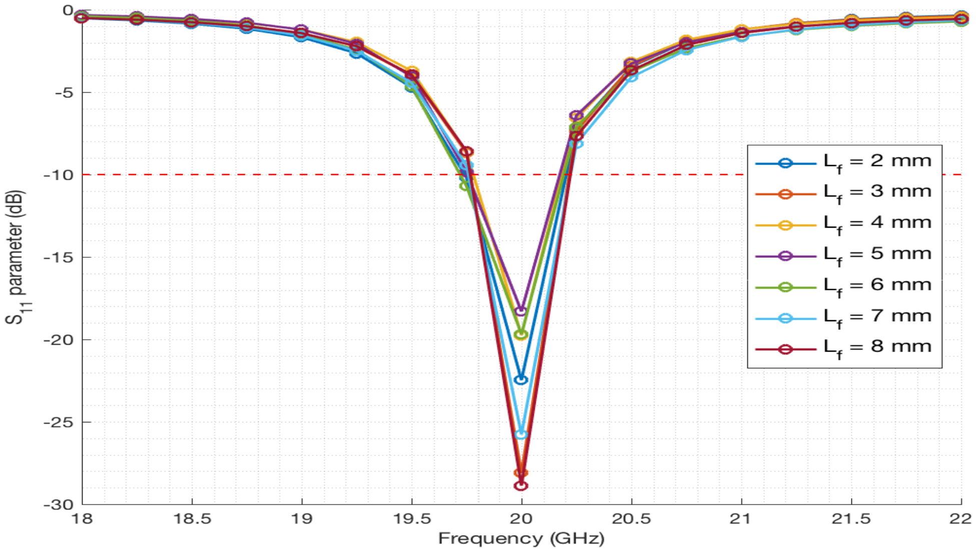

Figure 4.17: S_{11} parameter of the parametric simulation of the feed line length (L_f).

Table 4.3 shows the final values of the patch parameters obtained after the various parametric simulations.

Table 4.3: Final values of the patch parameters after the parametric simulations.

Patch Parameter	**Dimension (mm)**
Patch width (W_p)	4.969
Patch length (L_p)	3.8
Feed width (W_f)	0.2
Feed length (L_f)	4
Inset feed length (y_0)	1.2
Feed gap (g)	0.248

4.3 Antenna array design

As stated above, the array to be implemented was a 4 x 2 array with four pairs of antennas connected to an input feed by a power divider. This pair of antennas was created by combining two patch antennas with the same dimensions as specified in table 4.3. Figure 4.18 shows the initial design of the pair of antennas in HFSS. Both antennas are separated by a half-of-a-wavelength distance and are connected in the middle by a microstrip line calibrated to a $50\,\Omega$ impedance. The width of this line was calculated using equation 4.15. The input of the pair of antennas was matched to a $50\,\Omega$ impedance.

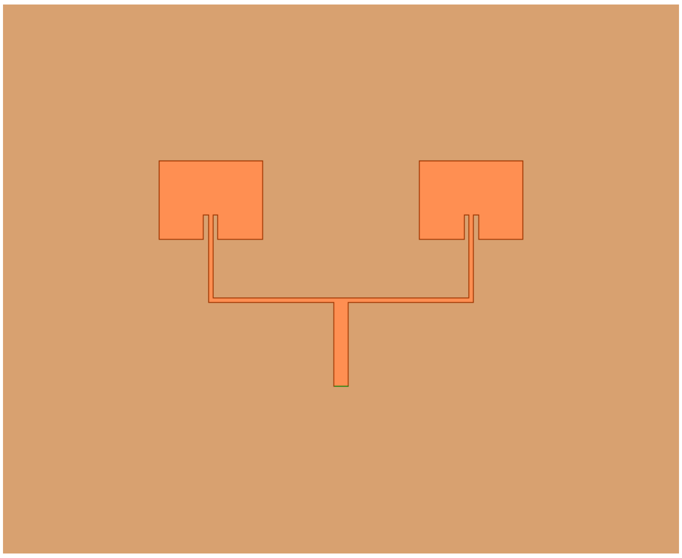

Figure 4.18: Initial design of the pair of the patch antennas in HFSS.

The pair of antennas was simulated in HFSS and the result is shown in figure 4.19.

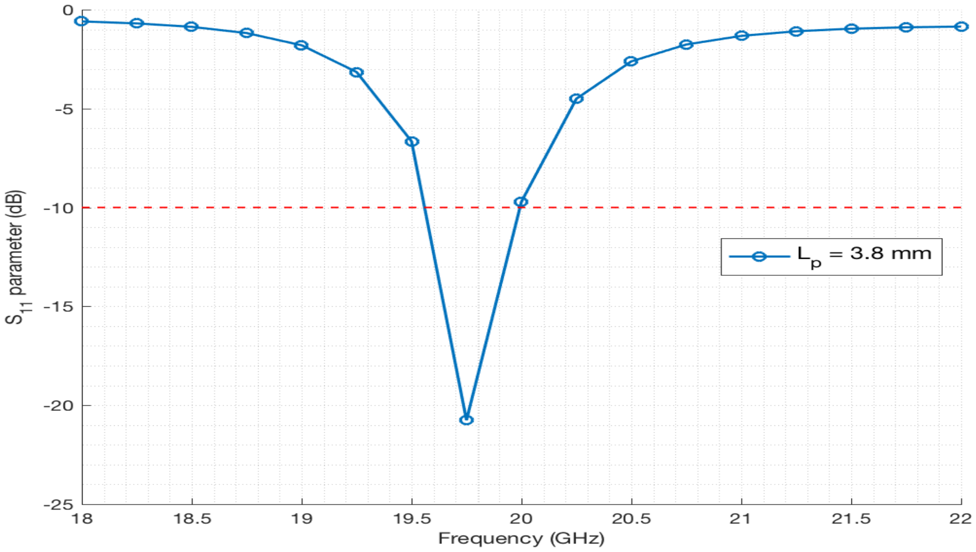

Figure 4.19: S_{11} parameter of the simulation of the pair of antennas.

As observed in figure 4.19, the S_{11} parameter of the pair of antennas displayed a small shift of the resonant frequency to 19.75 GHz. This was corrected by performing a parametric simulation, changing the patch length from 3.70 mm to 3.75 mm with a step size of 0.05 mm. The results of this simulation are displayed in figure 4.20.

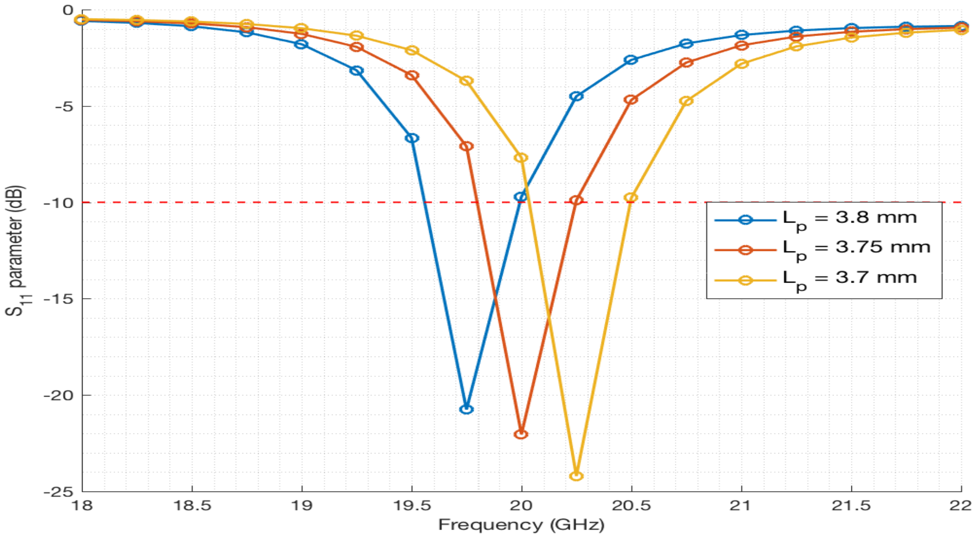

Figure 4.20: S_{11} parameter of the parametric simulation of the patch length (L_p) for the pair of antennas.

The analysis of figure 4.20 reveals that with a patch length (L_p) of 3.75 mm, the behavior of the pair of antennas is as intended.

Another parametric simulation was performed, this time changing the value of the length of the 50 Ω microstrip line (L_{50}) from 1 mm to 4 mm with a step size of 1 mm. Again, the aim of this simulation was to verify that changing the length of the 50 Ω feed line did not change the behavior of the pair of antennas. The results of this simulation are presented in figure 4.21.

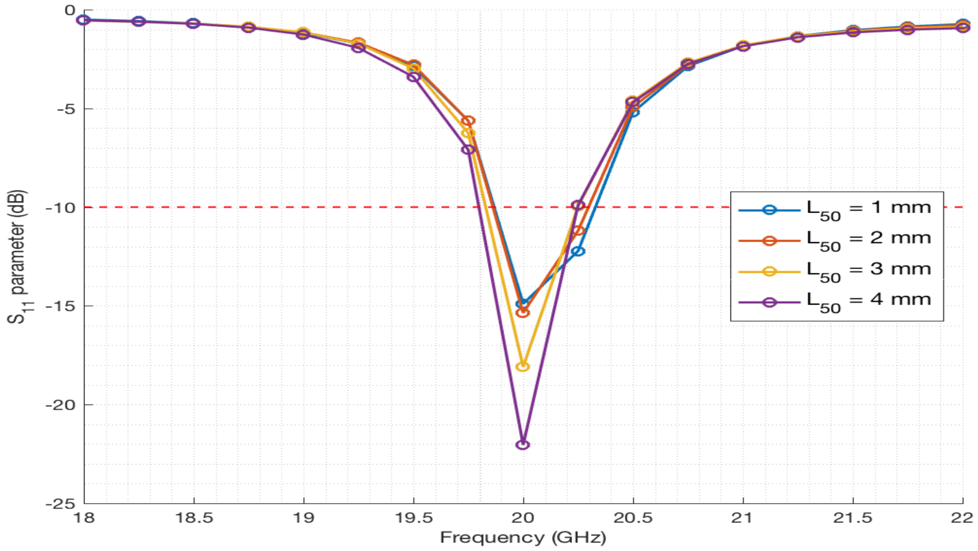

Figure 4.21: S_{11} parameter of the parametric simulation of the length of the 50 Ω microstrip line (L_{50}).

As observed in figure 4.21, the length of the 50 Ω microstrip line did not change the behavior of the pair of antennas, only changing the negative peak value of the S_{11} parameter at the resonant frequency, as was the case in figure 4.17.

To facilitate the development of the feeding circuitry for the pairs of antennas and to enable them to be positioned so as to obtain the desired beam, the 50 Ω microstrip line was changed and extended to allow the feeding from the side of the pair of antennas, as shown in figure 4.22.

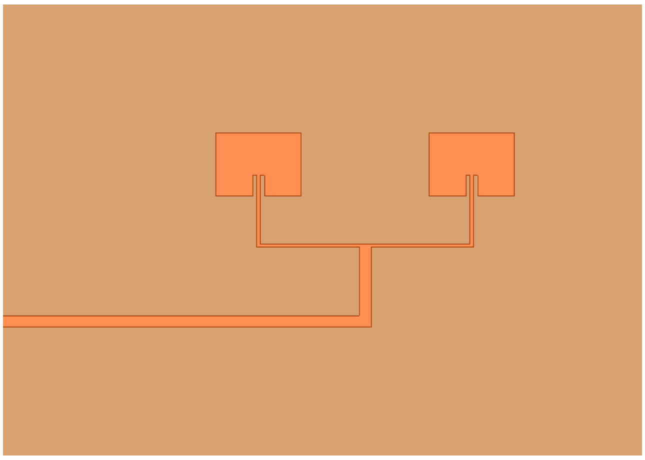

Figure 4.22: Design of the pair of the patch antennas with the lateral feed.

The design shown in figure 4.22 was simulated in HFSS and the result is shown in figure 4.23.

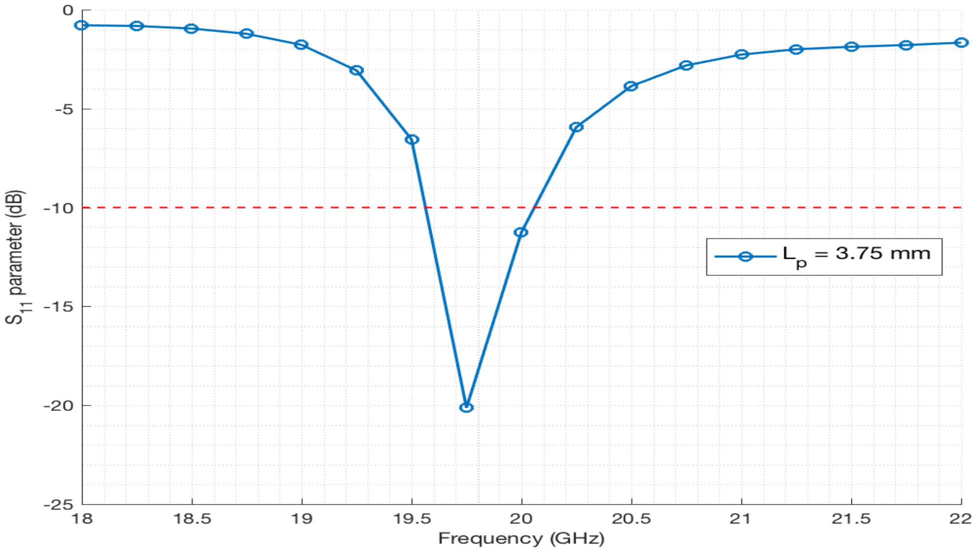

Figure 4.23: S_{11} parameter of the pair of antennas with the lateral feed.

As observed, there was a slight shift of the negative peak and the value of the S_{11} parameter at 20 GHz for this configuration was $-11.26\,\text{dB}$. A parametric simulation was performed by changing the value of the patch length (L_p) from 3.65 mm to 3.7 mm with a step size of 0.05 mm to improve the behavior of the antenna with the lateral feed, and the results are shown in figure 4.24.

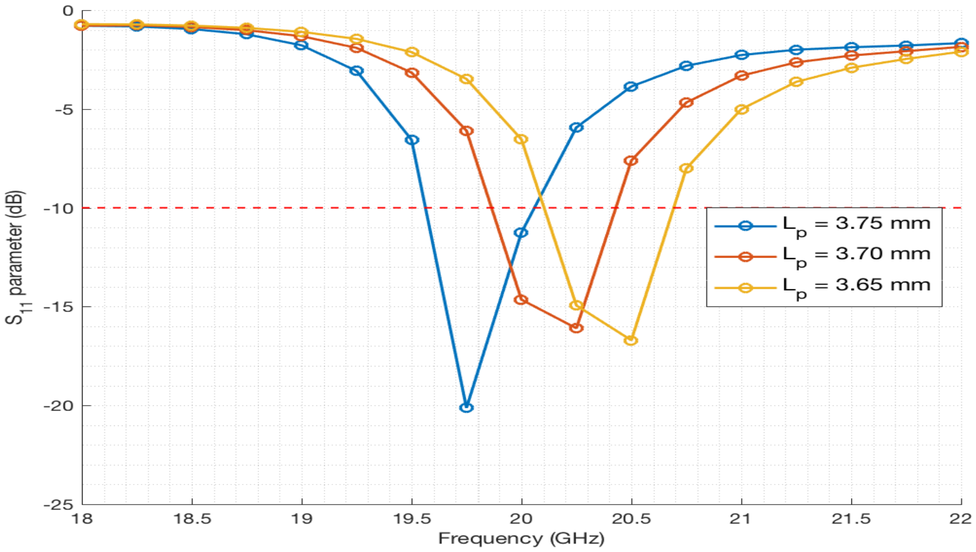

Figure 4.24: S_{11} parameter of the parametric simulation of the length of the patch (L_p) for the pair of antennas with the lateral feed.

The results of the parametric simulation reveal an improvement from −11.26 dB to −14.65 dB at 20 GHz with a patch length of 3.70 mm.

Since the connection between the power divider and each pair of antennas was made using SMA connectors, four holes were designed to allow for the fixation of the antennas to a physical support to improve the robustness of the system. The design of these holes is shown in figure 4.25.

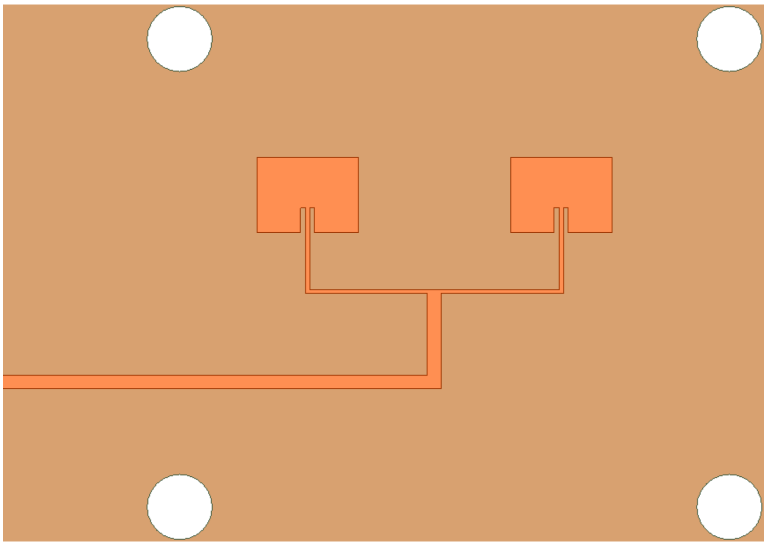

Figure 4.25: Design of the pair of the patch antennas with the holes for fixation.

Figure 4.26 shows the radiation pattern of the individual antenna and of the pair of antennas with the lateral feed. As observed in this figure, the radiation pattern of the pair of antennas presents a more directive pattern, increasing the directivity from around 6 dB to 9.5 dB, when compared to the individual patch antenna.

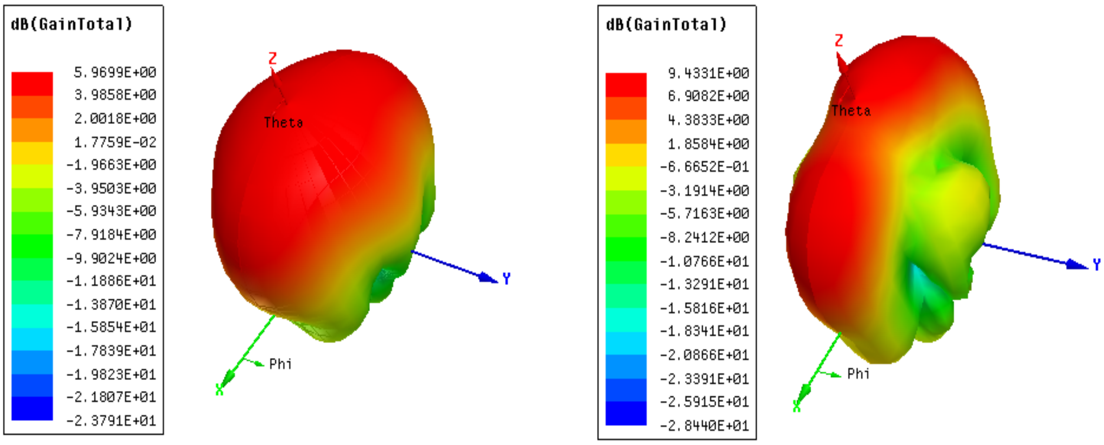

(a) Radiation pattern of the individual patch antenna.

(b) Radiation pattern of the pair of antennas.

Figure 4.26: Radiation pattern of the individual patch antenna and of the pair of antennas with the lateral feed.

Figure 4.27 shows a photography of the developed pair of antennas with a SMA connector.

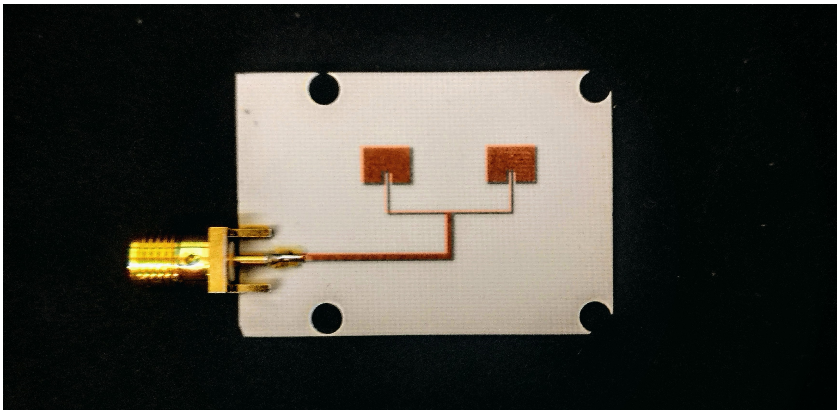

Figure 4.27: Photography of the fabricated pair of antennas.

The HFSS allows for the simulation of multiple antennas with different individual feeding ports. To predict the behavior of each pair of antennas when mounted on the array configuration side-by-side, a simulation of four pairs of antennas was performed, with the configuration as shown in figure 4.28.

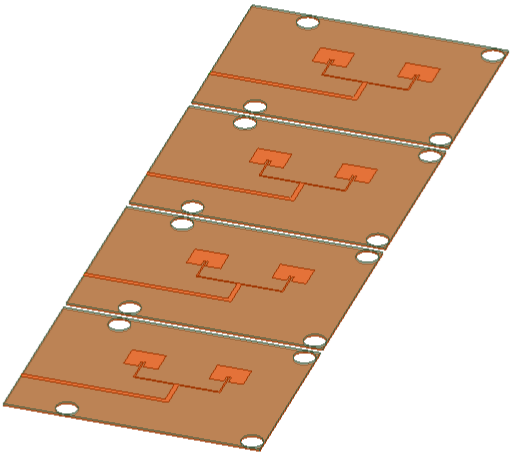

Figure 4.28: Four pairs of antennas syde-by-side.

The results of this simulation are shown in figure 4.29, and as observed, the S_{11} parameter of each individual pair of antennas is in accordance with the desired, this is, with a value below $-10\,\mathrm{dB}$ at 20 GHz. The line "Antenna 1" corresponds to the upper antenna of the array and the line "Antenna 4" corresponds to the lower antenna, with lines "Antenna 2" and "Antenna 3" corresponding to the antennas in the middle, in the same sequence.

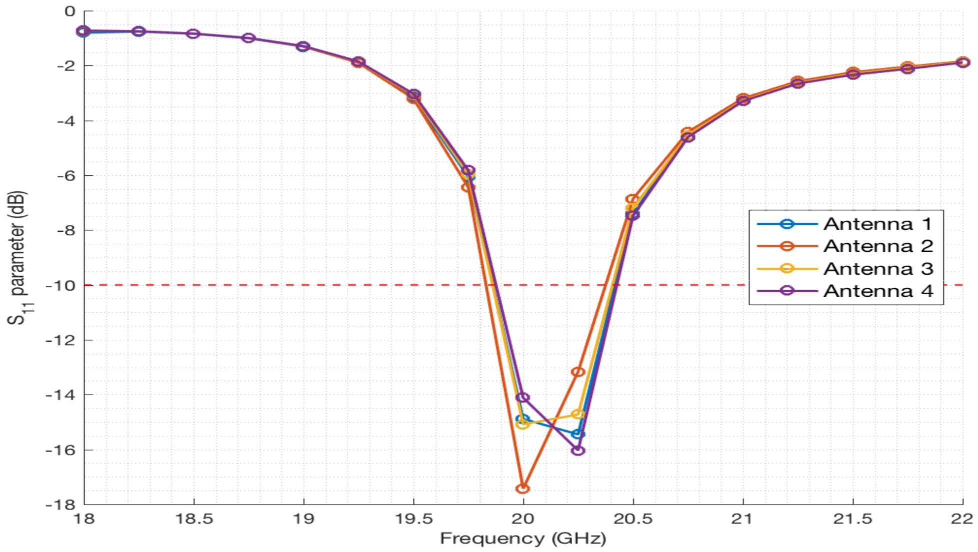

Figure 4.29: S_{11} parameter of each of the four antennas.

Figure 4.30 shows the radiation pattern of the complete array. As observed, the radiation pattern has a higher directivity of 15 dB and presents a narrower beam in the vertical direction due to the placement of the four pair of antennas as shown in figure 4.28.

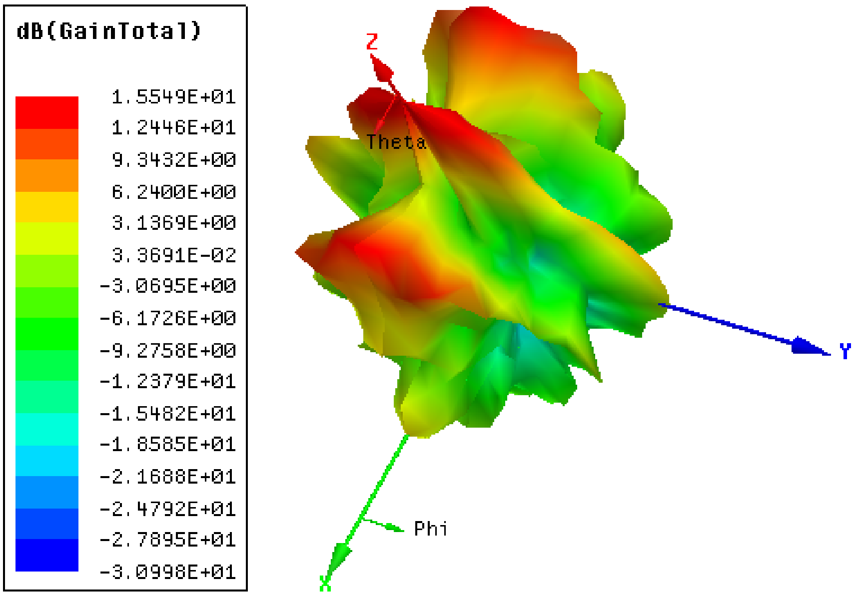

Figure 4.30: Radiation pattern of the complete array.

Table 4.4 shows the final values of the parameters for the pair of antennas obtained after the various parametric simulations.

Table 4.4: Final values of the parameters of the pair of antennas after the parametric simulations.

Parameter	**Dimension (mm)**
Patch width (W_p)	4.969
Patch length (L_p)	3.70
Feed width (W_f)	0.2
Feed length (L_f)	4
Inset feed length (y_0)	1.2
Feed gap (g)	0.248
Length $50\,\Omega$ line (L_{50})	4

4.4 Power divider design

To feed each of the antennas using only one feeding point, the development of a one-to-four power divider was necessary. The design of this element was split into two phases: the first consisted of a schematic design and the second of an electromagnetic (EM) simulation of the layout generated by the schematic design. The development and simulation of this element were performed using the Advanced Design System (ADS) software, which is an electronic design automation software for RF, microwave, high-speed digital, and power electronics applications [32].

Taking into account the size of each individual pair of antennas and the simulations of the array, the distance between each antenna feed should be 29 mm. Figure 4.31 shows the basic design idea of the one-to-four power divider, where the number "1" represents the input port and the numbers "2" to "5" the output feeds.

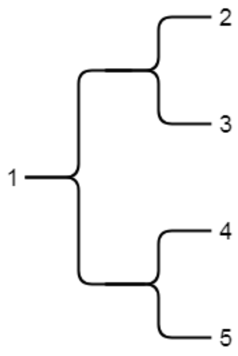

Figure 4.31: Basic design idea of the one-to-four power divider. Each number represents a port where "1" is the input port and the rest are the output port.

4.4.1 Schematic design

The design of the power divider consisted in creating three one-to-two power dividers and connect the three to obtain a one-to-four power divider. The one-to-two power dividers consisted of two microstrip lines of 50 Ω that connected in the middle, creating a junction with 25 Ω of impedance. This junction was then connected to a taper to smoothly transform the impedance back to 50 Ω, as shown in figure 4.32. The width of the microstrip lines for 25 Ω and 50 Ω (represented by "z25" and "z50" in figure 4.32, respectively) was calculated using the equation 4.15, where W_f is the width of the microstrip line and h is the height of the substrate.

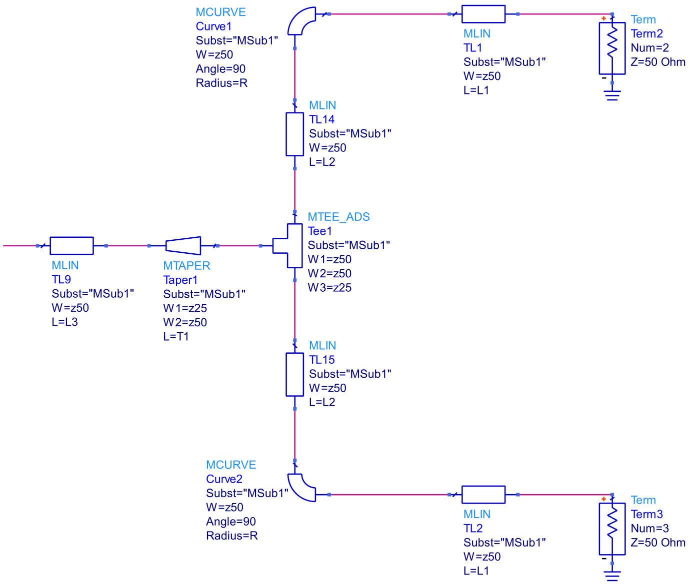

Figure 4.32: Schematic of a one-to-two power divider.

The one-to-four power divider was obtained by combining three sets of one-to-two power dividers, and the resulting schematic is shown in figure 4.33.

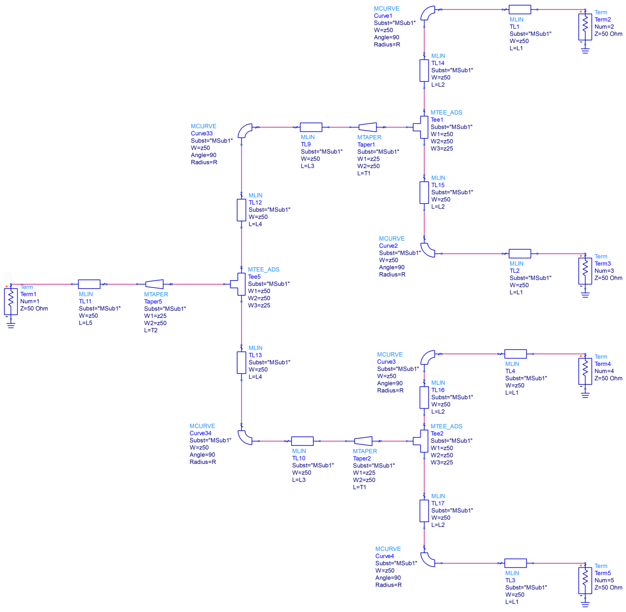

Figure 4.33: Schematic of the one-to-four power divider.

The tuning feature of ADS was used to tune the values of the lengths of the microstrip lines and of the radius of the corners to achieve the desired result. The results of the simulation of the schematic are shown in figures 4.34 and 4.35. Figure 4.34 represents the S(1,1) parameter which is the amount of input power reflected by the input port.

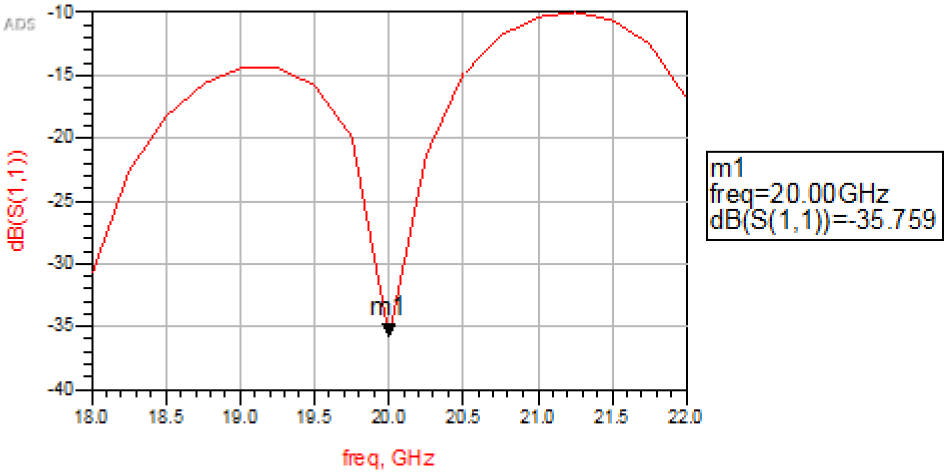

Figure 4.34: S(1,1) parameter of the schematic of the power divider.

Figure 4.35 shows the S(1,2) to the S(1,5) parameters, which represent the amount of power transferred from the input port "1" to each of the four output ports. Each one-to-two power divider creates a -3 dB attenuation due to the power division, and since there are two power dividers from the input feed to each of the four output feeds, the expected attenuation from the input port to one of the outputs of the complete power divider is -6 dB. By analyzing figure 4.35, one can observe that the obtained value is -6.510 dB, which is almost the expected value.

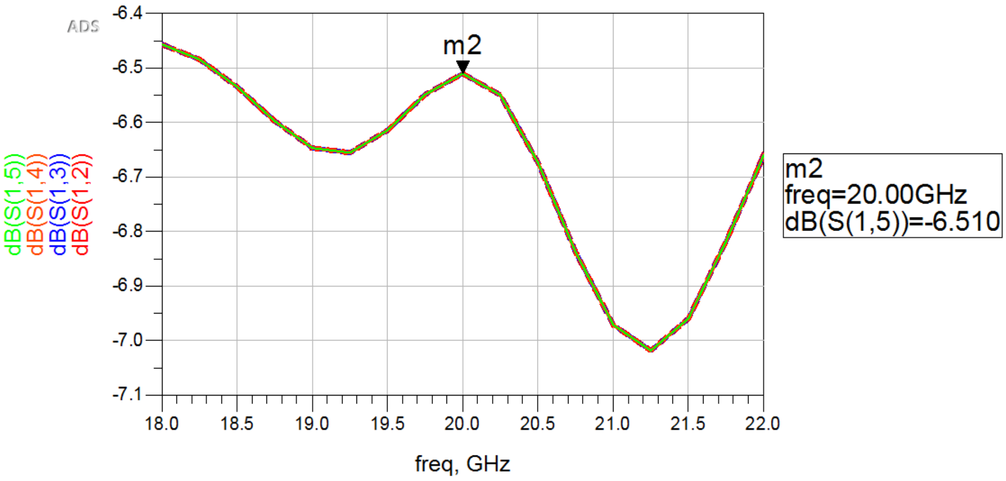

Figure 4.35: S(1,2) to S(1,5) parameters of the schematic of the power divider.

By importing the S-parameters of the pair of antennas developed in HFSS to ADS, the power divider and the antennas can be simulated together to verify if the power divider does not cause unwanted effects on the antenna behaviour. As shown in figure 4.36, the results show that even with the power divider, the antennas radiate at 20 GHz, showing a value of -13.004 dB for the S(1,1) parameter.

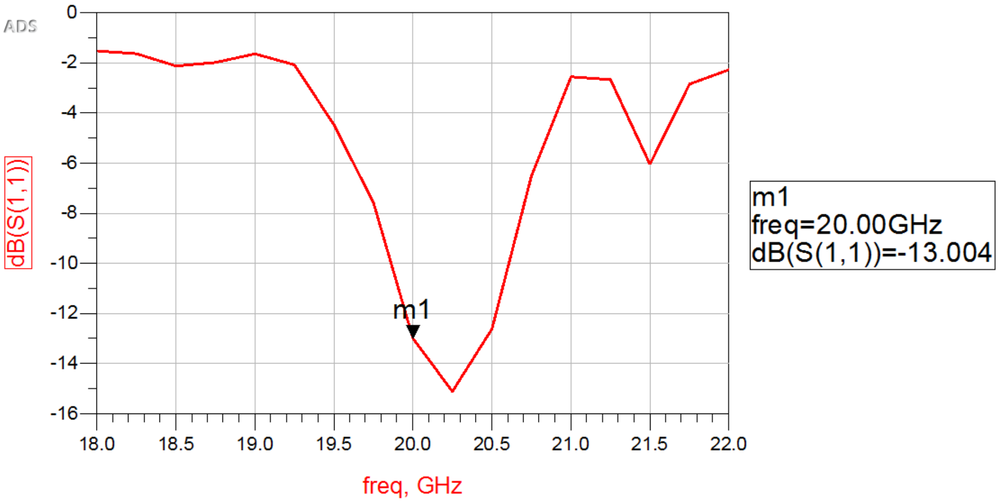

Figure 4.36: S(1,1) parameter of the simulation of the schematic of the power divider together with the S-parameters of the pair of antennas extracted from HFSS.

The results from the analysis of the schematic show that the power divider is correctly sized for the intended purpose and to the desired dimensions. The layout of the power divider was generated using the ADS tool that automatically generates the layout from the schematic, and the result is shown in figure 4.37.

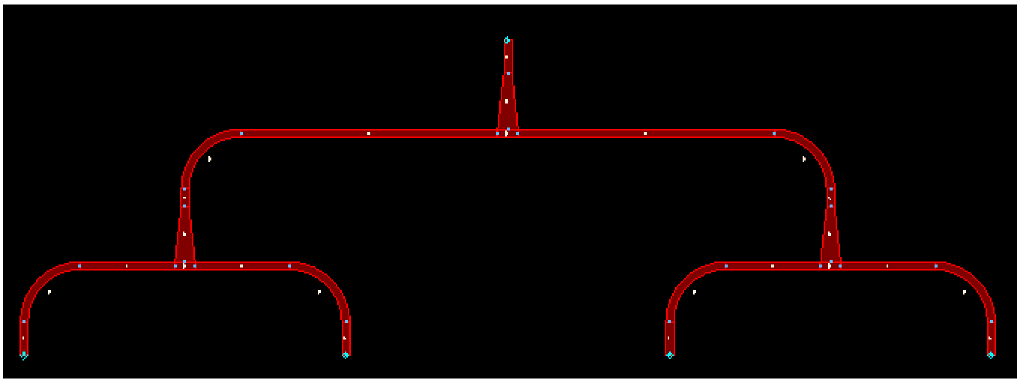

Figure 4.37: Layout that resulted from the automatic tool.

4.4.2 EM simulation of the layout

To perform the EM simulation of the layout, the substrate has to be defined and each layer has to be assigned to the correct format. Figure 4.38 shows the substrate used during the EM simulation. The "cond" layer was defined as a copper conductor with a thickness of 18 µm. The dielectric material was the Rogers RO4003C with a thickness of 0.305 mm. The ground layer was defined as a slot plane since it is the most appropriate for the use of the method of moments (MoM) analysis.

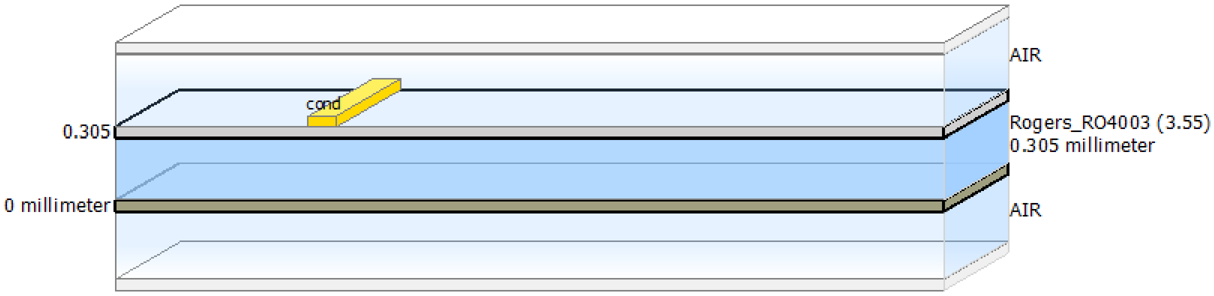

Figure 4.38: Substrate used for the EM simulation.

The results of the EM simulation using the method of moments (MoM) are shown in figures 4.39 and 4.40. As observed in figure 4.39, the value of S(1,1) is −18.812 dB, an increase from −35.759 dB of the schematic results. This result is explained by the more complex calculations that occur during the EM simulation, that take into account the circulation of the currents over the conductor layer, the effect of the ground plane, the losses from the substrate and the mutual coupling between the different microstrip lines.

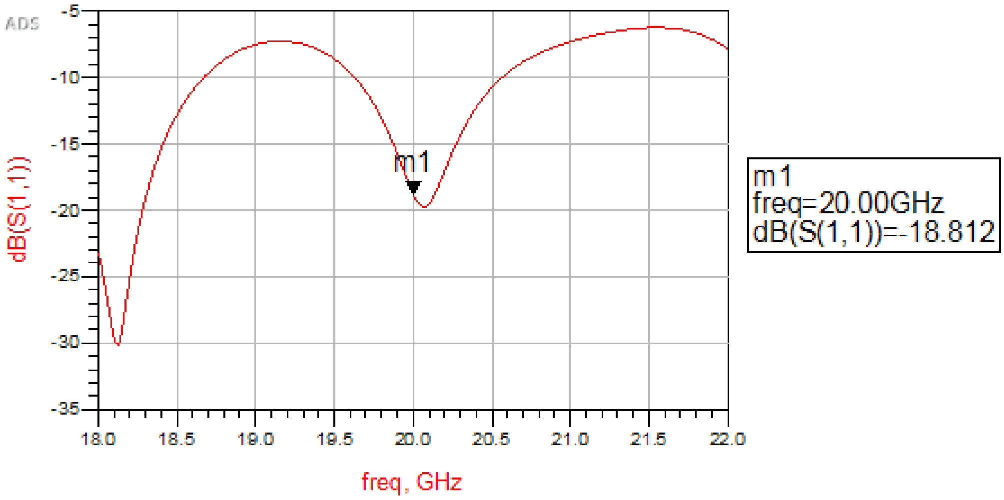

Figure 4.39: S(1,1) parameter of the layout of the power divider.

Figure 4.40 also reveals some differences between the results of the schematic and the layout analysis. The values for the S(1,2) to S(1,5) parameters decreased in 1 dB, from −6.510 dB to around −7.5 dB. There is also a slight difference of 0.1 dB between the values of the S(1,2) and S(1,5) and the values of the S(1,3) and S(1,4), as denoted by the two different lines in figure E. This difference is caused by the different relative positions of the output ports. Ports 2 and 5 are in the extremities of the power divider, whereas, ports 3 and 4 are in middle part.

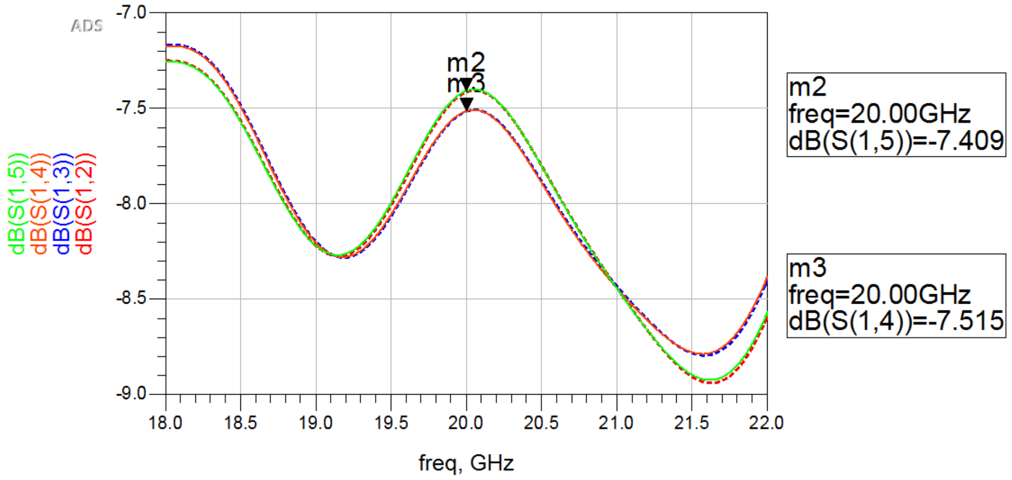

Figure 4.40: S(1,2) to S(1,5) parameters of the layout of the power divider.

The S-parameters extracted from the HFSS were again used to validate the correct behaviour of the power divider together with the antennas. As in the simulation with the schematic, the simulation with the layout and the pair of antennas showed that the system was radiating at 20 GHz, as shown in figure4.41 with a value of S(1,1) of -11.504 dB.

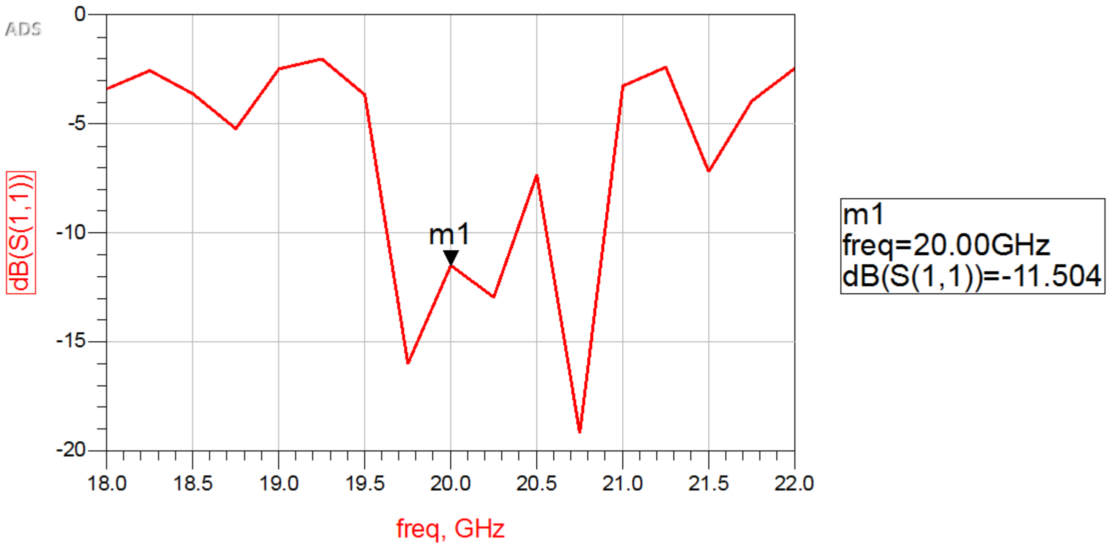

Figure 4.41: S(1,1) parameter of the simulation of the layout of the power divider together with the S-parameters of the antennas extracted from HFSS.

Figure 4.42 shows a photography of the developed power divider with SMA connectors.

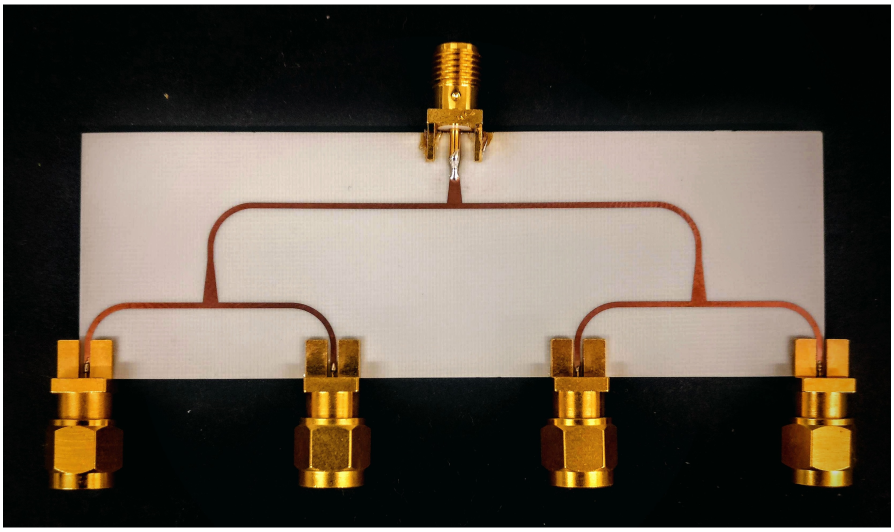

Figure 4.42: Photography of the developed power divider.

4.5 Microstrip line phase shifters

Due to budget limitations and for the purpose of testing the proposed system with the steering of the beam, four phase shifters were developed using microstrip line technology. The shift in the phase of the signal was achieved by changing the length of the microstrip line that the signal has to go through. Therefore, to implement the phase shifters, four microstrip lines with different lengths were created. The schematic of the lines for the phase shifter is shown in figure 4.43.

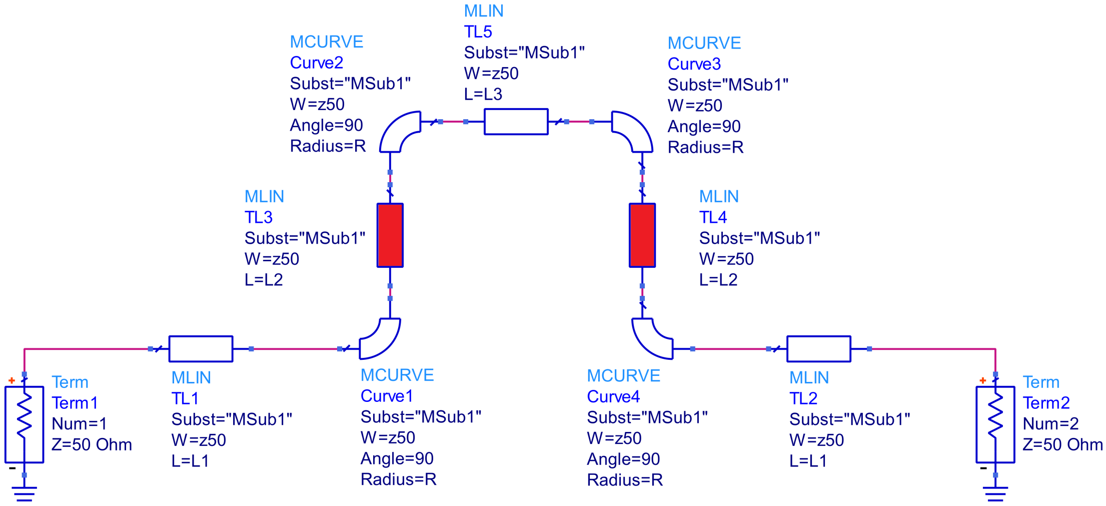

Figure 4.43: Schematic of the microstrip line phase shifter.

The four different phase shifters were achieved by changing the length of the two red blocks shown in figure 4.43. By only changing the length of these blocks, the footprint of all the phase shifters stayed the same, allowing them to be placed between the power divider and the antennas, maintaining the desired configuration and distance between the antennas. An example of the layout of one of the phase shifters is shown in figure 4.44.

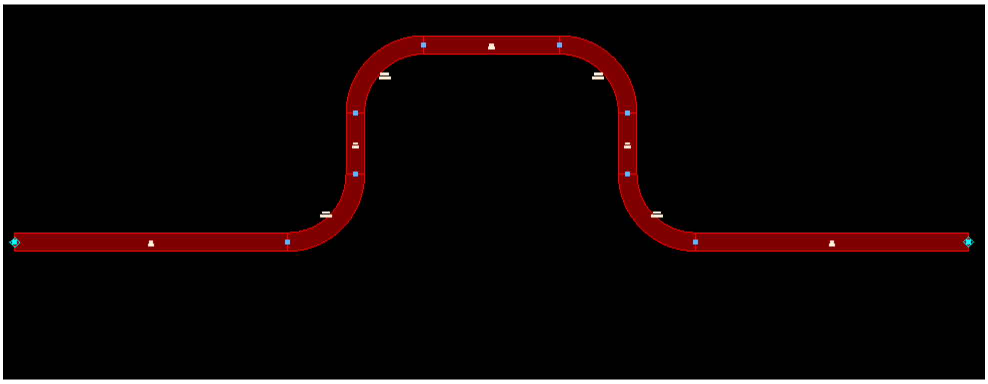

Figure 4.44: Example of the layout of one of the phase shifters.

The layout of each phase shifter was simulated using the same substrate as for the simulation of the layout of the power divider. The results shown in figure 4.45 represent the phase shift that each phase shifter induces in the input signal.

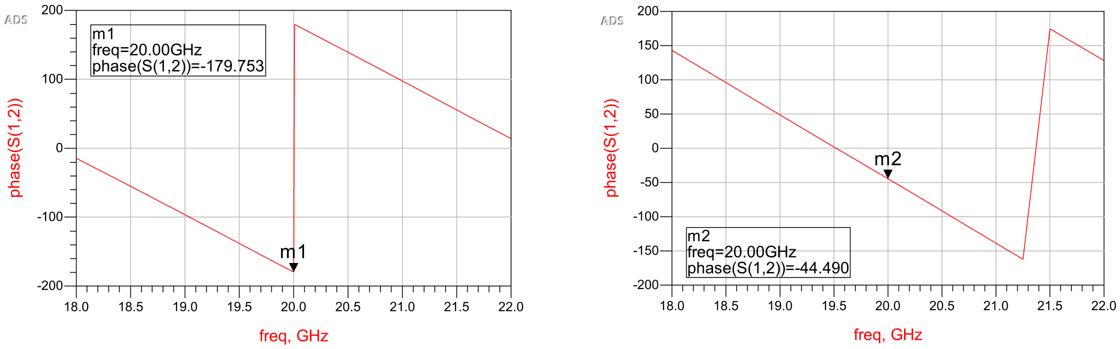

(a) Phase shift corresponding to 0°.

(b) Phase shift corresponding to 225°.

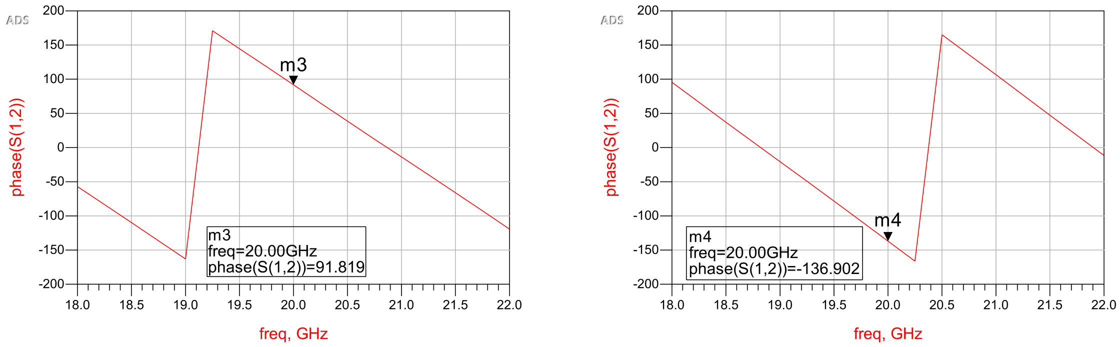

(c) Phase shift corresponding to 450°.

(d) Phase shift corresponding to 675°.

Figure 4.45: Different phases for each of the phase shifters.

The difference in phase between each consecutive figure from 4.45a to 4.45d is 225°. This fact is better observed in figure 4.46, where each line corresponds to the phase of each of the images in figure 4.45. Between each consecutive line, there is a negative angle of 225°, as intended.

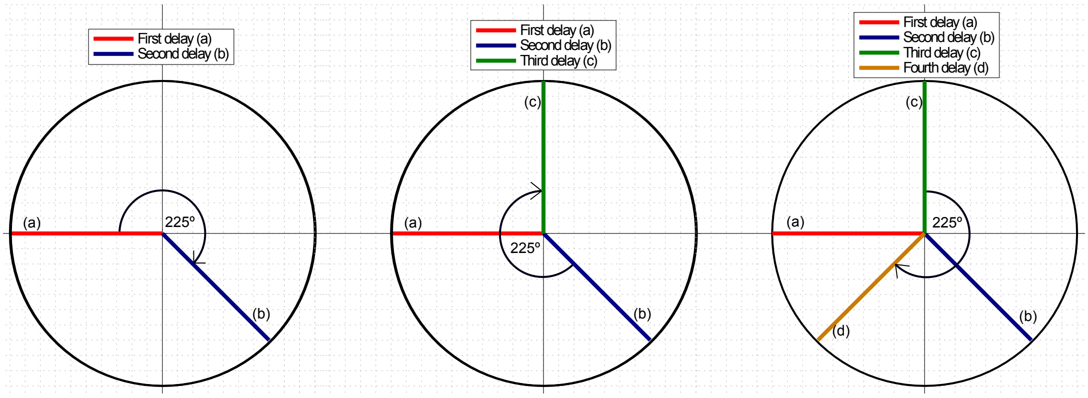

Figure 4.46: Representation of the phase difference between each consecutive phase shifter.

Based in equation 4.1 and with a phase difference $(\Delta\varphi)$ of 225°, the expected angle of the beam of the developed array with the phase shifters is 20°.

Figure 4.47 shows a photography of one of the developed phase shifter with the SMA connectors.

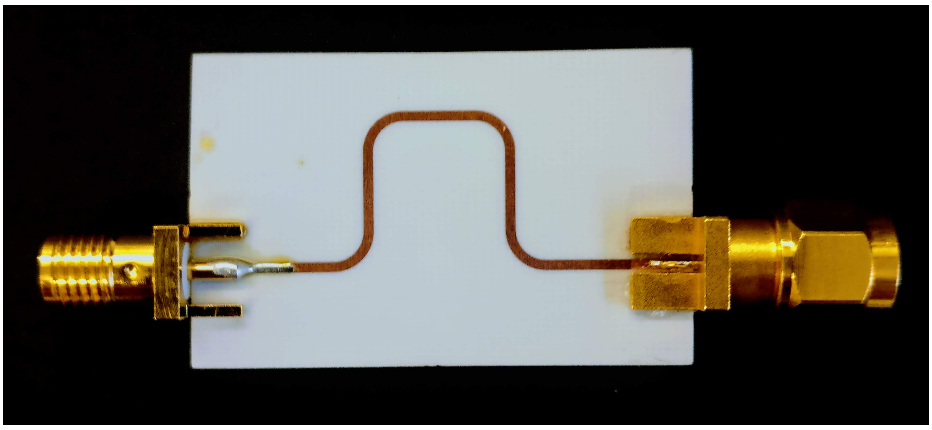

Figure 4.47: Photography of one of the fabricated phase shifters.

4.6 Complete system

The complete system, which includes the power divider, the mircrostrp phase shifters and the developed pair of antennas was simulated using ADS. The schematic used for this simulation is shown in figure 4.48, where the layout of the power divider and of the phase shifters is used, along with the S-parameters extracted from HFSS.

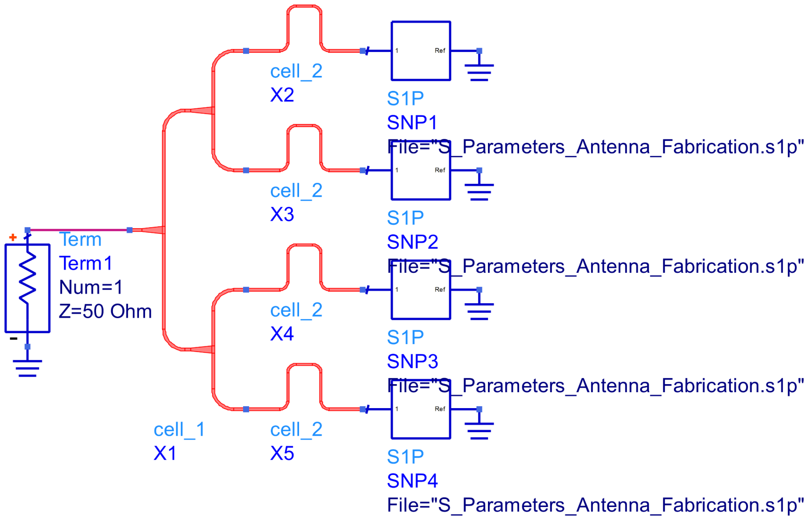

Figure 4.48: Schematic used to simulate all the different components of the system.

The results of this simulation are shown in figure 4.49. The results show that, at 20 GHz, the system is adapted since it has a value of -13.936 dB for the S_{11} parameter of the complete system.

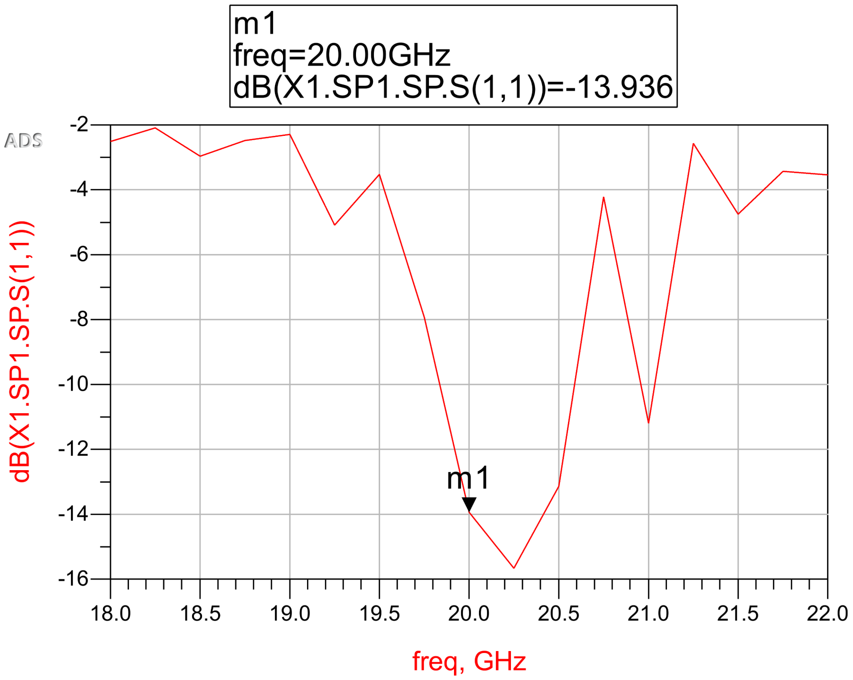

Figure 4.49: S(1,1) parameter of the simulation of the layout of the power dividerand of the phase shifters together with the S-parameters of the antennas extracted from HFSS.

Figure 4.50 shows a photography of the complete system.

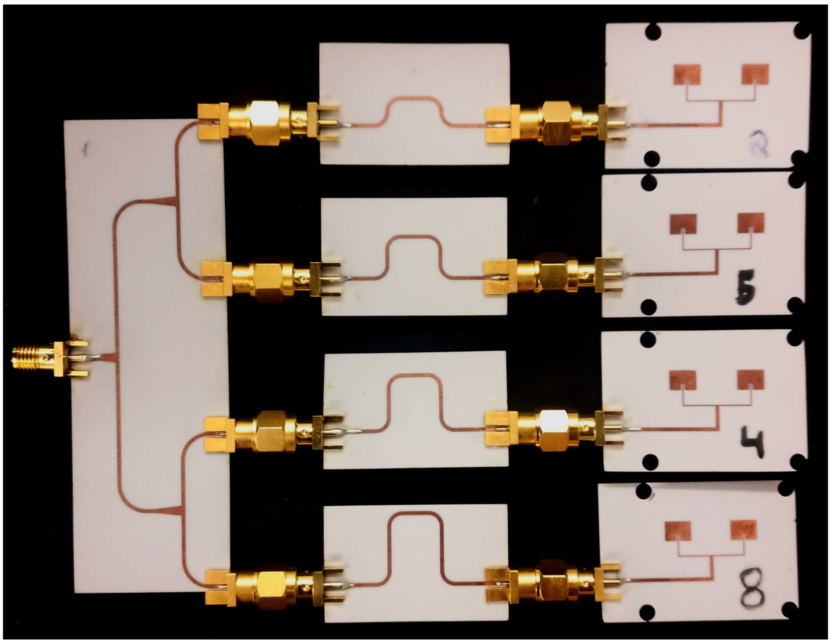

Figure 4.50: Photography of the complete system assembled with all the individual components.

4.7 Test and results of the fabricated elements

A set of tests was performed over the different components simulated during the previous sections to assess if the fabricated components are in accordance to the simulations. These tests were performed using the VNA to extract the S-parameters of each fabricated element.

Figure 4.51 shows the S_{11} parameter of the fabricated antennas in comparison with the S_{11} parameter achieved in the simulations. As observed, there is a different behavior between the measured and simulated parameter. The fabricated antennas are adpated to the range of 19.2 GHz to 19.5 GHz and of 21.5 GHz to 21.8 GHz. At the desired frequency of 20 GHz, the fabricated antennas present an S_{11} parameter of -8 dB, a value higher than the desired -10 dB.

At these frequencies, the size of the wavelength is in the magnitude of millimeters. Therefore, the size of the elements fabricated is also in the magnitude of millimeters. As observed by the graphs of the results of the parametric simulations of the pair of antennas, a difference as small as 0.05 millimeters in the size the antenna or of the feed can create a shift of the resonant frequency and a change of the behavior of the antenna. These variations can happen during the fabrication processes, changing the behavior of the antennas.

The substrate can also present differences in its characteristics due to fabrication variations. The specific characteristics of the substrate in use are different from the characteristics presented in the datasheet of this type of substrate and that were used during the simulations. The dielectric constant of the substrate of the fabricated elements is 3.35, compared to 3.55 of the datasheet. Also, the dielectric loss constant is 0.0035 compared to 0.0027. These differences also influence the behavior of the produced antennas in comparison to the simulations.

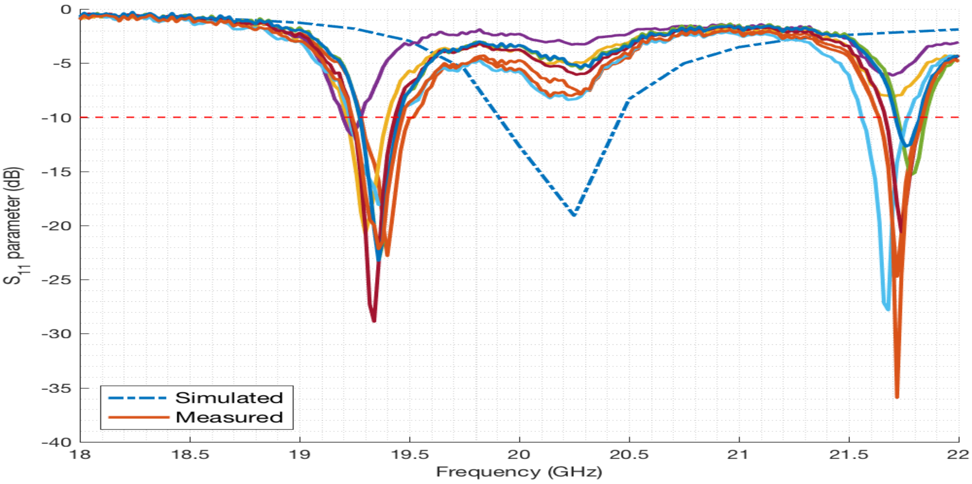

Figure 4.51: S_{11} parameter measured by the VNA of the fabricated antenna versus the result of the simulation.

As for the power divider, the test of the S-parameters using the VNA also revealed differences in comparison to the simulations, as shown in figure 4.52. The negative peak value at 20 GHz is higher than the simulated value having a value of -6 dB. The curve of the measured S_{11} parameter of the power divider is fairly equal in shape to simulated curve, although presenting a shift of around 7 dB at the desired frequency. Again, this difference is related to the losses in the substrate due to the different characteristics when compared to the simulations. The losses in the cables used during the tests can also interfere with the measurements of this parameter.

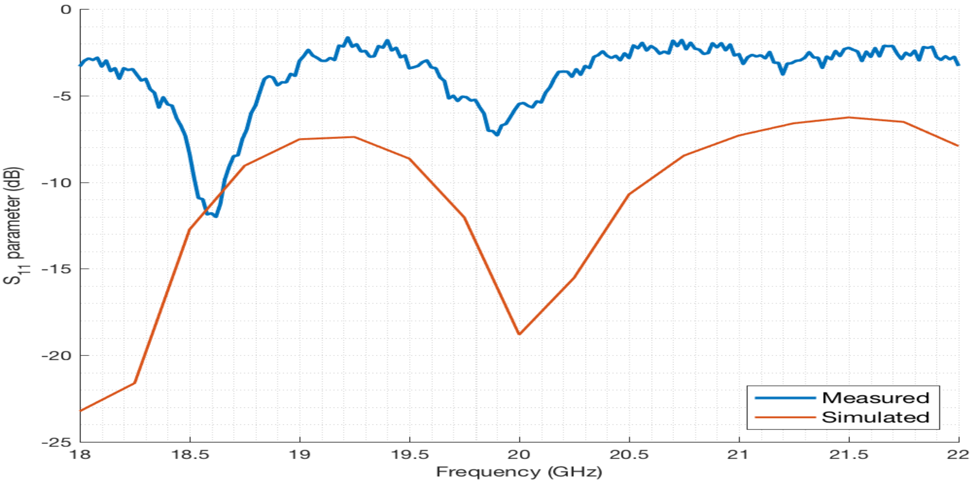

Figure 4.52: S_{11} parameter measured by the VNA of the fabricated power divider versus the result of the simulation of the layout of the power divider.

The results of the S-parameters for the transmission of power between the input port "1" and the output ports are shown in figure 4.53. The results show a decrease in the value of the S-parameters at 20 GHz when compared to the simulated and expected values. The analysis of figure 4.53 and figure 4.40 reveals a correlation between the simulation and the measured value, since the value of the S(1,2) and the value of the S(1,5) is the same at 20 GHz as was the case in the simulations.

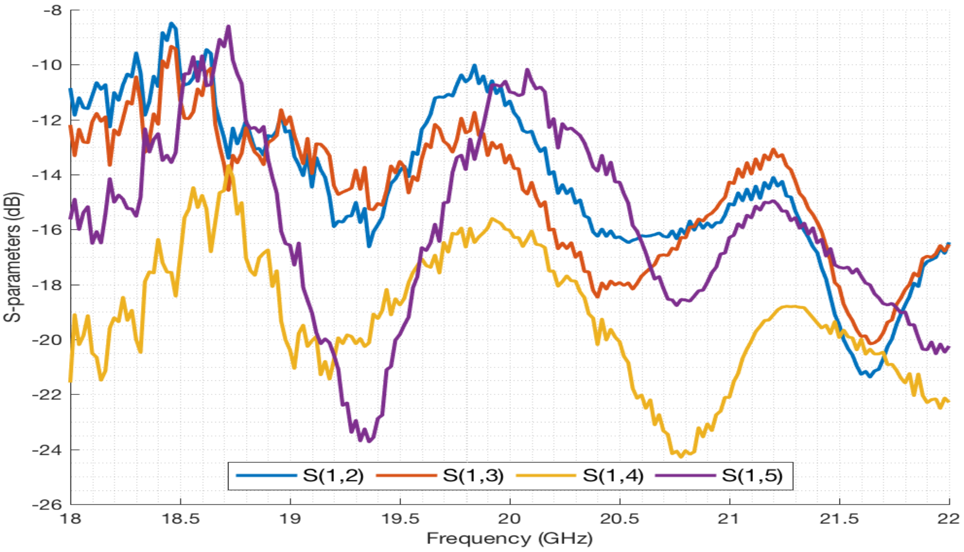

Figure 4.53: S(1,2) to S(1,5) parameters measured by the VNA of the fabricated power divider.

The use of SMA connectors can also influence these results. Although the chosen SMA connectors were suitable for frequencies up to 26.5 GHz, the mounting type and the soldering of the connectors to the board can have an influence in the performance of the elements due to the range of frequencies in use.

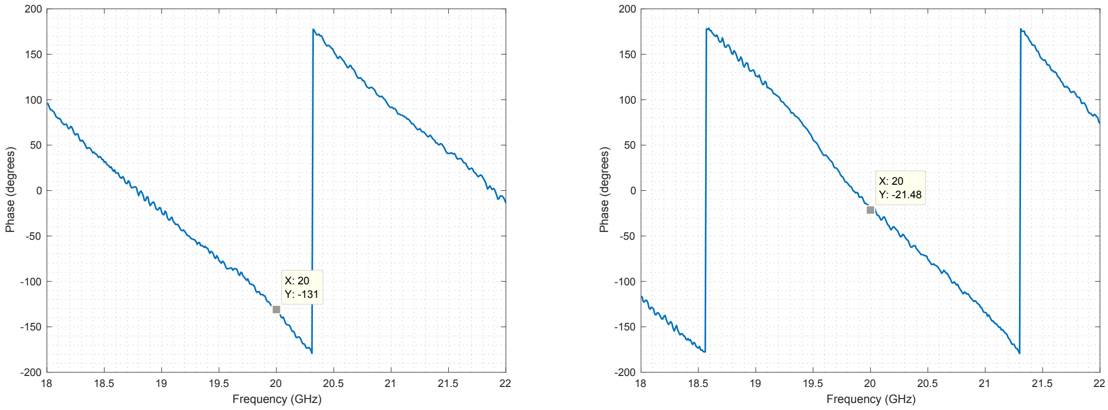

(a) Phase shift corresponding to 0°. Value at 20 GHz is of $-131°$.

(b) Phase shift corresponding to 225°. Value at 20 GHz is of $-21.48°$.

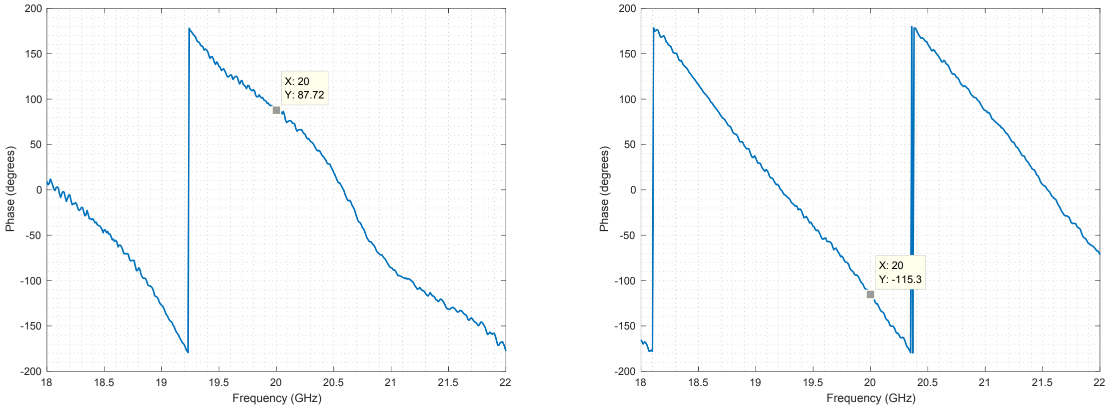

(c) Phase shift corresponding to 450°. Value at 20 GHz is of 87.72°.

(d) Phase shift corresponding to 675°. Value at 20 GHz is of $-115°$.

Figure 4.54: Different measured phases for each of the phase shifters.

As for the phase shifters, the results showed a change in the phase difference between each consecutive phase shifter. The difference between the first three phase shifters increased from 225° to 250°, with the difference between the phase shiter of 450° and 675° is around 200°. These differences are caused by variations on the fabrication process as well as different characteristics of the substrate.

Chapter 5

Conclusions and future work

The goals of this dissertation were to validate the proposed concept using the available test equipment and to evaluate the feasibility of developing a system capable of applying the technique to a real situation.

The results of the performed tests revealed a clear indication that the amount of water in a plant influences the signal's intensity. The validation of the base concept for this technique was, therefore, confirmed. Due to equipment malfunctions, the number of performed tests was lower than what was desired. Nevertheless, the results of the tests are conclusive in relation to the perception ability of the system to the existence of water in an object or a plant.

The amount of computational power needed to perform RF simulations also limited the characteristics of the proposed systems.

Given the test equipment limitations as well as budget limitations for this dissertation, some of the choices made during the course of the dissertation were made based on the ability to be tested in-house or not, as well as a price limit for the components to be bought. This influenced the decisions taken during the development of the system.

Working on a subject that with no prior technical knowledge proved to be a major shortcoming, especially given the time required to understand and learn the concepts needed to develop antennas. This learning curve for the development of the array and for the study of the different implementations only allowed for one interaction of a possible system implementation.

Given the time available for the development of this dissertation, the results are satisfactory. With time for only one iteration of the proposed system, all the defaults and problems encountered with this implementation could not be resolved. The learnings from the development process of the proposed system are used in the following section to propose other system implementations and new ideas to improve the technique and the analysis of the collected.

5.1 Future work

The use of coaxial feeding for the microstrip patch antennas would allow for a better arrangement of the elements of the array, enabling a closer proximity between consecutive antennas and allowing for a better efficiency of the array as a whole. By implementing coaxial feeding, the feeding circuitry of the array could be printed and developed in a different layer from the antennas, in a different substrate with different characteristics to improve the efficiency of the feeding lines. The study of other possible shapes of the patch antenna can also represent an improvement in the array behavior for this specific application.

The implementation of individual digital or analog phase shifters for each antenna would allow for the control of the beam in the vertical and horizontal directions at the same time, contributing to a greater level of precision during a scan. This control can be achieved by using a micro-controller connected to each phase shifter, enabling the control of the beam direction in real-time.

The development of a power amplifier or of a different method to input a 20 GHz reference signal to the different phase shifters and antennas is of utmost importance, allowing for the test and analysis of bigger plants, with a greater distance between the emitter and the receiver.

The system should also conjugate different sensors to improve the results reliability. The conjugation of different sensors to assess the climacteric conditions such as the air temperature, humidity percentage, and the atmospheric pressure would allow for better and more accurate results, with a lesser variance between measurements.

As for the analysis of data, the use of data mining techniques could be beneficial to find patterns and to extract more information. The study of the effects of the amount of water on the phase of the transmitted signal is also a possibility to allow for the extraction of more information about the plant. Tests should be performed with a greater variety of plants with different controlled conditions to create a reference as to compare to a real scan.

A study of the effects of macro-nutrients on the signals behavior has some importance. If there are differences in the signal behavior due to the presence of macro-nutrients, this could lead to an even greater level of detail for assessing the plants' necessities.

References

[1] Stein Sandven, Ola Johannessen, and K Kloster. Sea ice monitoring by remote sensing, 09 2006.

[2] Thuy Le Toan. SAR image information content - scattering physics.

[3] Radar images.

[4] A. Moreira, P. Prats-Iraola, M. Younis, G. Krieger, I. Hajnsek, and K. P. Papathanassiou. A tutorial on synthetic aperture radar. *IEEE Geoscience and Remote Sensing Magazine*, 1(1):6–43, March 2013.

[5] Perrine Loussert, Frédéric Baup, Samuel S. Corgne, Hervé Quénol, and Alejandro Ortega Hernandez. Analysis of SAR and optical temporal signatures of grapevine over a heterogeneous vineyard landscape. In *SPIE Remote Sensing*, Edinburgh, United Kingdom, October 2016.

[6] G. Schiavon, D. Solimini, and A. Burini. Sensitivity of multi-temporal high resolution polarimetric C and L-band SAR to grapes in vineyards. In *2007 IEEE International Geoscience and Remote Sensing Symposium*, pages 3651–3654, July 2007.

[7] Measuring Vegetation (NDVI & EVI) : Feature Articles.

[8] Bunkei Matsushita, Wei Yang, Chen Jin, Onda Yuyichi, and Qiu Guoyu. Sensitivity of the enhanced vegetation index (EVI) and normalized difference vegetation index (NDVI) to topographic effects: A case study in high-density cypress forest. 7, 11 2007.

[9] *Recomandation Itu-R P.676-11: Attenuation by Atmospheric Gases*. P Series Radiowave Propagation. Radiocomunication sector of ITU, 2016.

[10] Jorge Mendes, Filipe Santos, Inês Cas tel ao, Tiago Ramalho, Cândido Duarte, Fernanda Almeida, and Cristina Carlos. Romovi – robô modular e cooperativo para v inhas de encosta. *AgroTec*, pages 19–21, Dec/Jan/Feb 2017.

[11] F. Ulaby. Radar measurement of soil moisture content. *IEEE Transactions on Antennas and Propagation*, 22(2):257–265, March 1974.

[12] Fawwaz T. Ulaby, Pascale C. Dubois, and Jakob van Zyl. Radar mapping of surface soil moisture. *Journal of Hydrology*, 184(1):57 – 84, 1996. Soil Moisture Theories and Observations.

[13] Susan C. Steele-Dunne, Heather McNairn, Alejandro Monsivais-Huertero, Jasmeet Judge, Pang-Wei Liu, and Kostas Papathanassiou. Radar remote sensing of agricultural canopies: A review. *IEEE Journal of Selected Topics in Applied Earth Observations and Remote Sensing*, 10(5):2249–2273, 2017.

[14] Mark T Crockett and David Long. An introduction to synthetic aperture radar: a high-resolution alternative to optical imaging. 2013.

[15] M.S. Moran, A. Vidal, D. Troufleau, J. Qi, T.R. Clarke, P.J. Pinter, T.A. Mitchell, Y. Inoue, and C.M.U. Neale. Combining multifrequency microwave and optical data for crop management. *Remote Sensing of Environment*, 61(1):96 – 109, 1997.

[16] M Susan Moran, Daniel C Hymer, Jiaguo Qi, and Edson E Sano. Soil moisture evaluation using multi-temporal synthetic aperture radar (sar) in semiarid rangeland. *Agricultural and Forest Meteorology*, 105(1):69 – 80, 2000.

[17] P. C. Dubois, J. van Zyl, and T. Engman. Measuring soil moisture with imaging radars. *IEEE Transactions on Geoscience and Remote Sensing*, 33(4):915–926, Jul 1995.

[18] Eni G. Njoku and Dara Entekhabi. Passive microwave remote sensing of soil moisture. *Journal of Hydrology*, 184(1):101 – 129, 1996. Soil Moisture Theories and Observations.

[19] Y. Kim, T. Jackson, R. Bindlish, H. Lee, and S. Hong. Radar vegetation index for estimating the vegetation water content of rice and soybean. *IEEE Geoscience and Remote Sensing Letters*, 9(4):564–568, July 2012.

[20] A. Burini, A. Minchella, and D. Solimini. SAR in agriculture: sensitivity of backscattering to grapes. In *Proceedings. 2005 IEEE International Geoscience and Remote Sensing Symposium, 2005. IGARSS '05.*, volume 3, pages 1542–1545, July 2005.

[21] Bacchus - a european research project.

[22] A. Burini, F. Del Frate, A. Minchella, G. Schiavon, D. Solimini, R. Bianchi, L. Fusco, and R. Horn. Multi-temporal high-resolution polarimetric L-band SAR observation of a wine-producing landscape. In *2006 IEEE International Symposium on Geoscience and Remote Sensing*, pages 501–503, July 2006.

[23] E.Raymond Hunt and Barrett N Rock. Detection of changes in leaf water content using near- and middle-infrared reflectances. *Remote Sensing of Environment*, 30(1):43 – 54, 1989.

[24] Compton J. Tucker. Remote sensing of leaf water content in the near infrared. *Remote Sensing of Environment*, 10(1):23 – 32, 1980.

[25] A. Bannari, D. Morin, F. Bonn, and A. R. Huete. A review of vegetation indices. *Remote Sensing Reviews*, 13(1-2):95–120, 1995.

[26] A Huete, K Didan, T Miura, E.P Rodriguez, X Gao, and L.G Ferreira. Overview of the radiometric and biophysical performance of the modis vegetation indices. *Remote Sensing of Environment*, 83(1):195 – 213, 2002. The Moderate Resolution Imaging Spectroradiometer (MODIS): a new generation of Land Surface Monitoring.

[27] Bo cai Gao. NDWI—a normalized difference water index for remote sensing of vegetation liquid water from space. *Remote Sensing of Environment*, 58(3):257 – 266, 1996.

[28] Hui Qing Liu and Alfredo Huete. A feedback based modification of the NDVI to minimize canopy background and atmospheric noise. 33:457 – 465, 04 1995.

[29] David M Pozar. *Microwave engineering*. John Wiley & Sons, 2009.

[30] C.A. Balanis. *Antenna Theory: Analysis and Design*. Number vol. 1 in Antenna Theory: Analysis and Design. John Wiley & Sons, 2005.

[31] Ansys hfss: High frequency electromagnetic field simulation software. `https://www.ansys.com/products/electronics/ansys-hfss`.

[32] Advanced design system (ads) | keysight (formerly agilent's electronic measurement). `https://www.keysight.com/en/pc-1297113/advanced-design-system-ads?nid=-34346.0.00&cc=PT&lc=eng&cmpid=zzfindeesof-ads`.